

# Quantum Theory of Scattering

*final project:*

Standard Hermitian & Non-Hermitian Approach

Michal Ptáček

June 2022

## Contents

<b>1</b>	<b>Introduction</b>	<b>2</b>
<b>2</b>	<b>Theoretical Background</b>	<b>2</b>
2.1	Quantum Theory of Scattering . . . . .	2
2.2	Resonances as Meta-stable States . . . . .	6
2.3	Complex Scaling . . . . .	8
2.3.1	Scalar Product and C-Product . . . . .	10
2.4	Interaction with Light . . . . .	11
2.4.1	Interaction Hamiltonian . . . . .	11
2.4.2	Standard Floquet Theory . . . . .	14
2.4.3	Non-Hermitian Floquet Theory . . . . .	16
2.4.4	Exceptional Points (EP) . . . . .	17
<b>3</b>	<b>Computational Algorithms</b>	<b>19</b>
3.1	Basis Set Expansion . . . . .	19
<b>4</b>	<b>Implementation Details</b>	<b>20</b>
<b>5</b>	<b>Results</b>	<b>22</b>
5.1	Scattering on a Potential . . . . .	22
5.1.1	Standard Hermitian Approach . . . . .	23
5.1.2	Non-Hermitian Approach . . . . .	43
5.2	Light Induced Resonances . . . . .	47
5.2.1	Standard Floquet Theory . . . . .	48
5.2.2	Non-Hermitian Floquet Theory . . . . .	48
5.2.3	Exceptional Point . . . . .	51
<b>6</b>	<b>Discussion and Summary</b>	<b>57</b>
6.1	Numerical Approach . . . . .	57
6.2	Basis Set Expansion and Complex Scaling . . . . .	57
6.3	Floquet Theory and Complex Scaling . . . . .	57

# 1 Introduction

The scattering theory represents one of the most studied areas of quantum mechanics. The phenomena of quantum scattering can be rather complex and involving process, but in this project we will restrict ourselves to one of the simplest cases: scattering of an incoming quantum particle represented by a wavepacket on a smooth local well-converging potential in one dimension. The reduced dimensionality of the introduced problem simplifies the evaluation significantly.

The problem will be studied from several perspectives, using both Hermitian and non-Hermitian formalisms, as well as purely numerical approaches. The system will be also either isolated, or interacting with electro-magnetic field.

At the beginning, theoretical introduction into all necessary topics is made in the section 2. Two following chapters then shed some (dim) light on the implementation of all the presented methods and algorithm. In terms of size, the largest part of this report is comprised of the results, plots, and figures. Rather than creating pages of vague tables, I preferred graphical representations anywhere possible. The presented results are then summarised and briefly discussed in the last chapter.

## 2 Theoretical Background

### 2.1 Quantum Theory of Scattering

The physical problem can be formulated in a following way: Find the final state  $|\psi_{\text{OUT}}\rangle$  of the system consisting of a free-moving quantum particle described by a square integrable wavepacket  $|\psi_{\text{IN}}\rangle$ , and a smooth local well-converging potential  $V(x)$ . To be exact, the potential should fall off to zero in both plus and minus infinity with at least second power (i.e.  $x^{-2}$  or faster). We can then suppose that the interaction with the potential  $V(x)$  centered at  $x = 0$  is restricted only to some interaction interval  $(a, b)$ ;  $a < 0 < b$ . Out of this interval, the particle evolves freely:

$$V(x < a) \approx 0, V(x > b) \approx 0 . \quad (1)$$

If this condition holds, we can further formulate the so-called *asymptotic condition* for the state itself. Let  $|\psi(t)\rangle$  be a general unbound state. As  $t$  runs to  $\pm\infty$ , the state  $|\psi(t)\rangle$  tends to leave the interaction region and evolves freely. For every such state there exists an unique incoming state  $|\phi_{\text{IN}}\rangle$  such that:

$$\hat{U}(t) |\psi(0)\rangle \xrightarrow{t \rightarrow -\infty} \hat{U}_0(t) |\phi_{\text{IN}}\rangle , \quad (2)$$

and similarly there exists an unique outgoing state  $|\phi_{\text{OUT}}\rangle$  such that:

$$\hat{U}(t) |\psi(0)\rangle \xrightarrow{t \rightarrow +\infty} \hat{U}_0(t) |\phi_{\text{OUT}}\rangle . \quad (3)$$

The equations (2) and (3) can be easily rearranged into:

$$\begin{aligned} |\phi_{\text{OUT}}\rangle &= \underbrace{\lim_{t \rightarrow \infty} \hat{U}_0^\dagger(t) \hat{U}(t) \hat{U}^\dagger(-t) \hat{U}_0(-t)}_{\hat{S}} |\phi_{\text{IN}}\rangle \\ &= \hat{S} |\phi_{\text{IN}}\rangle . \end{aligned} \quad (4)$$

In equation (4), the so-called *scattering operator*  $\hat{S}$  was introduced. Since it is a result of subsequent actions of four unitary evolution operators, the scattering operator is unitary as well.

To begin with, we can expand the freely evolving incoming state (wavepacket)  $|\phi_{\text{IN}}\rangle$  into the basis of eigenstates of the free part ( $\hat{H}_0$ ) of the total Hamiltonian  $\hat{H}$  such that the Schrödinger equation (SchrE) reads:

$$\hat{H}_0 |\phi_{E\eta}\rangle = E |\phi_{E\eta}\rangle. \quad (5)$$

The equation (5) for  $\hat{H}_0 = \frac{\hat{p}^2}{2m}$  gives us twice degenerated solution. For every value of energy  $E$  ( $E > 0$ ,  $E \in \mathbb{R}$ ), there are two corresponding eigenstates—plane waves—of the form:

$$\phi_{E\eta}(x) = \langle x | \phi_{E\eta} \rangle = \sqrt{\frac{m}{2\pi\hbar^2 k}} e^{i\eta kx}, \quad (6)$$

where  $\eta = \pm 1$  marks apart the branches of the solution associated with the value of energy  $E$ . The expansion can be then written as:

$$|\phi_{\text{IN}}\rangle = \int_0^\infty dE \sum_{\eta=-1,1} \underbrace{\langle \phi_{E\eta} | \phi_{\text{IN}} \rangle}_{c_{E\eta}} \langle \phi_{E\eta} |. \quad (7)$$

Similarly, the state  $|\psi\rangle$  can be expanded in the basis of complete Hamiltonian  $\hat{H}$  eigenstates  $|\psi_{E\eta}^\pm\rangle$  which are called *stationary scattering states*:

$$(\hat{H}_0 + \hat{V}) |\psi_{E\eta}^\pm\rangle = E |\psi_{E\eta}^\pm\rangle, \quad (8)$$

where the  $\pm$  in the upper index refers to the so-called *retarded* (+) or *advanced* (-) *Green operators*  $\hat{G}$  used in their definition, see (13), and  $\eta$  denotes the direction of plane wave propagation. We will keep focus on the advanced solution which is pertinent to the incoming state  $|\phi_{\text{IN}}\rangle$ :

$$|\psi(0)\rangle = \lim_{t \rightarrow -\infty} \int_0^\infty dE \sum_{\eta=-1,1} c_{E\eta} |\psi_{E\eta}^+\rangle. \quad (9)$$

The equation (2) can be alternatively expressed as:

$$|\psi(0)\rangle = \hat{U}^+(t) \hat{U}_0(t) |\phi_{\text{IN}}\rangle = |\phi_{\text{IN}}\rangle - \int_{-\infty}^0 dt' \frac{\partial}{\partial t'} \left( \hat{U}^+(t') \hat{U}_0(t') \right) |\phi_{\text{IN}}\rangle = \quad (10)$$

$$= |\phi_{\text{IN}}\rangle - \frac{i}{\hbar} \int_{-\infty}^0 \hat{U}^+(t') \underbrace{\hat{H} - \hat{H}_0}_{\hat{V}} \hat{U}_0(t') |\phi_{\text{IN}}\rangle. \quad (11)$$

By plugging the expanded form of  $|\phi_{\text{IN}}\rangle$  from (7) into the last line of equation (10), and comparing the result with the equation (9), we obtain the *explicit Lippmann-Schwinger equation* (LSE):

$$|\psi_{E\eta}^\pm\rangle = |\phi_{E\eta}\rangle + \underbrace{\frac{1}{E - \hat{H} \pm i\epsilon}}_{\hat{G}^\pm(E)} \hat{V} |\phi_{E\eta}^\pm\rangle. \quad (12)$$

Explicit LSE can be further modified into a—for our intentions preferable—form called the *implicit Lippmann-Schwinger equation*:

$$\left| \psi_{E\eta}^{\pm} \right\rangle = \left| \phi_{E\eta} \right\rangle + \underbrace{\frac{1}{E - \hat{H}_0 \pm i\epsilon}}_{\hat{G}_0^{\pm}(E)} \hat{V} \left| \psi_{E\eta}^{\pm} \right\rangle. \quad (13)$$

Since the functions  $\left| \psi_{E\eta}^{\pm} \right\rangle$  form a complete orthonormal basis set, the following relations hold:

$$1 = \int_{-\infty}^{+\infty} dE \left| \psi_{E\eta}^{\pm} \right\rangle \left\langle \psi_{E\eta}^{\pm} \right|, \quad (14)$$

$$\left\langle \psi_{E\eta}^{\pm} \right| \left| \psi_{E'\eta'}^{\pm} \right\rangle = \delta(E - E') \delta_{\eta\eta'}. \quad (15)$$

The equation (13) can be then expressed in  $x$ -representation followingly:

$$\psi_{E\eta}^{\pm}(x) = \left\langle x \left| \psi_{E\eta}^{\pm} \right\rangle \right. = \phi_{E\eta}^{\pm}(x) + \int_a^b dy \left\langle x \left| \frac{1}{E - \hat{H}_0 \pm i\epsilon} \right| y \right\rangle V(y) \psi_{E\eta}^{\pm}(y). \quad (16)$$

For convenience, we can rescale the equation (16) by a normalization factor  $\sqrt{\frac{m}{2\pi\hbar^2 k}}$  originating from the definition of  $\phi_{E\eta}^{\pm}(x)$  in (6) what gives us:

$$\tilde{\psi}_{E\eta}^{\pm}(x) = e^{\pm ikx} + \int_{\infty}^{-\infty} dy \left\langle x \left| \frac{1}{E - \hat{H}_0 \pm i\epsilon} \right| y \right\rangle V(y) \tilde{\psi}_{E\eta}^{\pm}(y), \quad (17)$$

where  $\psi_{E\eta}^{\pm}(x) = \sqrt{\frac{m}{2\pi\hbar^2 k}} \tilde{\psi}_{E\eta}^{\pm}(x)$ .

$$\left| \phi_{\text{OUT}} \right\rangle = \hat{S} \left| \phi_{\text{IN}} \right\rangle = \underbrace{\int_0^{\infty} dE \sum_{\xi} \left| \phi_{E\eta} \right\rangle \left\langle \phi_{E\eta} \right|}_{1} \hat{S} \underbrace{\int_0^{\infty} dE' \sum_{\xi'} \left| \phi_{E'\eta'} \right\rangle \left\langle \phi_{E'\eta'} \right|}_{1} \left| \phi_{\text{IN}} \right\rangle = \quad (18)$$

$$= \int_0^{\infty} dE \sum_{\xi} \int_0^{\infty} dE' \sum_{\xi'} \left| \phi_{E\eta} \right\rangle \underbrace{\left\langle \phi_{E\eta} \right| \hat{S} \left| \phi_{E'\eta'} \right\rangle}_{\left\langle \psi_{E\eta}^+ \right| \left| \psi_{E'\eta'}^- \right\rangle} \left\langle \phi_{E'\eta'} \right| \left| \phi_{\text{IN}} \right\rangle \quad (19)$$

After several convoluted steps the following expression can be derived:

$$\left| \phi_{\text{OUT}} \right\rangle = \underbrace{\int_0^{\infty} dE \left| \phi_{E(+1)} \right\rangle T_{E(+1)}^+ \left\langle \phi_{E(+1)} \right| \left| \phi_{\text{IN}} \right\rangle}_{\left| \phi_{\text{TR}} \right\rangle} + \underbrace{\int_0^{\infty} dE R_{E(+1)}^+ \left\langle \phi_{E(+1)} \right| \left| \phi_{\text{IN}} \right\rangle}_{\left| \phi_{\text{RF}} \right\rangle}, \quad (20)$$

where  $\left| \phi_{\text{TR}} \right\rangle$  is the transmitted wave-function and  $\left| \phi_{\text{RF}} \right\rangle$  is the reflected wave-function. Both wave-functions are orthogonal to each other. Total probabilities of transmission and reflection correspond to inner products of these functions:

$$P_{\text{TR}} = \left\langle \phi_{\text{TR}} \right| \left| \phi_{\text{TR}} \right\rangle = \int_0^{\infty} |T_{E(+1)}|^2 \cdot |\left\langle \phi_{E(+1)} \right| \left| \phi_{\text{IN}} \right\rangle|^2, \quad (21)$$

$$P_{\text{RF}} = \left\langle \phi_{\text{RF}} \right| \left| \phi_{\text{RF}} \right\rangle = \int_0^{\infty} |R_{E(+1)}|^2 \cdot |\left\langle \phi_{E(+1)} \right| \left| \phi_{\text{IN}} \right\rangle|^2. \quad (22)$$

Since  $\int_0^\infty dE |\langle \phi_{E(+1)} | \phi_{\text{IN}} \rangle|^2 = 1$ , the sum of squares of the reflection and transmission coefficients has to equal one:

$$|T_{E(+1)}|^2 + |R_{E(+1)}|^2 = 1 . \quad (23)$$

Back to our original problem. The Schrödinger equation holds for the renormalized wavefunctions  $|\tilde{\psi}_{E\eta}^\pm\rangle$  as well. Assuming  $\eta = +1$  (i.e. the plane waves are moving from the negative towards the positive part of the  $x$ -axis), and retarded stationary scattering states only, the SchrE then reads:

$$\left( -\frac{\hbar^2}{2m} \nabla_x^2 + V(x) \right) |\tilde{\psi}_{E(+1)}^+\rangle = E |\tilde{\psi}_{E(+1)}^+\rangle . \quad (24)$$

To find the eigenstates, we need to specify the boundary conditions as well:

$$\tilde{\psi}(x \rightarrow +\infty) = T_{E(+1)}^+ \cdot e^{ikx}, \quad (25)$$

$$\tilde{\psi}(x \rightarrow -\infty) = e^{ikx} + R_{E(+1)}^+ e^{-ikx}. \quad (26)$$

Both equations (25)–(26) along with the Schrödinger equation (24) can be divided by the transmission coefficient  $T_{E(+1)}^+$  so we obtain following set of equations:

$$\left( -\frac{\hbar^2}{2m} \nabla_x^2 + V(x) \right) |\bar{\psi}_{E(+1)}^+\rangle = E |\bar{\psi}_{E(+1)}^+\rangle , \quad (27)$$

$$\bar{\psi}(x \rightarrow +\infty) = e^{ikx}, \quad (28)$$

$$\bar{\psi}(x \rightarrow -\infty) = \underbrace{\frac{1}{T_{E(+1)}^+} \cdot e^{ikx}}_A + \underbrace{\frac{R_{E(+1)}^+}{T_{E(+1)}^+} \cdot e^{-ikx}}_B . \quad (29)$$

For the sake of numerical evaluation of the Schrödinger equation (27) constrained by boundary conditions (28)–(29) we will replace the continuous coordinate  $x$  with a discretized set  $\{x_n\}_{n \in \mathbb{N}}$  and adopt the algorithm of propagation on the grid using the relation:

$$\bar{\psi}(x_{n+1}) + \bar{\psi}(x_{n-1}) = 2 \cdot \left( 1 - \frac{m(\Delta x)^2}{\hbar^2} \cdot (E - V(x_n)) \right) \bar{\psi}(x_n). \quad (30)$$

The formula (30) can be used to iterate through all  $x_n$  down to some sufficiently distant  $x_1$  and  $x_2$  where we assume the condition (29). We can then easily find the coefficients  $A, B$  and consequently the  $T_{E(+1)}^+$  and  $R_{E(+1)}^+$  as well. One of the possible approaches is the following matrix inversion:

$$\begin{pmatrix} \bar{\psi}(x_1) \\ \bar{\psi}(x_2) \end{pmatrix} = \begin{pmatrix} e^{ik(E)x_1} & e^{-ik(E)x_1} \\ e^{ik(E)x_2} & e^{-ik(E)x_2} \end{pmatrix} \cdot \begin{pmatrix} A \\ B \end{pmatrix} \quad (31)$$

$$\begin{pmatrix} A \\ B \end{pmatrix} = \begin{pmatrix} e^{iKx_1} & e^{-iKx_1} \\ e^{iKx_2} & e^{-iKx_2} \end{pmatrix}^{-1} \cdot \begin{pmatrix} \bar{\psi}(x_1) \\ \bar{\psi}(x_2) \end{pmatrix} \quad (32)$$

The initial condition is, in a similar manner, derived from the boundary condition (28) such that for  $x_N \rightarrow \infty$  we can write:

$$\bar{\psi}(x_N) = e^{ikx_N}, \quad (33)$$

$$\bar{\psi}(x_{N-1}) = e^{ikx_{N-1}}, \quad (34)$$

where  $k = \frac{\sqrt{2mE}}{\hbar}$ .

## 2.2 Resonances as Meta-stable States

Meta-stable states can be regarded as nearly bound states, i.e. bound states with a finite lifetime. Hence, we firstly focus solely on the bound states. Let us consider a standard 1D Schrödinger equation:

$$\left( -\frac{\hbar^2}{2m} \nabla_x^2 + V(x) \right) \psi(x) = E\psi(x) \quad (35)$$

We are looking for solutions that are discrete and quadratically integrable, and thus asymptotically converging to zero. As a result of these conditions, we can expect the following solution in the left ( $-\infty$ ) and right ( $+\infty$ ) asymptotic regions:

$$\begin{aligned} \psi(x \rightarrow +\infty) &= Ae^{\kappa x} + Be^{-\kappa x} & \rightarrow A = 0, \\ \psi(x \rightarrow -\infty) &= Ce^{\kappa x} + De^{-\kappa x} & \rightarrow D = 0, \end{aligned}$$

where  $\kappa^2 = -\frac{2mE}{\hbar^2}$ . The reduction of general solutions into just a single exponential on both side of the asymptotic region is a result of the abovementioned convergence condition. The resulting condition is then called the *Siegert boundary condition*. As can be seen, the parameter kappa belongs to complex numbers,  $\kappa = i\frac{\sqrt{2mE}}{\hbar}$ . Let us now define another complex parameter  $K = i\kappa$  and allow the energy  $E$  to be complex as well. It then follows that:

$$K = K_R + iK_I \implies E = \frac{\hbar^2}{2m} (K_R + iK_I)^2 = \quad (36)$$

$$= \underbrace{\frac{\hbar^2}{2m} (K_R^2 - K_I^2)}_{\text{Re}[E]} + i \underbrace{\frac{\hbar^2}{m} (K_R K_I)}_{\text{Im}[E]}. \quad (37)$$

The imaginary part of the energy is also related to the lifetime  $\tau$  of the pertinent state by:

$$\begin{aligned} \text{Im } E &\equiv -\frac{\Gamma}{2} = \frac{1}{2\tau} & \implies E = \mathcal{E} - i\frac{\Gamma}{2}. \end{aligned} \quad (38)$$

The eigenenergy also relates to the profile of the square of transition coefficient by the *Breit-Wigner profile*:

$$f_{\text{B-W}}(E) = \frac{\frac{\Gamma^2}{4}}{(E - \mathcal{E})^2 + \frac{\Gamma^2}{4}}. \quad (39)$$

The Siegert states in general becomes:

$$\psi(x \rightarrow \infty) \propto e^{(iK_R - K_I)x} \quad (40)$$

$$\psi(x \rightarrow -\infty) \propto e^{-(iK_R - K_I)x} \quad (41)$$

Several other conditions stem from the above expressions, upon which four categories of Siegert states can be distinguished. Depending on the values of real and imaginary part of the variable  $K$ . The categories are summarised in Table 1.

**Table 1:** Summary of Siegert states categorisation based on the values of real and imaginary part of the complex parameter  $K$ . The graphical depiction can be found in Figure 1.

	Im $K < 0$	Im $K = 0$	Im $K > 0$
Re $K < 0$	anti-resonances	$\times^*$	$\times^\#$
Re $K = 0$	anti-bound	$\times^\dagger$	bound
Re $K > 0$	resonances	$\times^*$	$\times^\#$

\* Wronskian of  $\psi(x)$  would not be conserved;

#  $\psi(x)$  would not be quadratically integrable;

† trivial solution

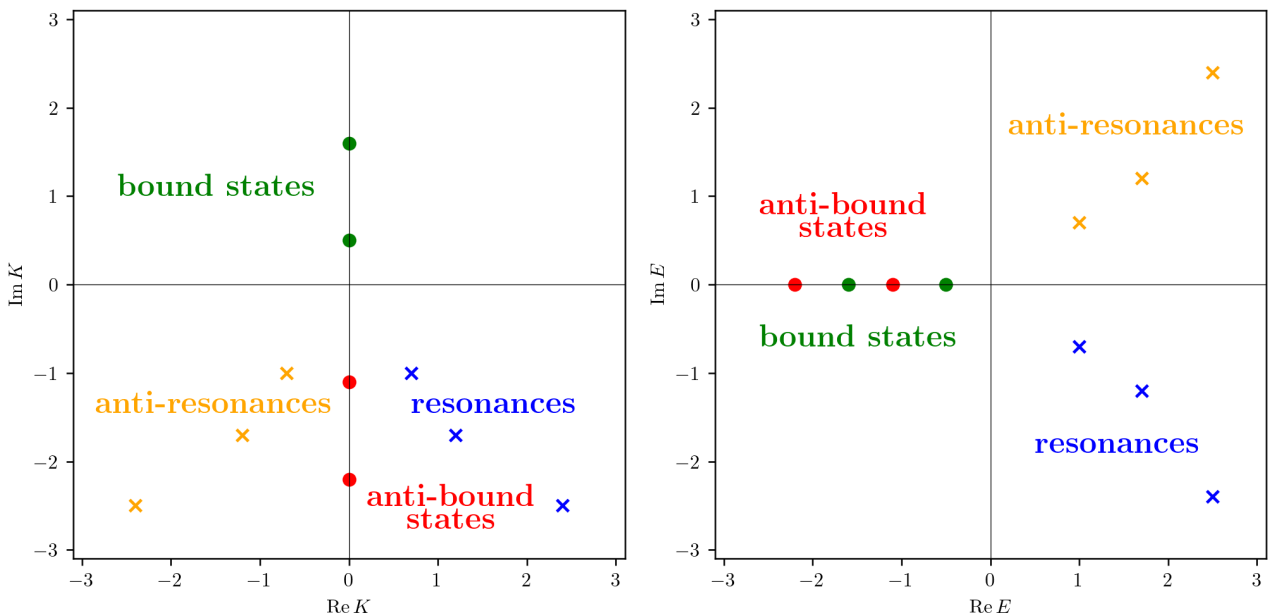


**Figure 1:** Illustrative graphical depiction of four different types of Siegert states on a complex plane depending on the values of parameter  $K$  (left), and similarly energy  $E$  (right).

The bound states can be calculated easily by expanding the sought wave-function into a fixed complete basis set of size  $N$ . The problem than reduces into a diagonalisation of  $N \times N$  Hermitian matrix. For more details see subsection 3.1. However, to calculate the resonances—or meta-stable states—analytically, we need to abandon the Hilbert space and Hermitian formalism and adopt the non-Hermitian formalism instead. The subsequent assumptions will result in the *complex scaling method*, see the following subsection 2.3.

### 2.3 Complex Scaling

In the previous section we allowed the energy to be complex. That introduced a new possibility of a divergency caused by the imaginary part of argument  $K$  in the exponential if it is negative.

$$\psi(x \rightarrow \pm\infty) \propto e^{\mp Kx} = e^{\pm iKx} \quad (42)$$

$$= e^{\pm(iK_R - K_I)x} = \quad (43)$$

$$= e^{\pm iK_R x} \underbrace{e^{\mp K_I x}}_{\text{divergent}} \quad (44)$$

$$\Leftrightarrow$$

$$K_I < 0$$

That is to say, Siegert states with negative imaginary part of the argument  $K$  are going to explode—do not converge—in the asymptotic regions. Hence, they are not quadratically integrable and neither they belong to Hilbert space.

That might be seen as a problem at first glance. But it is not that a big deal in fact. For example, the well-known plane waves are not square integrable either. But a wavepacket—a linear combination of plane waves—square integrable already is.

The complex scaling method—as its name suggests—approaches the problem differently. Besides allowing the energy to be a complex number, we add a complex phase factor  $\theta$  to the coordinate  $x$ :

$$x \rightarrow xe^{i\theta}. \quad (45)$$

This effectively correspond to a rotation in the complex plane by the angle  $\theta$ . We can find the following consequences:

$$\psi(x \rightarrow \pm\infty) \propto e^{\pm iKx} = e^{\pm i(K_R + iK_I)x(\cos\theta + i\sin\theta)} = \quad (46)$$

$$= \underbrace{e^{\pm ix(K_R \cos\theta - K_I \sin\theta)}}_{\text{oscillating phase}} \underbrace{e^{\mp x(K_I \cos\theta + K_R \sin\theta)}}_{?}, \quad (47)$$

where we used the relation  $e^{i\theta} = \cos\theta + i\sin\theta$ . There arises a question from the equation (47): For what value of  $\theta$  the last exponential will start to converge? We want the following inequality to be fulfilled:

$$-|K_I|\cos\theta + K_R\sin\theta \geq 0 \quad (48)$$

$$\tan\theta \geq \frac{|K_I|}{K_R} \quad (49)$$

$$\arctan\left(\frac{|K_I|}{K_R}\right) \geq \theta \quad (50)$$

The fraction can be then expressed in terms of the energy, based on the equation (37), as:

$$\left( \frac{\operatorname{Re} E \pm \sqrt{(\operatorname{Re} E)^2 + (\operatorname{Im} E)^2}}{\operatorname{Im} E} \right) \geq \tan\theta \quad (51)$$

Alternatively to the eq. (37), we can write the following for the resonances (where we expect negative imaginary part of  $K$ ):

$$K = |K|e^{-i\phi} \rightarrow E = \frac{\hbar^2}{2m} K^2 = \frac{\hbar^2}{2m} |K|^2 e^{-2i\phi} \quad (52)$$

$$= \underbrace{|K|^2 \cos 2\phi}_{\text{Re } E} - i \underbrace{|K|^2 \sin 2\phi}_{\text{Im } E} \quad (53)$$

From eq. (53) then follows the expression for angle  $\phi$ :

$$2\phi = \arctan \left( -\frac{\text{Im } E}{\text{Re } E} \right), \quad (54)$$

what directly implies:

$$\frac{\text{Im } E}{\text{Re } E} = -\tan 2\phi = -\frac{\sin 2\phi}{\cos 2\phi}, \quad \frac{\text{Im } E}{|E|} = \sin 2\phi. \quad (55)$$

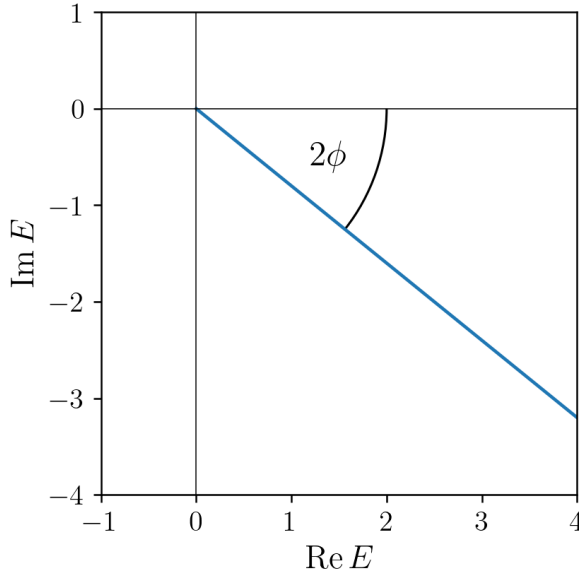


**Figure 2:** Visualization of the angle  $\phi$  significance (see eqs. (52) and (54) for context) in relation to the values of energy plotted on complex plane.

By plugging eqs. (55) into eq. (51) we obtain the first relation between  $\theta$  and  $\phi$ :

$$\tan \theta \leq -\frac{\cos 2\phi \pm 1}{\sin 2\phi} \quad (56)$$

$$(57)$$

what doesn't seem to be that much useful. Thus, in order to shed more light on the angle  $\theta$ , we can further expand the eq. (48) using the relation  $K = |K|e^{-i\phi} = |K|(\cos \phi - i \sin \phi)$ :

$$0 \leq -\sin \phi \cos \theta + \cos \phi \sin \theta \quad (58)$$

$$\leq \sin(\theta - \phi) \quad (59)$$

$$\Rightarrow 0 \leq (\theta - \phi) \leq \pi \pmod{2\pi} \quad (60)$$

$$\Rightarrow \phi \leq \theta \leq \phi + \pi \quad (61)$$

That means the angle  $\phi$  actually corresponds to some critical value of scaling angle  $\theta$ . We will denote it  $\theta_C = \phi$ . To conclude, rotating the coordinate  $x$  by the angle  $\theta$  results in unraveling, and making convergent and square integrable all wavefunctions corresponding to energies rotated on the complex plane by up to an angle  $-2\theta$ .

We can finally plug the eq. (45) into the 1D SchrE and we obtain:

$$\left( -\frac{\hbar^2}{2m} \frac{d^2}{dx^2} e^{-2i\theta} + V(xe^{i\theta}) \right) \psi(xe^{i\theta}) = E\psi(xe^{i\theta}), \quad (62)$$

where the first term comes from  $\frac{d^2}{d(xe^{i\theta})^2} = \frac{d^2}{d(x^2e^{2i\theta})} = \frac{d^2}{dx^2} e^{-2i\theta}$ . As can be seen, the energy does not depend on the angle of complex rotation  $\theta$  in contrast to the wavefunctions. The transition (45) can be described as an action of some operator of complex rotation  $\hat{S}_\theta$  such that:

$$\hat{S}_\theta \psi(x) \propto \psi(xe^{i\theta}). \quad (63)$$

For Schrödinger equation we can then write:

$$\hat{S}_\theta \hat{H} \underbrace{\hat{S}_\theta^{-1} \hat{S}_\theta}_{\mathbf{1}} \psi(x) = E\psi(xe^{i\theta}) \quad (64)$$

$$\hat{H}_\theta \psi(xe^{i\theta}) = E\psi(xe^{i\theta}), \quad (65)$$

where  $\hat{H}_\theta = \hat{S}_\theta \hat{H} \hat{S}_\theta^{-1}$  represents a similarity transformation of Hamiltonian  $\hat{H}$  into a non-Hermitian form, i.e.  $\hat{H}_\theta \neq \hat{H}_\theta^{-1}$ . The operator of rotation  $\hat{S}_\theta$  on complex plane by an angle  $\theta$  can be derived from the assumption of a series of subsequent infinitesimal rotations by an angle  $d\theta = \frac{\theta}{N}$ :

$$\psi(xe^{id\theta}) = \psi(x + ix d\theta) = \psi(x) + ix d\theta \frac{\partial \psi(x)}{\partial x} = \underbrace{\left( \mathbf{1} + ix d\theta \frac{\partial}{\partial x} \right)}_{\hat{S}'_{d\theta}} \psi(x), \quad (66)$$

$$\implies \hat{S}'_\theta = \left( \hat{S}'_{d\theta} \right)^N = \left( \mathbf{1} + ix\theta \frac{\partial}{\partial x} \right)^N = e^{ix\theta \frac{\partial}{\partial x}}. \quad (67)$$

Actually, we append yet another factor to the last term of eq. (67) representing the phase. The final form of the complex scaling operator then reads:

$$\hat{S}_\theta := e^{i\frac{\theta}{2}} e^{ix\theta \frac{\partial}{\partial x}}. \quad (68)$$

### 2.3.1 Scalar Product and C-Product

In the standard formulation of quantum theory, the inner product of two functions from the Hilbert space has the form of a scalar product:

$$\langle \psi^{(i)} | \psi^{(j)} \rangle = \int_{-\infty}^{\infty} \left( \psi^{(i)}(x) \right)^* \psi^{(j)}(x) dx. \quad (69)$$

If  $\psi^{(i)}, \psi^{(j)}$  represent eigenfunctions of a Hermitian operator, they are orthogonal to each other, and their corresponding eigenvalues are real numbers. However, we have shown that Siegert eigenstates corresponding to for example resonances are not from Hilbert space of square integrable functions and

their eigenenergies have non-zero imaginary part. And even though the motivation of the complex scaling method was to make these states square integrable by rotating the coordinate  $x$  in the complex plane by angle  $\theta$ , by doing so we introduced another little issue. That is, the scaled Hamiltonian  $\hat{H}_\theta$  is non-Hermitian (see eq. (65)). To ensure similar properties known from the Hermitian world (e.g. the orthogonality of eigenstates, completeness relation), a generalised form of the scalar product called the  $\mathbb{C}$ -product needs to be introduced:

$$\left( \psi_\theta \middle| \psi'_\theta \right) = \int_{-\infty}^{\infty} \psi_\theta(x) \psi'_\theta(x) \, dx, \quad (70)$$

where  $\hat{S}_\theta \psi(x) = e^{i\frac{\theta}{2}} \psi(xe^{i\theta}) \equiv \psi_\theta$ . We can now proof that the  $\mathbb{C}$ -product formulation ensures the orthogonality of resonances eigenstates.

Let us have two resonances eigenstates  $\psi_\theta^{(1)}(x)$ ,  $\psi_\theta^{(2)}(x)$ , complex-scaled by an angle  $\theta$ . We want to proof that:

$$0 \equiv \left( \psi_\theta^{(1)}(x) \middle| \psi_\theta^{(2)}(x) \right) = \quad (71)$$

$$= \int_{-\infty}^{\infty} dx \, e^{i\theta} \psi^{(1)}(xe^{i\theta}) \psi^{(2)}(xe^{i\theta}) = \quad | \quad z := xe^{i\theta}; \, dz = e^{i\theta} dx; \, z \in \mathbb{C} \quad (72)$$

$$= \int_{\gamma_C} dz \, \psi^{(1)}(z) \psi^{(2)}(z). \quad (73)$$

Since both functions  $\psi^{(1,2)}(z)$  are now square integrable and converging to zero in the asymptotic region, we can construct a closed loop (contour, see Figure 3) in the complex plane and use the Cauchy integral theorem<sup>1</sup>. The orthogonality of resonance eigenstates shall be thus considered proven.

## 2.4 Interaction with Light

The third part of the report studies the bound states in the presence of light. This gives origin to a different type of metastable states called *Feshbach resonances* in contrast to the so-called *shape resonances* introduced in subsection 2.2.

### 2.4.1 Interaction Hamiltonian

The Hamiltonian of irradiated system interacting with light reads:

$$\hat{H} = \frac{1}{2m} \left( \hat{\vec{p}} - \frac{q}{\epsilon_0} \hat{\vec{A}}(t) \right)^2 + V(x), \quad (74)$$

where  $\hat{\vec{A}}(t)$  is the vector potential of electro-magnetic field in the dipole approximation<sup>2</sup> stemming from the Maxwell equations. The representation presented in eq. (74) is called the *momentum gauge* (MG), or the *minimum coupling Hamiltonian*.

The bracket in eq. (74) can be further expanded into

---

<sup>1</sup>Cauchy integral theorem states that a contour integral of a function  $f(z)$  holomorphic (i.e. including analytical) in a complex domain enclosed by the contour  $\gamma_C$  equals zero:  $\oint_{\gamma_C} f(z) \, dz = 0$ .

<sup>2</sup>The dipole approximation assumes that the usual characteristic size of the interacting system (e.g. an atom or a molecule) is far smaller than the wavelength of the incoming light and thus the vector potential can be considered constant over that region. That is  $\hat{A}(x, t) \approx \hat{A}(t)$ .

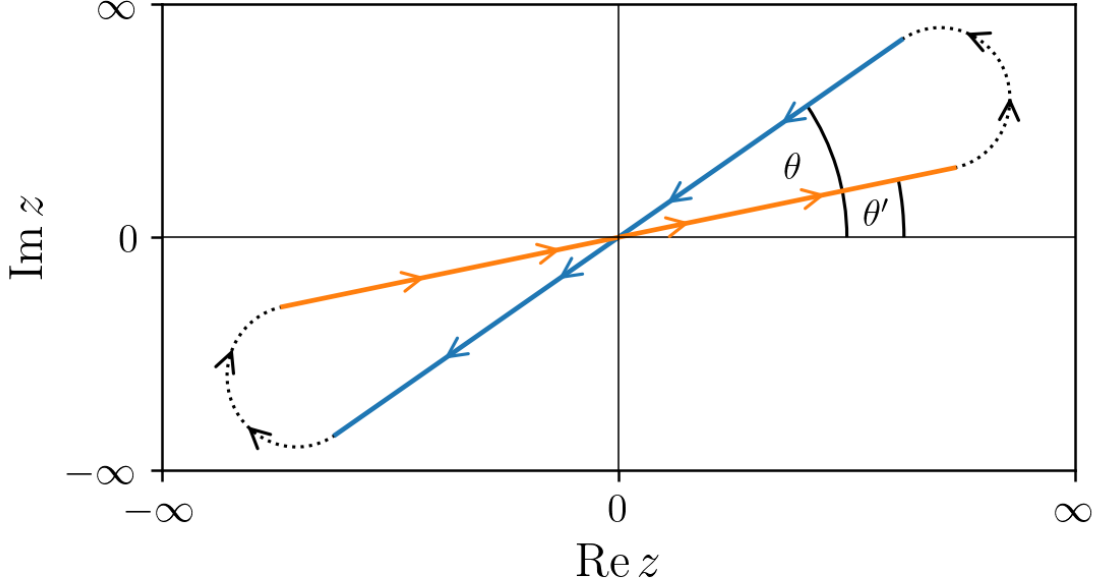


**Figure 3:** Plot of a closed contour constructed from the originally real coordinate axis  $x$  rotated by two slightly different angles  $\theta, \theta'$  (solid straight lines). The two connections between them (dotted black line) is possible to make in the asymptotic regions because the functions  $\psi(z)$  are assumed to be already well-converged there.

$$\hat{H} = \underbrace{\frac{\hat{p}^2}{2m}}_{\hat{H}_0} + V(x) - \underbrace{\frac{q}{2m\epsilon_0}\hat{p}A(t)}_{H_I(t)} + \underbrace{\frac{q^2}{2m\epsilon_0^2}A^2(t)}_{H_A(t)}. \quad (75)$$

Solving the Schrödinger equation corresponding to the last term of the Hamiltonian denoted  $H_A(t)$  gives a rather simple exponential prefactor. We can get rid of it by introducing an appropriate transformation of the momentum gauge Hamiltonian eigenfunction  $\psi_{\text{MG}}(t)$  resulting in the so-called *reduced momentum gauge* (RMG):

$$\psi_{\text{RMG}}(t) = e^{-\frac{i}{\hbar}\frac{q^2}{2m\epsilon_0^2}\int_{t_0}^t d\tau A^2(\tau)} \cdot \psi_{\text{MG}}(t). \quad (76)$$

In a similar manner, we can introduce yet another transformation:

$$\psi_{\text{LG}} = e^{-\frac{i}{\hbar}\frac{q}{c_0}A(t)x} \cdot \psi_{\text{MG}}(t), \quad (77)$$

what represents the so-called *length gauge*. The Hamiltonian then becomes:

$$H_{\text{LG}} = H_0 - qx\hat{E}(t). \quad (78)$$

The last gauge worth of mentioning here is the *acceleration gauge* (AG), also called the Kramers-Henneberger gauge:

$$\psi_{\text{AG}}(t) = e^{-\frac{i}{\hbar}\int f(t)\hat{p}} \cdot \psi_{\text{RMG}}(t), \quad (79)$$

with the corresponding Hamiltonian  $H_{\text{AG}}$ :

$$H_{\text{AG}} = \frac{\hat{p}^2}{2m} + V(x + f(t)) , \quad (80)$$

where  $f(t) = \frac{q}{mc_0} \int_{t_0}^t d\tau A(\tau)$ . Taylor expansion of  $V(x)$  around  $x = 0$  up to the first order gives:

$$H_{\text{AG}} = \frac{\hat{p}^2}{2m} + V(x) + f(t)V'(x) \quad (81)$$

$$= H_0 + f(t)V'(x) . \quad (82)$$

The  $V'(x)$  stands for the derivative of the potential what corresponds to the force—or let us say acceleration—what gives the gauge its usual name.

To sum up the various gauges, Table 2 presents the comparison between all introduced gauges.

**Table 2:** Summary of all introduced gauges and equivalent representations of both the Hamiltonian  $H$  and wavefunctions  $\psi$  of a system interacting with an electro-magnetic field described by the vector potential in the dipole approximation<sup>2</sup>  $A(t)$ . The presented gauges are momentum gauge (MG), reduced momentum gauge (RMG), length gauge (LG), and acceleration gauge (AC).

	$H$	$\psi$
MG	$\frac{(\hat{p}-qA(t))^2}{2m} + V(x)$	$\psi_{\text{MG}}(x, t)$
RMG	$\frac{\hat{p}^2}{2m} + V(x) - \frac{q\hat{p}A(t)}{m}$	$e^{-\frac{i}{\hbar}g(t)} \cdot \psi_{\text{MG}}(x, t)$
LG	$\frac{\hat{p}^2}{2m} + V(x) - q\hat{x}E(t)$	$e^{-\frac{i}{\hbar}\frac{q}{c_0}A(t)\hat{x}} \cdot \psi_{\text{MG}}(x, t)$
AG	$\frac{\hat{p}^2}{2m} + V(x + f(t))$	$e^{-\frac{i}{\hbar}f(t)\hat{p}} \cdot e^{-\frac{i}{\hbar}g(t)} \cdot \psi_{\text{MG}}(x, t)$

$$g(t) = \frac{q^2}{2mc_0^2} \int_{t_0}^t d\tau A^2(\tau) ;$$

$$f(t) = \frac{q}{mc_0} \int_{t_0}^t d\tau A(\tau) ;$$

$$E(t) = -\frac{1}{c_0} \frac{\partial A(t)}{\partial t} ;$$

For our purposes, we will assume the incoming light in terms of a semi-classical approximation—corresponding to e.g. a monochromatic laser:

$$A(t) = A_0 \sin(\omega t) , \quad (83)$$

$$E(t) = -\frac{\omega}{c_0} A_0 \cos(\omega t) \equiv \mathcal{E}_0 \cos(\omega t) , \quad (84)$$

$$f(t) = \frac{q}{mc_0} A_0 \frac{\cos(\omega t)}{\omega} \equiv \alpha_0 \cos(\omega t) . \quad (85)$$

The further used Hamiltonian in the acceleration gauge thus becomes:

$$H = \frac{p^2}{2m} + V(x) + V'(x)\alpha_0 \cos(\omega t) \cdot F(t) , \quad (86)$$

where  $F(t)$  is an envelope of the laser beam, e.g. a Gaussian function.

### 2.4.2 Standard Floquet Theory

The Hamiltonian presented in eq. (86) is noticeably periodic in time due to the function  $\cos(\omega t)$  in the last term. Therefore, the Floquet time-dependent theory for time-periodic Hamiltonians can be adopted to provide a straightforward tool for solving the Schrödinger equation. The theory will be derived there just briefly, following the argumentation from lecture notes of Santoro (2019).

Let us start with a time-dependent Schrödinger equation

$$i\hbar \frac{\partial}{\partial t} |\psi(t)\rangle = \hat{H}(t) |\psi(t)\rangle \quad (87)$$

where the Hamiltonian is time periodic,  $\hat{H}(t_0) = \hat{H}(t_0+T)$ . We can write the time-evolution operator  $U(t_2, t_2)$  along with some of its properties that imply from the periodicity:

$$U(t_1, t_0) \equiv e^{-\frac{i}{\hbar} \hat{H}(t_1-t_0)}, \quad (88)$$

$$|\psi(t_1)\rangle = U(t_1, t_0) |\psi(t_0)\rangle, \quad (89)$$

$$U(t_1 + nT, t_0) \equiv U(t_1, t_0) \left( U(t_0 + T, t_0) \right)^n, \quad (90)$$

$$U_{t_0}^{(T)} \equiv U(t_0 + T, t_0) = e^{-\frac{i}{\hbar} \hat{H}_{t_0}^{(T)} T}. \quad (91)$$

The last relation, eq. (91), defines the one-period time-evolution operator  $U_{t_0}^{(T)}$ , which is dependent on the initial time  $t_0$  and propagates the system to time  $t_0 + T$ . The Hamiltonian  $\hat{H}_{t_0}^{(T)}$  is Hermitian since  $U_{t_0}^{(T)}$  is unitary, and its eigenstates represent the so-called *Floquet modes* that form a complete basis set for the *Floquet states*:

$$\hat{H}_{t_0}^{(T)} |\varphi_j(t_0)\rangle = \epsilon_j |\varphi_j(t_0)\rangle, \quad (92)$$

$$U_{t_0}^{(T)} |\varphi_j(t_0)\rangle = e^{-\frac{i}{\hbar} \hat{H}_{t_0}^{(T)} T} |\varphi_j(t_0)\rangle = \quad (93)$$

$$= e^{-\frac{i}{\hbar} \epsilon_j T} |\varphi_j(t_0)\rangle. \quad (94)$$

The energies  $\epsilon_j$  are called quasienergies since their value is defined modulo  $E = \hbar\Omega = \frac{2\pi\hbar}{T}$ . We can also construct an unitary periodic evolution operator  $P(t_1, t_0)$  such that:

$$U(t_1, t_0) = \underbrace{U(t_1, t_0) e^{\frac{i}{\hbar} \hat{H}_{t_0}^{(T)} (t_1-t_0)}}_{P(t_1, t_0)} \overbrace{e^{-\frac{i}{\hbar} \hat{H}_{t_0}^{(T)} (t_1-t_0)}}^{\mathbb{1}}, \quad (95)$$

$$P(t_1, t_0) \equiv U(t_1, t_0) \cdot e^{\frac{i}{\hbar} \hat{H}_{t_0}^{(T)} (t_1-t_0)}. \quad (96)$$

The main difference between the evolution operators  $U(t_1, t_0)$  and  $P(t_1, t_0)$  can be presented for  $t_1 = t_0 + T$ :

$$U(t_0 + T, t_0) = e^{-\frac{i}{\hbar} \hat{H}_{t_0}^{(T)} T} \quad (97)$$

$$P(t_0 + T, t_0) = U(t_0 + T, t_0) \cdot e^{\frac{i}{\hbar} \hat{H}_{t_0}^{(T)} T} = U_{t_0}^{(T)} \left( U_{t_0}^{(T)} \right)^+ = \mathbb{1} \quad (98)$$

Since  $P(t_0 + T, t_0) = P(t_0, t_0)$ , the Floquet modes  $|\varphi_j(t)\rangle$  are periodic in a same way. They can be used to define a complete basis set of Floquet states  $\{|\psi_j(t)\rangle\}_{j=1}^{\infty}$  in the Hilbert space such that:

$$|\psi_j(t)\rangle = U(t_0 + t, t_0) |\varphi_j(t_0)\rangle \stackrel{(95)}{=} P(t, t_0) e^{-\frac{i}{\hbar} \hat{H}_{t_0}^{(T)}(t-t_0)} |\varphi_j(t_0)\rangle = \quad (99)$$

$$= e^{-\frac{i}{\hbar} \epsilon_j(t-t_0)} P(t, t_0) |\varphi_j(t_0)\rangle = \quad (100)$$

$$= e^{-\frac{i}{\hbar} \epsilon_j(t-t_0)} |\varphi_j(t)\rangle , \quad (101)$$

where we defined  $|\varphi_j(t_1)\rangle \equiv P(t_1, t_0) |\varphi_j(t_0)\rangle$  and thus  $|\varphi_j(t+T)\rangle = |\varphi_j(t)\rangle$ . Any state  $|\psi(t)\rangle$  can be then expressed as

$$|\psi(t_0)\rangle = \sum_j |\varphi_j(t_0)\rangle \langle \varphi_j(t_0)|\psi(t_0)\rangle = \quad (102)$$

$$= \sum_j C_j |\varphi_j(t_0)\rangle , \quad (103)$$

$$|\psi(t)\rangle = \sum_j C_j e^{-\frac{i}{\hbar} \epsilon_j(t-t_0)} |\varphi_j(t)\rangle . \quad (104)$$

Note that the expansion into the Floquet modes (102–104) is still dependant on the initial time parameter  $t_0$  as well.

The time-dependent Schrödinger equation for the Floquet states reads:

$$i\hbar \frac{\partial}{\partial t} |\psi(t)\rangle \stackrel{(104)}{=} i\hbar \left( \frac{\partial}{\partial t} e^{-\frac{i}{\hbar} \epsilon_j(t-t_0)} \right) |\varphi_j(t)\rangle + i\hbar e^{-\frac{i}{\hbar} \epsilon_j(t-t_0)} \left( \frac{\partial}{\partial t} |\varphi_j(t)\rangle \right) = \quad (105)$$

$$= \epsilon_j |\psi_j(t)\rangle + i\hbar e^{-\frac{i}{\hbar} \epsilon_j(t-t_0)} \left( \frac{\partial}{\partial t} |\varphi_j(t)\rangle \right) \quad (106)$$

$$= H(t) |\psi_j(t)\rangle \quad (107)$$

$$\Rightarrow \underbrace{\left( H(t) - i\hbar \frac{\partial}{\partial t} \right)}_{\mathcal{H}_F} |\varphi_j(t)\rangle = \epsilon_j |\varphi_j(t)\rangle , \quad (108)$$

where the Floquet Hamiltonian  $\mathcal{H}_F$  was introduced and Floquet modes  $|\varphi_j(t)\rangle$  represent its eigenstates with eigenvalues  $\epsilon_j$ . In contrast, the Floquet states  $|\psi_j(t)\rangle$  are eigenstates of the original time-periodic Hamiltonian  $H(t)$ .

If we multiply an arbitrary Floquet mode by a complex exponential factor oscillating with a frequency  $m\omega$ , the new such state is also an eigenstate of the Floquet Hamiltonian but its eigenvalue is now shifted by  $m\hbar\omega$ :

$$\mathcal{H}_F \left( e^{im\Omega(t-t_0)} |\varphi_j(t)\rangle \right) = (\epsilon_j + m\hbar\Omega) \left( e^{im\Omega(t-t_0)} |\varphi_j(t)\rangle \right) \quad (109)$$

However, such multiplicative factor does not influence the corresponding Floquet state  $|\psi_j(t)\rangle$ :

$$|\psi_j(t)\rangle = e^{-\frac{i}{\hbar} (\epsilon_j + m\hbar\Omega)(t-t_0)} \left( e^{im\Omega(t-t_0)} |\varphi_j(t)\rangle \right) = \quad (110)$$

$$= e^{-\frac{i}{\hbar} \epsilon_j(t-t_0)} |\varphi_j(t)\rangle \quad (111)$$

The adopted Floquet theory solving procedure is similar to the one described in subsection 3.1 and stems from expansion to a basis set. The problem is then expressed in terms of vectors and matrices and solution is found by diagonalizing the Hamiltonian matrix. In this case, the Fourier basis was used:

$$\psi(x, t) = \sum_{\nu=-N}^N e^{i\nu\omega t} \varphi_\nu(x), \quad \frac{1}{T} \int^T dt e^{-i\nu\omega t} e^{i\nu'\omega t} = \delta_{\nu\nu'} . \quad (112)$$

The Schrödinger equation then reads:

$$\left( \frac{p^2}{2m} + V(x) + V'(x)\alpha_0 \cos(\omega t) - i\hbar \frac{\partial}{\partial t} \right) \sum_{\nu} e^{i\nu\omega t} \varphi_\nu(x) = \epsilon_{\nu} \sum_{\nu} e^{i\nu\omega t} \varphi_\nu(x) \quad \left| \int^T e^{-i\nu'\omega t} \right. \quad (113)$$

$$\left( \frac{p^2}{2m} + V(x) + \nu' \hbar \omega \right) \varphi_{\nu'}(x) + V'(x)\alpha_0 \underbrace{\frac{1}{T} \int^T dt \frac{e^{i\omega t} + e^{-i\omega t}}{2} e^{-i\nu'\omega t} e^{i\nu'\omega t}}_{\delta_{\nu\pm 1, \nu'}} \varphi_{\nu}(x) = \epsilon_{\nu} \varphi_{\nu'}(x) \quad (114)$$

$$\underbrace{\left( \frac{p^2}{2m} + V(x) + \nu' \hbar \omega \right)}_{H_0} \varphi_{\nu'}(x) + V'(x)\alpha_0 \left( \varphi_{\nu'+1}(x) + \varphi_{\nu'-1}(x) \right) = \epsilon_{\nu} \varphi_{\nu'}(x) . \quad (115)$$

The Hamiltonian in (115) can now be expressed as a matrix of dimension  $N \times N$ . On top of that, the expansion of states  $\varphi_{\nu}(x)$  by yet another basis set  $\left\{ b_k^{(\nu)}(x) \right\}_{k=1}^K$  can be performed, what directly corresponds to the step described in subsection 3.1. As a result, we obtain a rather convoluted matrix object (a Floquet matrix) of dimensions  $(N \cdot K) \times (N \cdot K)$ .

Elements pertinent to a single value of index  $\nu$  form a so-called channel. The last term on the LHS of eq. (115) then corresponds to an inter-channel coupling controlled by the value of parameter  $\alpha_0$ .

Diagonalization of the Floquet matrix (115) provides  $N$  shifted copies of  $K$  eigenvalues and eigenstates—please see the section of results for images of the calculated results.

### 2.4.3 Non-Hermitian Floquet Theory

The complex-scaling approach can be used with the Floquet theory as well. The motivation and derivation procedure is roughly the same as was already discussed in subsection 2.3. This leads us to the complex-scaled Floquet Hamiltonian  $\mathcal{H}_F^\theta$ :

$$\mathcal{H}_F^\theta = H^\theta(t) - i\hbar \frac{\partial}{\partial t} = \quad (116)$$

$$= -\frac{\hbar^2}{2m} e^{-2i\theta} \nabla_x^2 + V(xe^{i\theta}) + \alpha \cos(\omega t) V'(xe^{i\theta}) - i\hbar \frac{\partial}{\partial t} . \quad (117)$$

The resulting complex-scaled Floquet matrix (also called the coupled-channels Schrödinger equation in matrix representation) then becomes

$$\left( -\frac{\hbar^2}{2m} e^{-2i\theta} \nabla_x^2 + V(xe^{i\theta}) + \nu \hbar \omega \right) \varphi_{\nu}(xe^{i\theta}) + V'(xe^{i\theta}) \alpha_0 \left( \varphi_{\nu+1}(xe^{i\theta}) + \varphi_{\nu-1}(xe^{i\theta}) \right) = \epsilon_{\nu} \varphi_{\nu}(xe^{i\theta}) . \quad (118)$$

Similarly to the hermitian Floquet theory, the eigenvalues and eigenstates of the Schrödinger equation can be obtained by diagonalizing the Floquet matrix (118) and Table 3. For more clarification please see the relevant figures in the section of results.

**Table 3:** Outline of the Floquet matrix from equation (115) (and similarly in the case of complex-scaling Floquet matrix from eq. 118). Each matrix element then corresponds to a  $K \times K$  matrix in the basis of states

$\nu$	...	-1	0	1	...
:	$\ddots$	$\frac{\alpha_0}{2} V'$		$\dots$	0
-1	$\frac{\alpha_0}{2} V'$	$H_0 - 1\hbar\omega$	$\frac{\alpha_0}{2} V'$		$\ddots$
0		$\frac{\alpha_0}{2} V'$	$H_0$	$\frac{\alpha_0}{2} V'$	
1	$\vdots$		$\frac{\alpha_0}{2} V'$	$H_0 + 1\hbar\omega$	$\frac{\alpha_0}{2} V'$
:	0	$\dots$		$\frac{\alpha_0}{2} V'$	$\ddots$

#### 2.4.4 Exceptional Points (EP)

The value of eigenenergies depends on two main parameters—the strength of the light-matter interaction  $\alpha_0$  (proportional to the light intensity), and the frequency of the incoming light  $\omega$  (for a monochromatic laser). As ?? shows, the energies plotted on a complex plane move all around as these two parameters are being varied. Let pose a question, for what values of  $\alpha_0$  and  $\omega$  will some two energies overlap and become degenerate?

To answer that question, let us reduce the size of problem from  $(N \cdot K) \times (N \cdot K)$  to a  $2 \times 2$  matrix, focusing solely on a bound state of  $\nu = 1$  channel, and the first resonance of  $\nu = 0$  channel:

$$\begin{pmatrix} E_{\text{BS}} + \hbar\omega & \frac{\alpha}{2} (\psi_{\text{BS}}^\theta | V' | \psi_{\text{R1}}^\theta) \\ \frac{\alpha}{2} (\psi_{\text{R1}}^\theta | V' | \psi_{\text{BS}}^\theta) & E_{\text{R1}} \end{pmatrix}. \quad (119)$$

The value of integrals in a C-formalism (let us denote them  $\mathcal{D}$  from now on) does not depend on the parameter  $\theta$  in fact . To be able to construct such matrix, one has to already have calculated the non-interacting system in terms of the complex-scaled Floquet theory, obtaining the values of both energies along with both of the wave-functions  $\psi_{\text{BS}}^\theta$  (bound state) and  $\psi_{\text{R1}}^\theta$  (the first resonance).

The non-Hermitian  $2 \times 2$  matrix can be in principle decomposed into a form of

$$A \begin{pmatrix} 1 & 0 \\ 0 & 1 \end{pmatrix} + B \begin{pmatrix} -1 & \lambda \\ \lambda & +1 \end{pmatrix}, \quad (120)$$

where the coefficients  $A$  and  $B$  can be shown to equal:

$$A = E_{\text{BS}} + \hbar\omega + \frac{\alpha\mathcal{D}}{2\lambda}, \quad (121)$$

$$B = E_{\text{R1}} - E_{\text{BS}} - \hbar\omega - \frac{\alpha\mathcal{D}}{2\lambda}. \quad (122)$$

Since the first matrix represents just a shift on a diagonal, our problem reduces to finding the eigenvalue degeneracy condition for the second matrix alone. That is

$$\begin{vmatrix} -1 - E & \lambda \\ \lambda & 1 - E \end{vmatrix} = (-1 - E)(1 - E) - \lambda^2 = 0 \quad (123)$$

$$E^2 = \lambda^2 + 1 \quad (124)$$

$$E = \pm \sqrt{\lambda^2 + 1} . \quad (125)$$

The eigenvectors can be found by solving:

$$\begin{pmatrix} -1 \mp \sqrt{\lambda^2 + 1} & \lambda \\ \lambda & 1 \mp \sqrt{\lambda^2 + 1} \end{pmatrix} \begin{pmatrix} c_1^\pm \\ c_2^\pm \end{pmatrix} \equiv 0 . \quad (126)$$

By fixing coefficient  $c_1^\pm$  to one, the solution reads:

$$\vec{c}^\pm = \begin{pmatrix} 1 \\ \frac{-\lambda}{1 \mp \sqrt{\lambda^2 + 1}} \end{pmatrix} . \quad (127)$$

In order to be double degenerate, the eigenvalue  $E$  needs to be zero. Hence, the parameter lambda equals  $\pm i$ :

$$\lambda = \pm i \quad (128)$$

We can now express the eigenvalue degeneracy condition for the only two free parameters  $\alpha_0$  and  $\omega$ :

$$\alpha_0 = \pm \frac{\Gamma}{\text{Re } \mathcal{D}} , \quad (129)$$

$$\omega = \frac{\mathcal{E}_R - \Gamma \frac{\text{Im } \mathcal{D}}{\text{Re } \mathcal{D}}}{\hbar} . \quad (130)$$

By plugging these relations into the expression for coefficients  $A$  and  $B$ , we obtain:

$$A = \mathcal{E}_R - \frac{\Gamma}{4} \frac{\text{Im } \mathcal{D}}{\text{Re } \mathcal{D}} - i \frac{\Gamma}{4} , \quad (131)$$

$$B = \frac{\Gamma}{4} \frac{\text{Im } \mathcal{D}}{\text{Re } \mathcal{D}} - i \frac{\Gamma}{4} . \quad (132)$$

Besides, when the eigenvalues are double degenerate, we can see from eq. (127) that both vectors become identical:

$$\vec{c}^+ = \vec{c}^- = \begin{pmatrix} 1 \\ \frac{\mp i}{1 \mp \sqrt{(\pm i)^2 + 1}} \end{pmatrix} = \begin{pmatrix} 1 \\ \mp i \end{pmatrix} \equiv \vec{c}_{(\mp)} . \quad (133)$$

It is important to point out that the sign  $\mp$  is related to the value of  $\lambda = \pm i$  solely. That is to the solution of two different—yet related—matrices. These eigenvectors will be denoted with  $(\mp)$  in the lower index. The eigenvectors have the so-called selforthogonality property. That is, that their  $\mathbb{C}$ -norm equals zero:

$$(\vec{c}_{(\mp)})^T \vec{c}_{(\mp)} = \begin{pmatrix} 1 & \mp i \end{pmatrix} \begin{pmatrix} 1 \\ \mp i \end{pmatrix} = 1 - 1 = 0 . \quad (134)$$

As a result of this strange behaviour, this category of matrices is called *defective*. Besides, by combining the matrix with  $+\lambda$  and the eigenvector pertinent to the matrix with  $-\lambda$ , the following relation stems out:

$$h(+\lambda) \vec{c}_{(+)}^\pm = f \cdot \vec{c}_{(-)}^\pm \quad (135)$$

$$\begin{pmatrix} -1 & +\lambda \\ +\lambda & 1 \end{pmatrix} \begin{pmatrix} 1 \\ \frac{-(-\lambda)}{1 \mp \sqrt{\lambda^2 + 1}} \end{pmatrix} = - \left( 2 \pm \sqrt{\lambda^2 + 1} \right) \begin{pmatrix} 1 \\ \frac{-(+\lambda)}{1 \mp \sqrt{\lambda^2 + 1}} \end{pmatrix} . \quad (136)$$

So for  $\lambda = \pm i$  we get  $f = -2$ . Relation (136) leads to another odd property. To formulate the closure property for the degenerate case  $\lambda = \pm i$ , one has to use exactly these cross-combined terms

$$1 = |\vec{c}_{(+)}| |\vec{c}_{(-)}| + |\vec{c}_{(-)}| |\vec{c}_{(+)}| \quad (137)$$

$$= \begin{pmatrix} 1 \\ i \end{pmatrix} (1 \quad -i) + \begin{pmatrix} 1 \\ -i \end{pmatrix} (1 \quad i) = \begin{pmatrix} 1 & -i \\ i & 1 \end{pmatrix} + \begin{pmatrix} 1 & -i \\ i & 1 \end{pmatrix} = 1 . \quad (138)$$

The last interesting phenomenon worth of mentioning is called the *state exchange phenomenon*. By stroboscopic encircling of the  $\lambda = \pm 1$  points plotted in the complex plane—these points are also called the *exceptional points*—an transition from  $\vec{c}^+$  to  $\vec{c}^-$  occurs, even though the eigenenergy remains the same. For clarification please see the subsubsection 5.2.3 of results where this phenomenon is thoroughly scrutinised and presented on various combinations of parameters.

### 3 Computational Algorithms

#### 3.1 Basis Set Expansion

The expansion of an unknown wavefunction into a linear combination of a fixed complete basis set is a frequently used method throughout physics and computational chemistry. The differential equation then translates into a eigenvalue problem of  $N \times N$  matrix and the wavefunction we are after can be expressed as a vector in the provided basis.

Let us assume a general 1D Schrödinger equation:

$$\left( -\frac{\hbar^2}{2m} \nabla_x^2 + V(x) \right) \psi(x) = E \psi(x), \quad (139)$$

and a complete basis set:

$$\{b_\nu(x)\}_{\nu=1}^N . \quad (140)$$

The wavefunction  $\psi(x)$  can be than expressed as a linear combination:

$$\psi(x) = \sum_{\nu=1}^N c_\nu b_\nu(x) \quad (141)$$

By restricting ourselves to an orthonormal basis set specifically<sup>3</sup>, the SE can be now expressed as:

$$\sum_{\nu'=1}^N \underbrace{\int_{-\infty}^{\infty} dx b_{\nu}^* \left( -\frac{\hbar^2}{2m} \nabla_x^2 + V(x) \right) b_{\nu'}(x) c_{\nu'}}_{H_{\nu\nu'}} = E c_{\nu} \quad (142)$$

$$\sum_{\nu'=1}^N H_{\nu\nu'} c_{\nu'} = E c_{\nu} \quad (143)$$

$$H\vec{c} = E\vec{c} \quad (144)$$

$$(H - E\mathbb{1})\vec{c} = 0 \quad (145)$$

The eigenvalues and corresponding eigenstates then represent the bound states. The obtained results don't depend on the selected basis set if the basis set is of infinite size. What doesn't happen quite often. Otherwise, since basis set of a finite size must be used, the results are then affected by both its selection and its size. In general, the better and more suitable basis set is adopted, the smaller in size it needs to be to give the same numerical result.

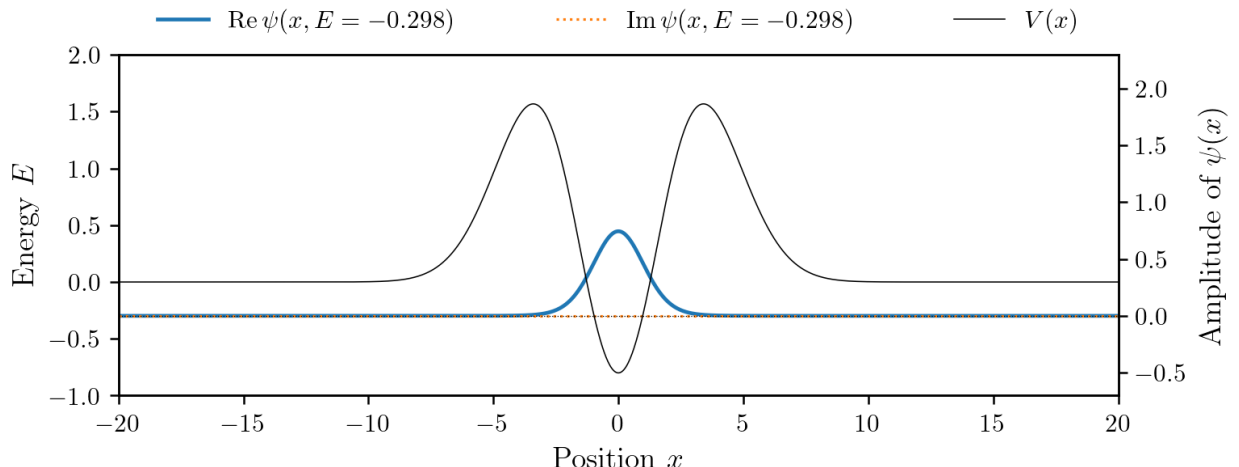


**Figure 4:** Plot of the only present bound state for the exemplary case of depicted potential  $V(x)$  calculated by the standard basis set expansion method. The basis set consisted of first 200 infinite square well eigenstates. Width of the well corresponded to the depicted interval.

## 4 Implementation Details

All computations were performed using the Python programming language. The noteworthy libraries having been used were the NumPy (CPU implementation) and CuPy (GPU implementation) libraries for numerical operations, Matplotlib and Mayavi for plotting and data visualization, and joblib for computation parallelization. Some 3D plots were further optimised in a desktop application Meshlab.

The implementation was optimised for the speed, at the little cost of memory. The propagator in (30) was vectorized in the dimension of energies  $E$  which were obviously also discretized.

$$\bar{\psi}_{n+1}(\vec{E}) + \bar{\psi}_{n-1}(\vec{E}) = 2 \cdot \left( 1 - \frac{m(\Delta x)^2}{\hbar^2} \cdot (\vec{E} - V_n) \right) \bar{\psi}_n(\vec{E}) \quad (146)$$

---

<sup>3</sup>that is  $\int_{-\infty}^{\infty} dx b_{\nu}^* b_{\nu'} = \delta_{\nu\nu'}$

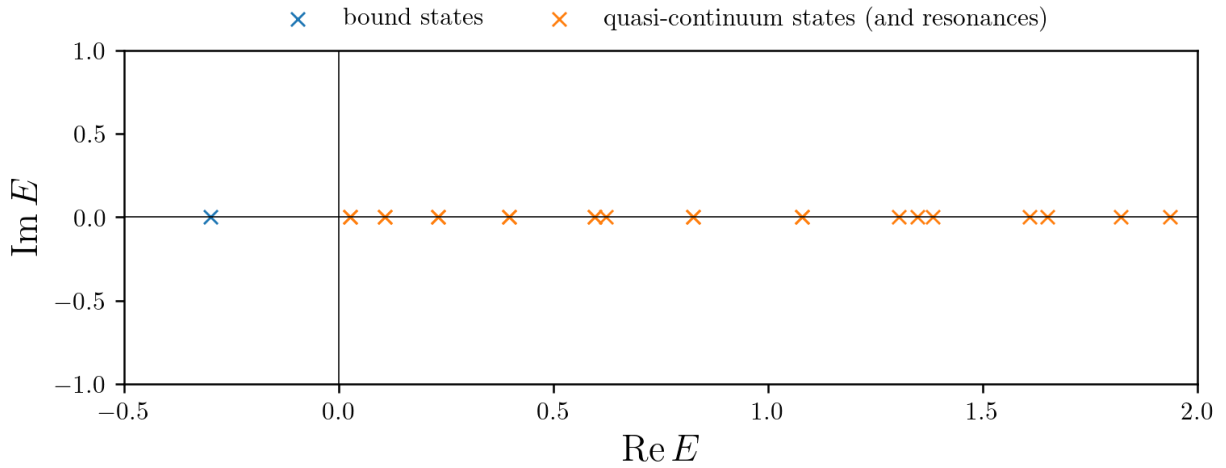


**Figure 5:** Eigenvalues obtained by the basis set expansion method plotted on a complex plane. As can be seen, there is only one bound state with a negative value of energy. Other, positive values corresponds to the so-called quasi-continuum states between those are hidden also the resonances (metastable states).

Even though this algorithm provided rather short computation times<sup>4</sup>, the amount of data related to the wavefunctions was unbearable for my RAM (cca 70 Gb in size) and needed to be stored on disk. As a result, the subsequent analysis of the data took more time than the calculation itself. That is, the code isn't optimised that well towards the data analysis and definitely would need a revision.

The code is stored on GitHub under this link: <https://github.com/MichalPt/resonances>

---

<sup>4</sup>for example, calculation with 10 000 steps in the coordinate and 400 000 steps in the energy took on my 5 year old laptop less than 2 minutes

## 5 Results

### 5.1 Scattering on a Potential

### 5.1.1 Standard Hermitian Approach

Transmission coefficient

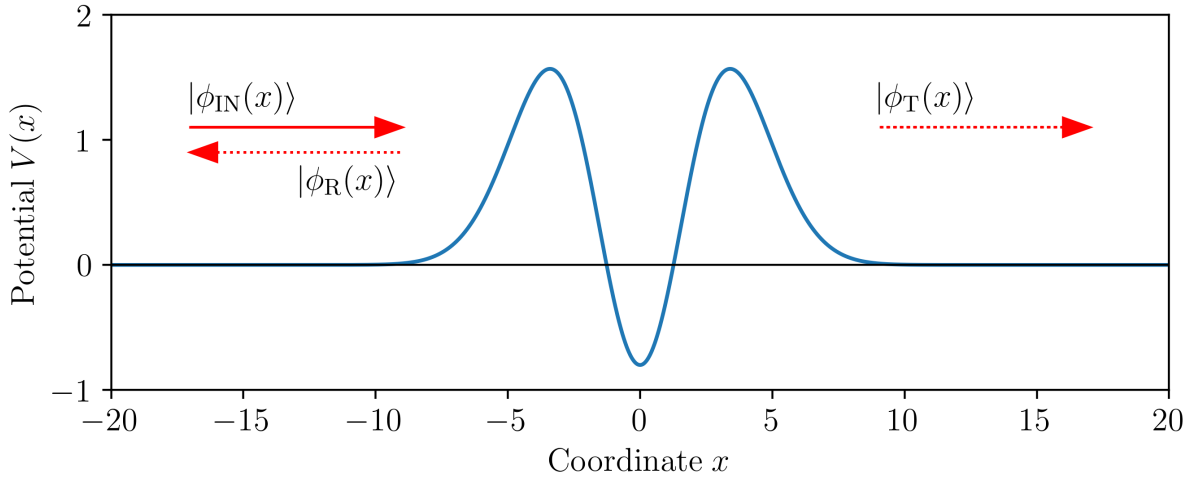


**Figure 6:** Shape of the studied potential. The direction of propagation of the incoming state  $|\phi_{IN}\rangle$ , along with the transmitted ( $|\phi_T\rangle$ ) and reflected ( $|\phi_R\rangle$ ) states, is denoted in the figure as well.

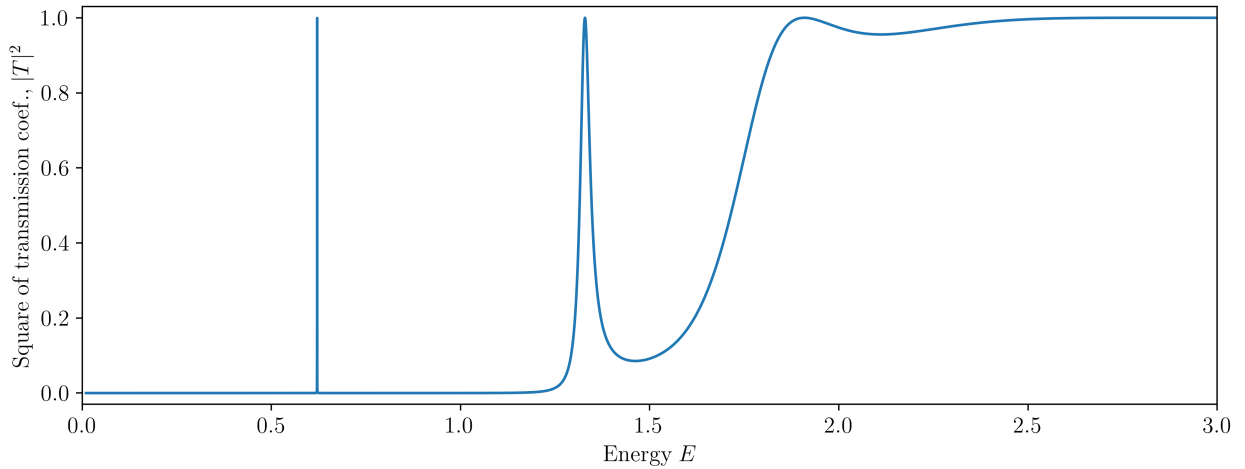


**Figure 7:** Dependence of the absolute value of transmission coefficient squared ( $|T|^2$ ) on the energy  $E$  as calculated by the propagation a grid algorithm.

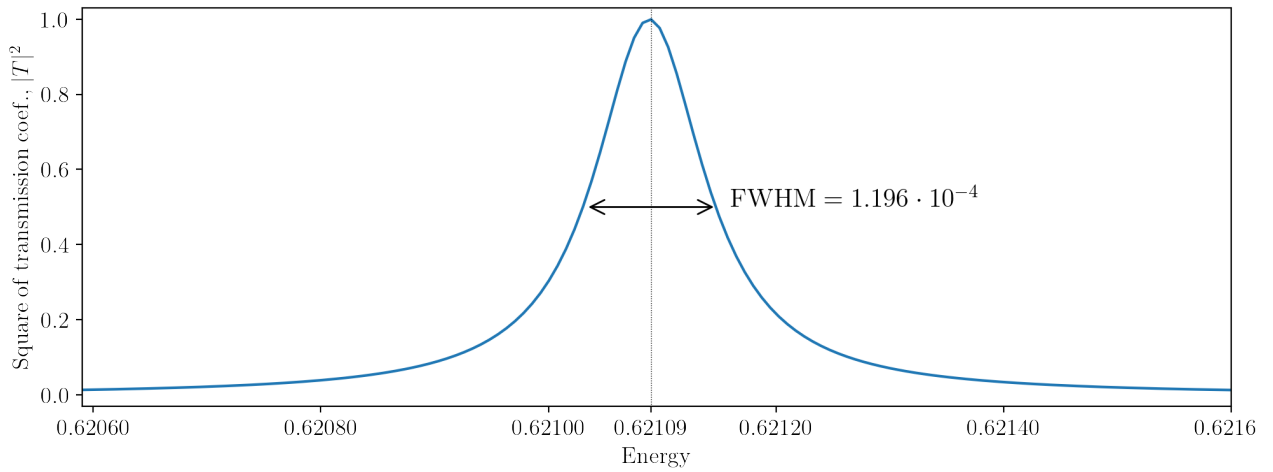


**Figure 8:** Closer look at the first resonance peak and its Lorentzian shape. The full width at half maximum (FWHM) measured from the presented data is denoted in the image.

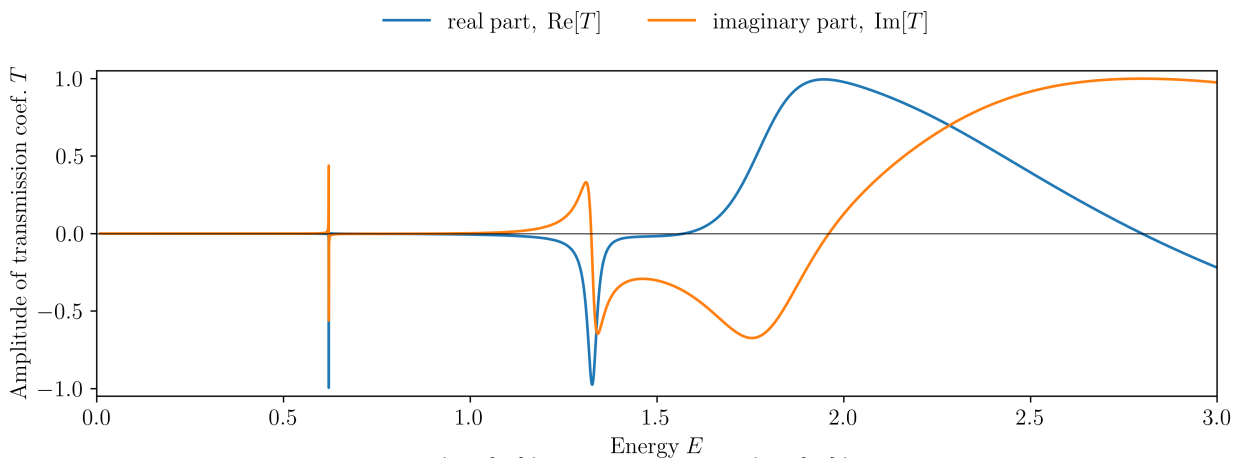


**Figure 9:** Dependence of the real ( $\text{Re}\{T\}$ ) and imaginary ( $\text{Im}\{T\}$ ) part of the transmission coefficient on the values of energy  $E$  as calculated by the propagation a grid algorithm.

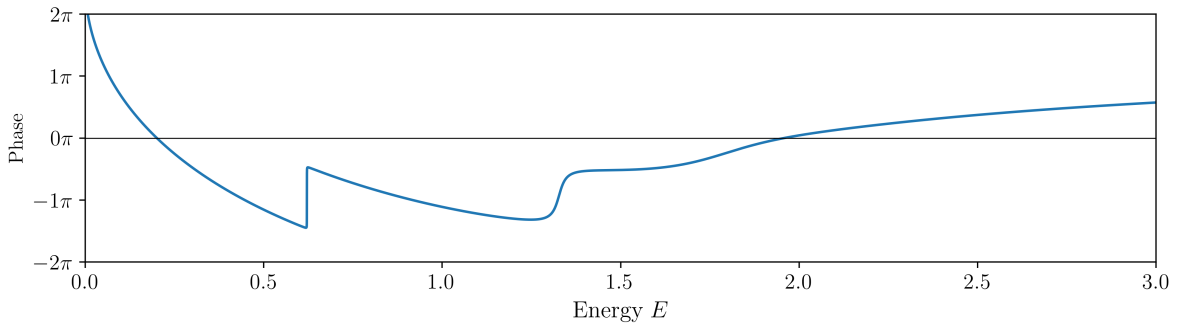


**Figure 10:** Dependence of the phase  $\phi$  of the transmission coefficient  $T$  on energy  $E$  as calculated by the propagation a grid algorithm.

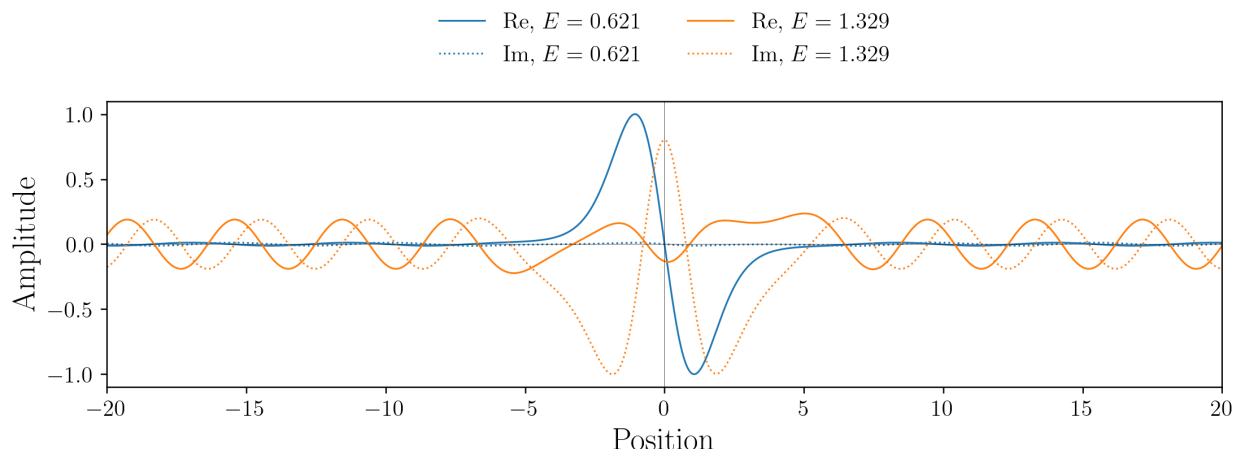


**Figure 11:** Plot of both the real and imaginary parts of two wavefunctions corresponding to the first two resonance peaks observed in the plot of transmission coefficient  $T$ . The data were obtained by the propagation a grid algorithm.

## 2D plots of wavefunctions – real part

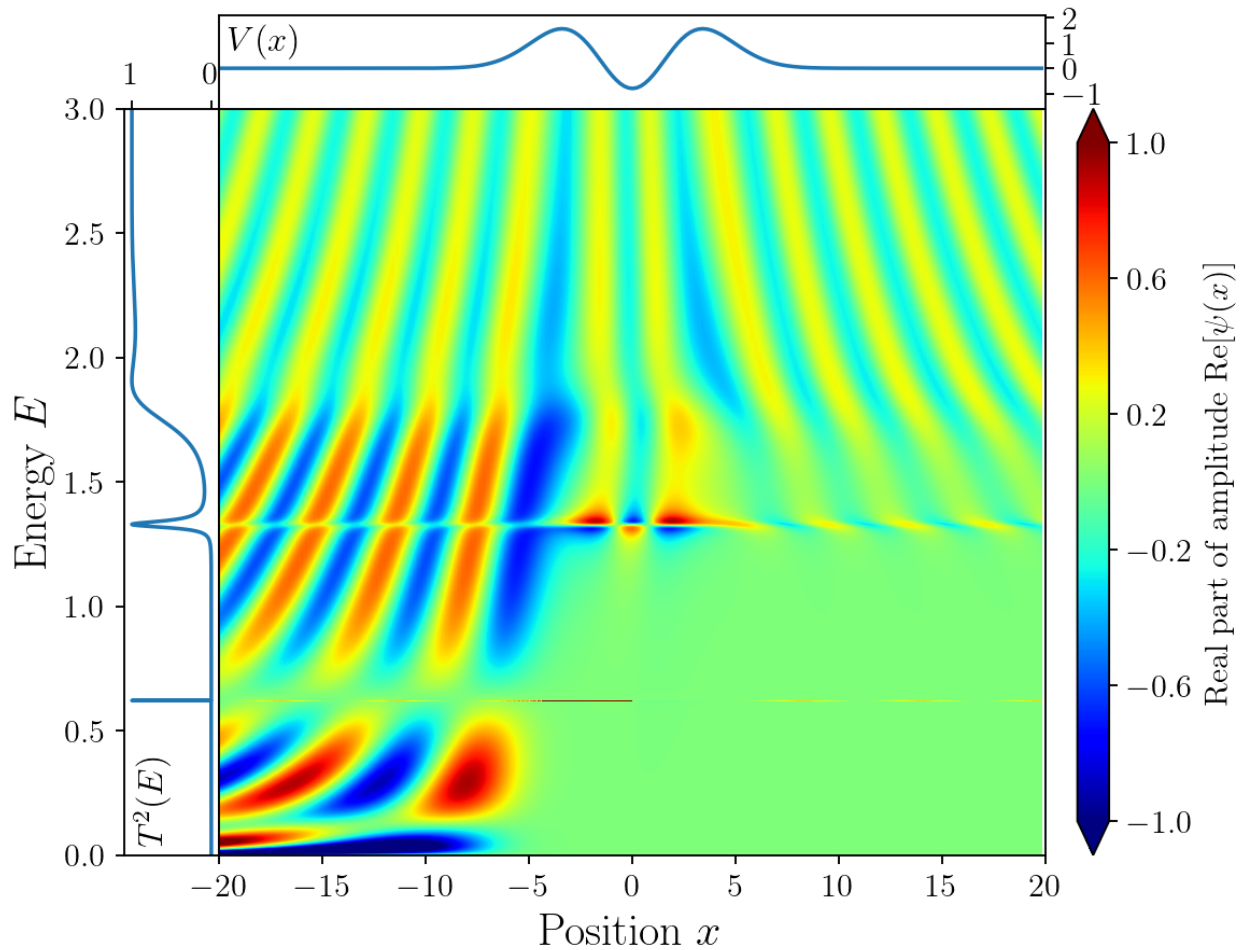


**Figure 12:** Dependence of the *real part* of the normalized scattered wavefunction amplitude on the energy  $E$  and coordinate  $x$ . Two additional plots are appended to the upper and left side of the central plot. They depict the local potential  $V(x)$  and the square of transmission coefficient  $|T(E)|^2$  respectively.

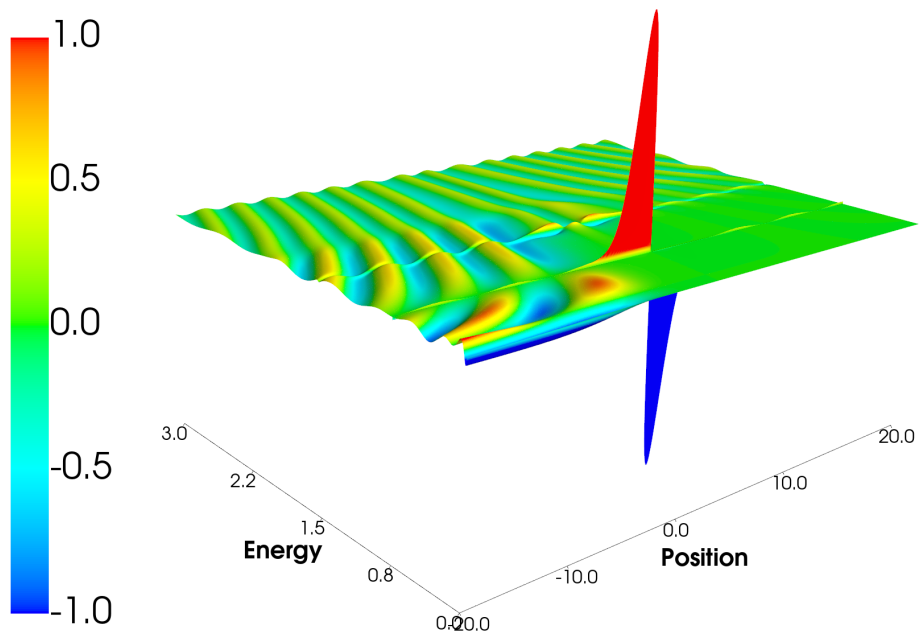


**Figure 13:** Image of a 3D representation of the plot in Figure 12, i.e. a plot of the real part of the wavefunction.

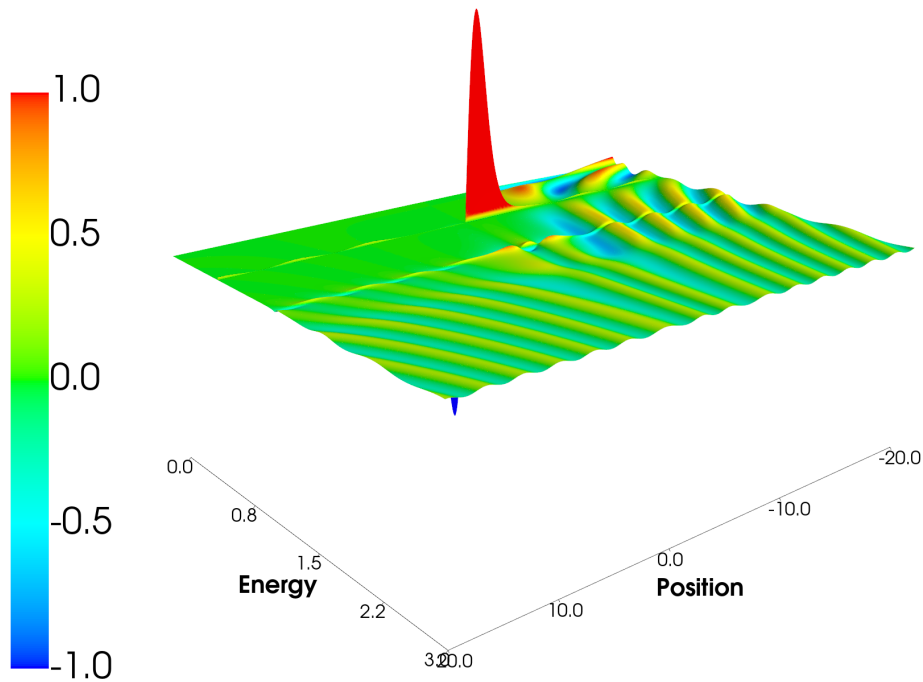


**Figure 14:** Image of a 3D representation of the plot in Figure 12, i.e. a plot of the real part of the wavefunction; opposite point of view.

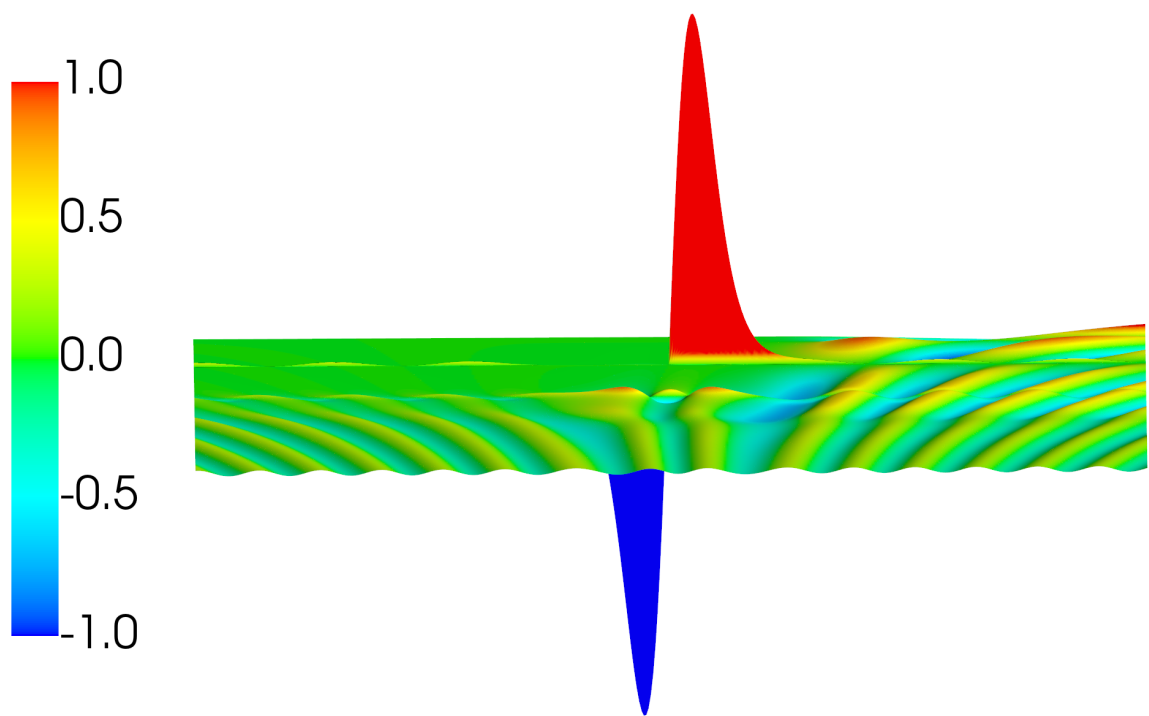


**Figure 15:** Image of a 3D representation of the plot in Figure 12, i.e. a plot of the real part of the wavefunction; the view is perpendicular to the axis of position, parallel to the axis of energy.

## 2D plots of wavefunctions – imaginary part

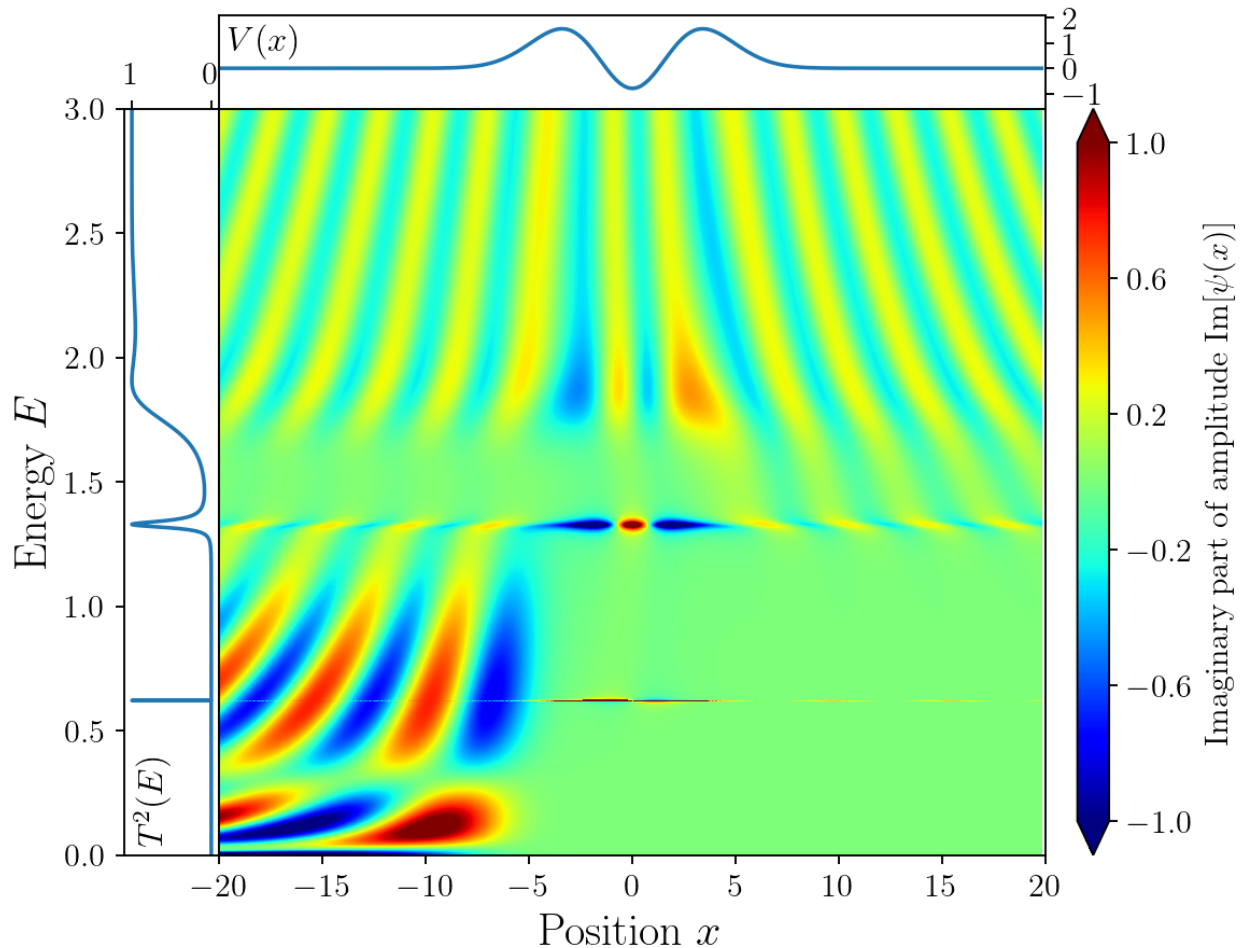


**Figure 16:** Dependence of the *imaginary part* of the normalized scattered wavefunction amplitude on the energy  $E$  and coordinate  $x$ . Two additional plots are appended to the upper and left side of the central plot. They depict the local potential  $V(x)$  and the square of transmission coefficient  $|T(E)|^2$  respectively.

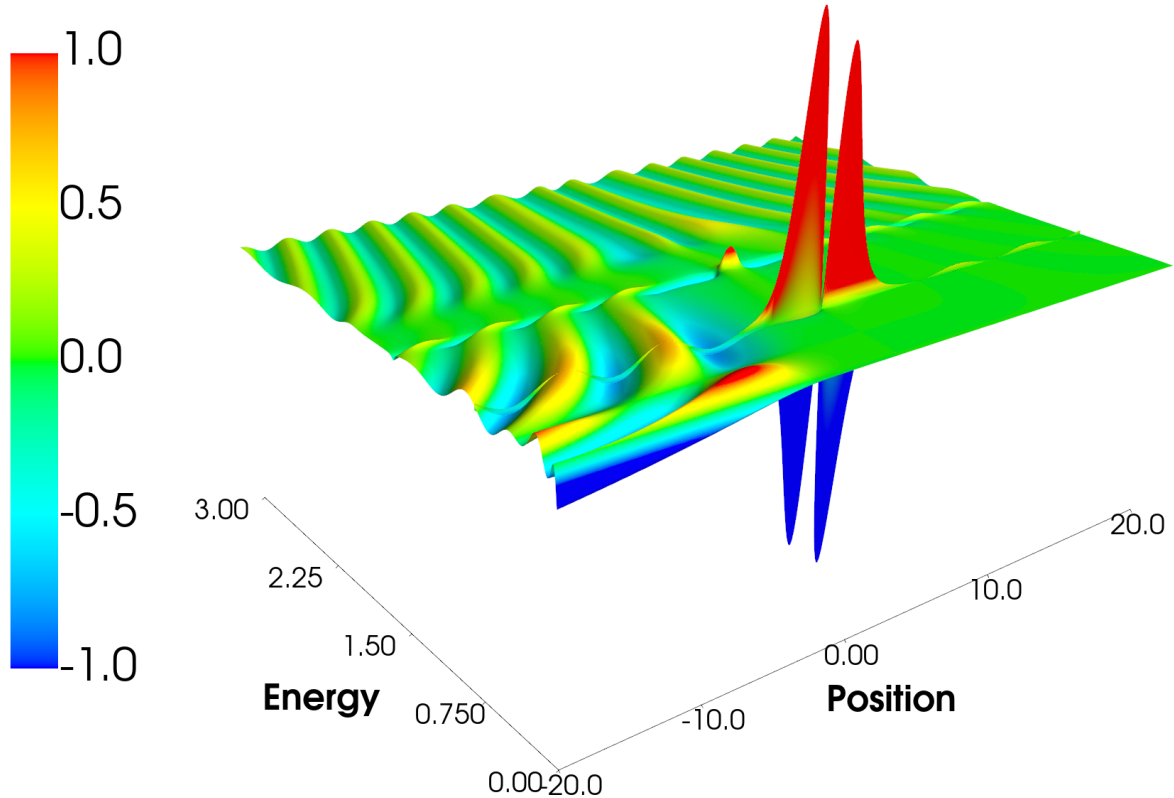


**Figure 17:** Image of a 3D representation of the plot in Figure 16, i.e. a plot of the imaginary part of the wavefunction.

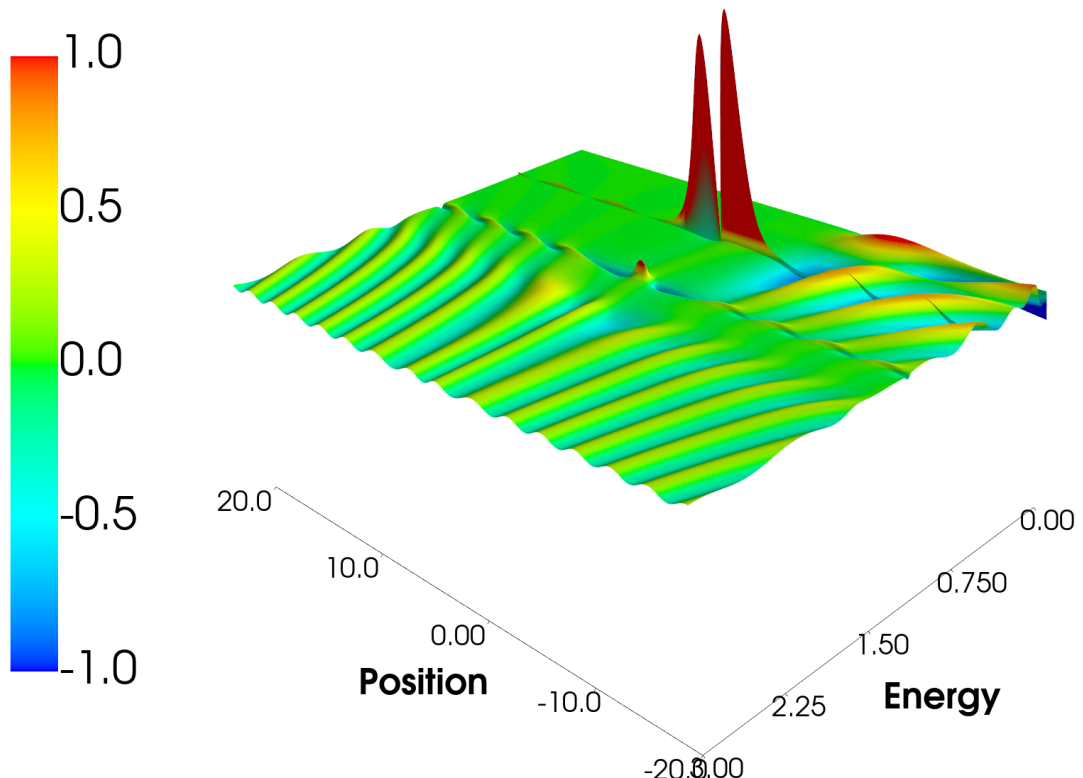


**Figure 18:** Image of a 3D representation of the plot in Figure 16, i.e. a plot of the imaginary part of the wavefunction; rotated direction of view.

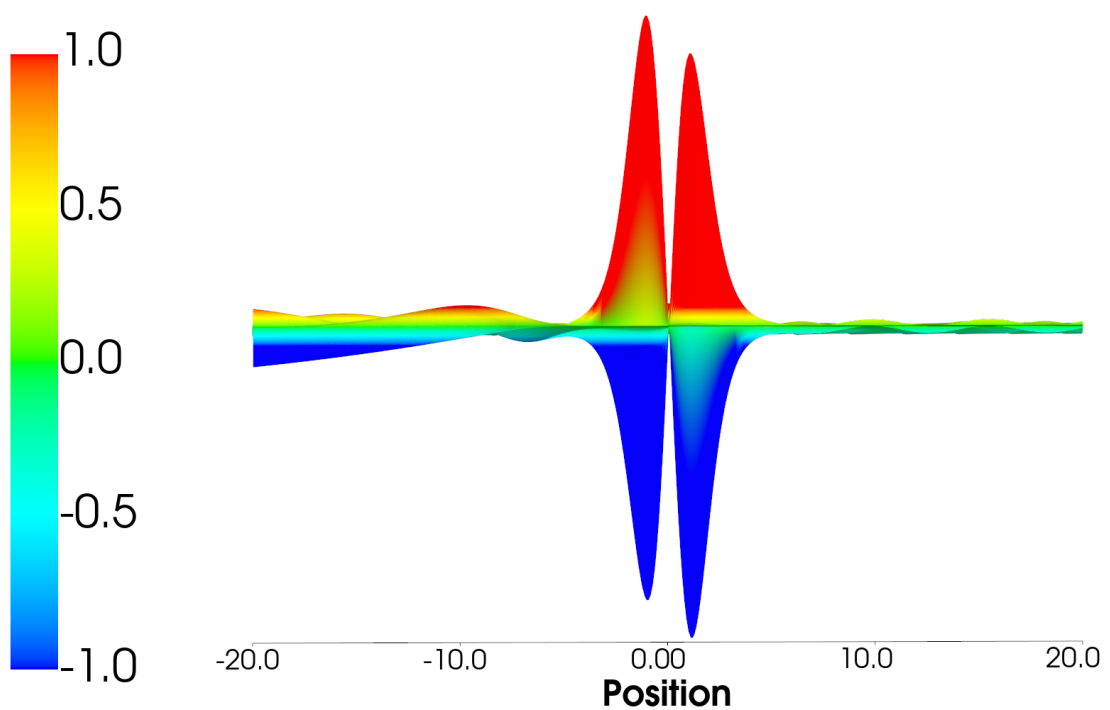


**Figure 19:** Image of a 3D representation of the plot in Figure 16, i.e. a plot of the imaginary part of the wavefunction; the view is oriented perpendicular to the axis of position, parallel to the axis of energy.

**Resonance no. 1 – real part**

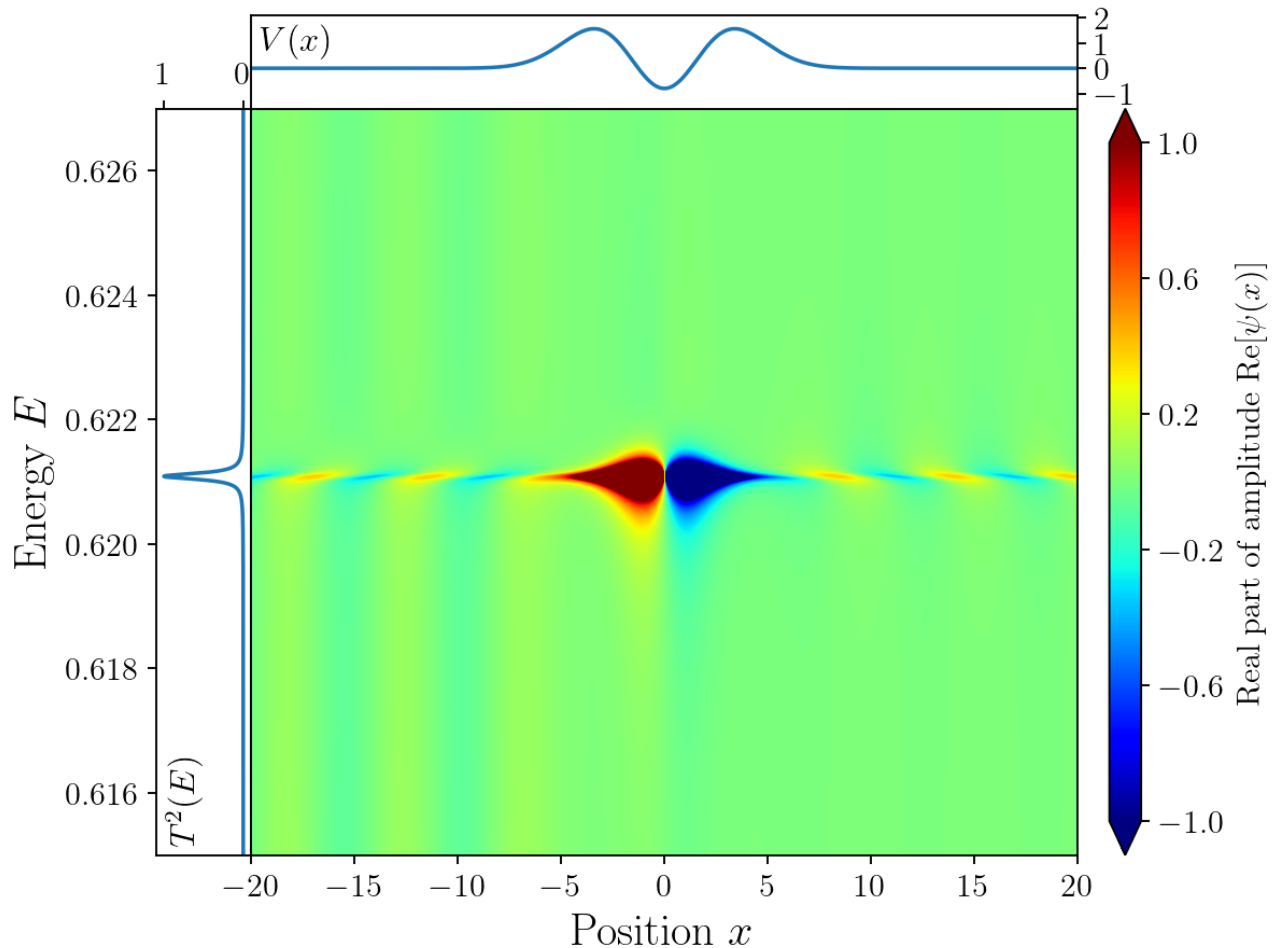


**Figure 20:** Focused area of the **first resonance peak** of the *real part* of the normalized scattered wavefunction. Two additional plots are appended to the upper and left side of the central plot. They depict the local potential  $V(x)$  and the square of transmission coefficient  $|T(E)|^2$  respectively.

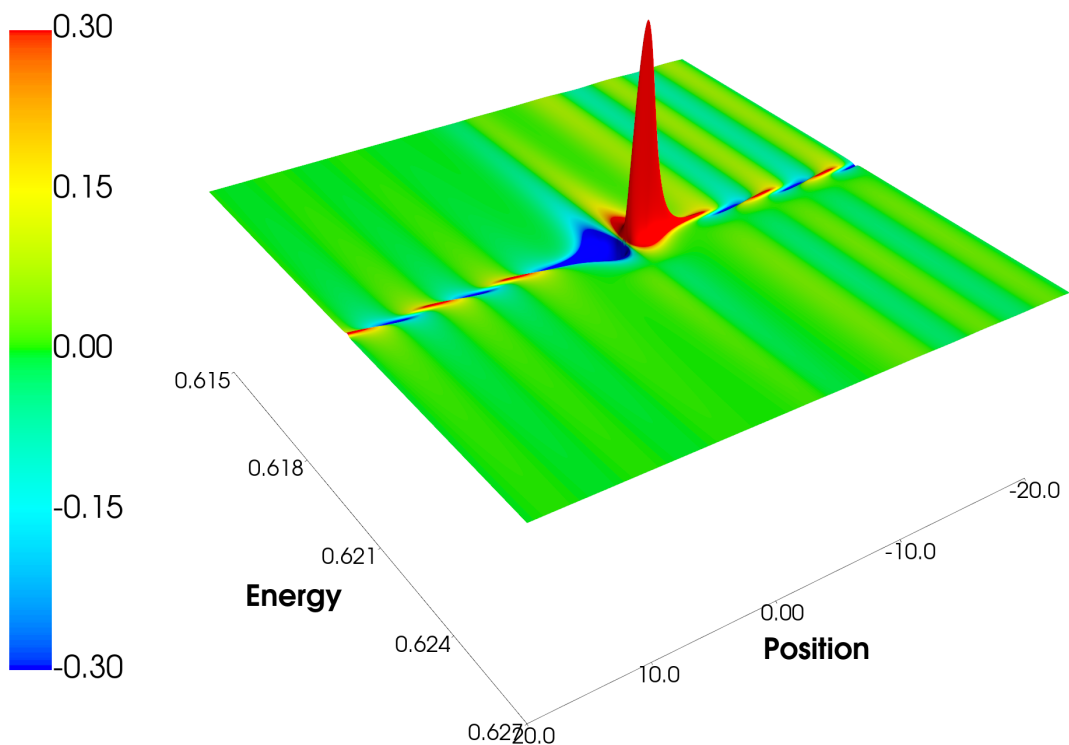


**Figure 21:** Image of a 3D representation of the plot in Figure 20, i.e. a plot of the real part of the wavefunction in the area of the first resonance peak.

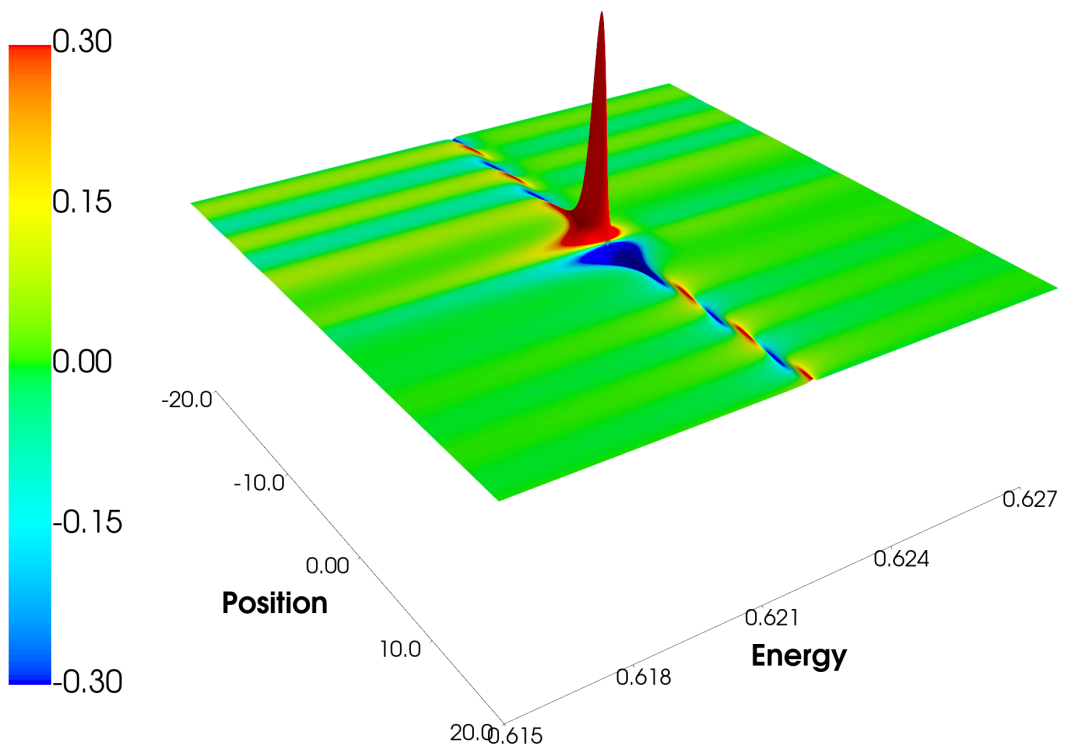


**Figure 22:** Image of a 3D representation of the plot in Figure 20, i.e. a plot of the real part of the wavefunction in the area of the first resonance peak; rotated direction of view.

### Resonance no. 1 – imaginary part

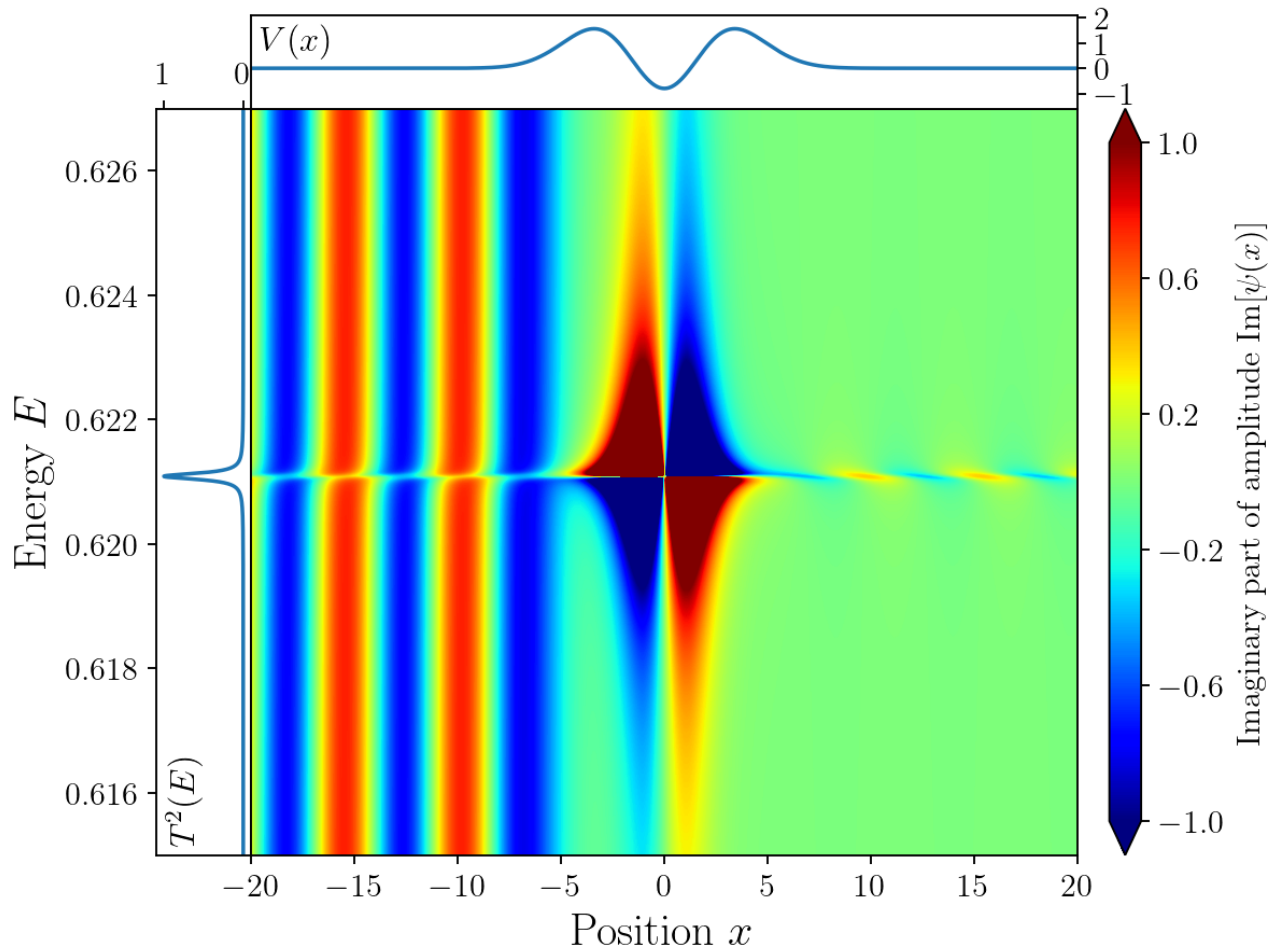


**Figure 23:** Focused area of the **first resonance peak** of the *imaginary part* of the normalized scattered wavefunction. Two additional plots are appended to the upper and left side of the central plot. They depict the local potential  $V(x)$  and the square of transmission coefficient  $|T(E)|^2$  respectively.

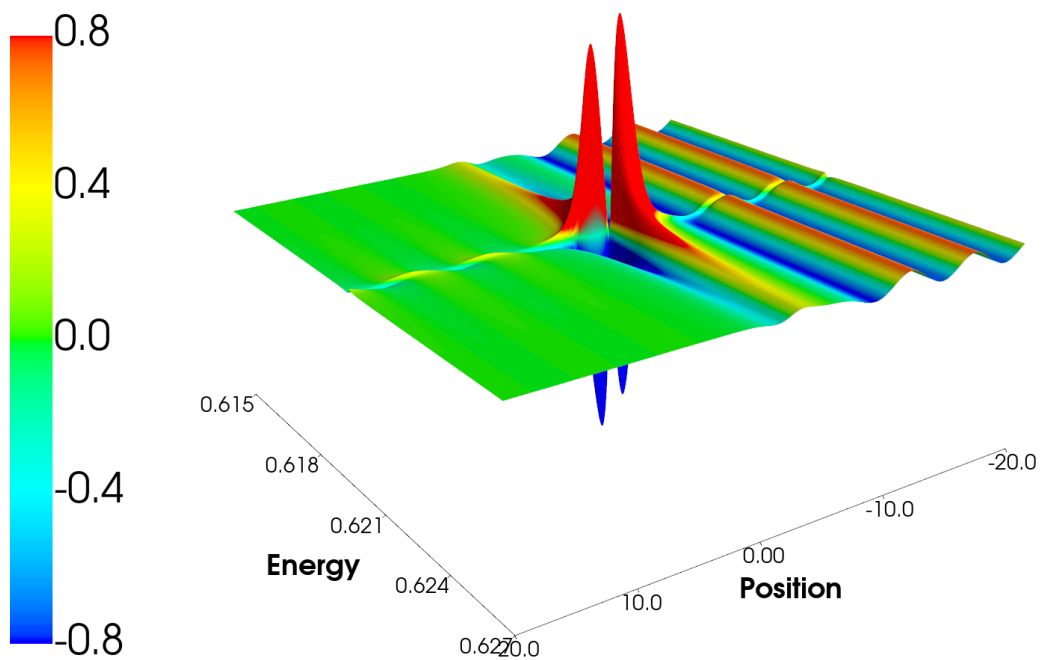


**Figure 24:** Image of a 3D representation of the plot in Figure 23, i.e. a plot of the imaginary part of the wavefunction in the area of the first resonance peak.

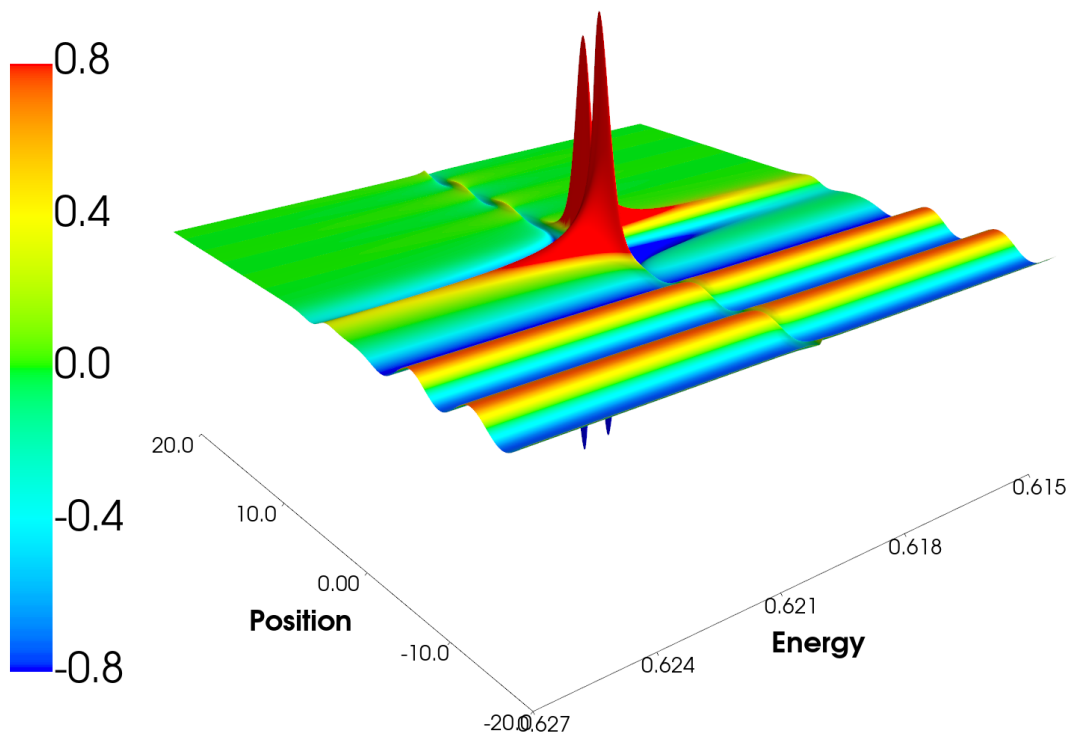


**Figure 25:** Image of a 3D representation of the plot in Figure 23, i.e. a plot of the imaginary part of the wavefunction in the area of the first resonance peak; rotated direction of view

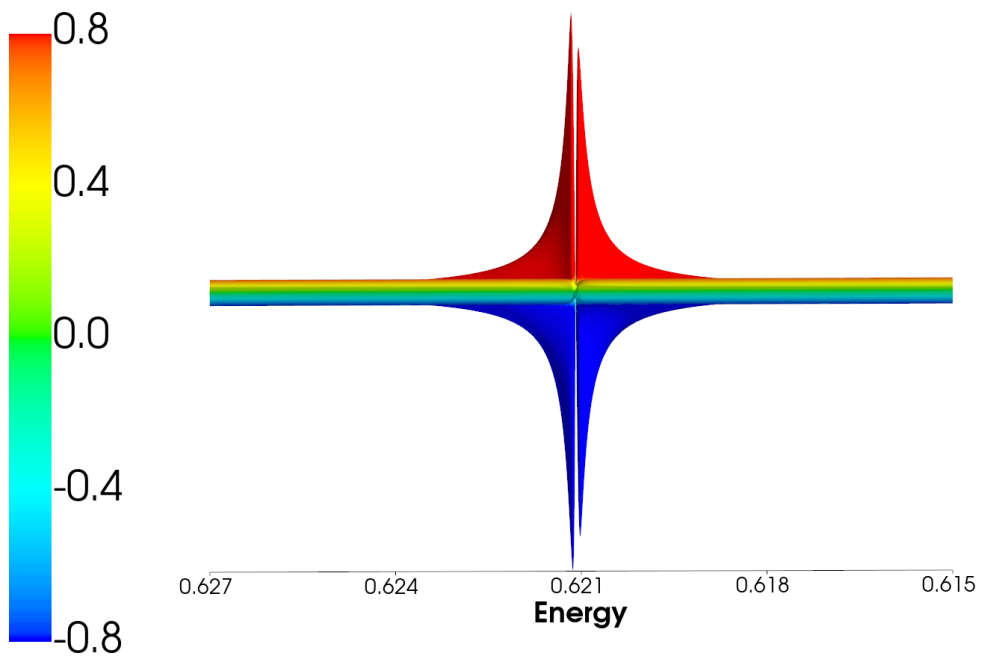


**Figure 26:** Image of a 3D representation of the plot in Figure 23, i.e. a plot of the imaginary part of the wavefunction in the area of the first resonance peak; the view is oriented perpendicular to the axis of energy, parallel to the axis of position.

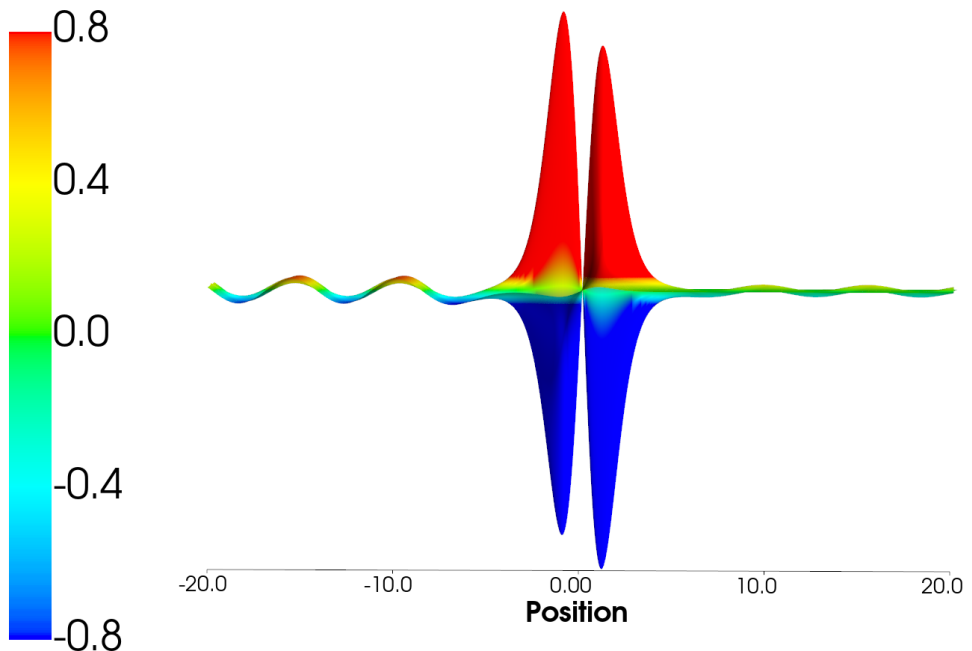


**Figure 27:** Image of a 3D representation of the plot in Figure 23, i.e. a plot of the imaginary part of the wavefunction in the area of the first resonance peak; the view is oriented perpendicular to the axis of position, parallel to the axis of energy.

Resonance no. 2 – real part

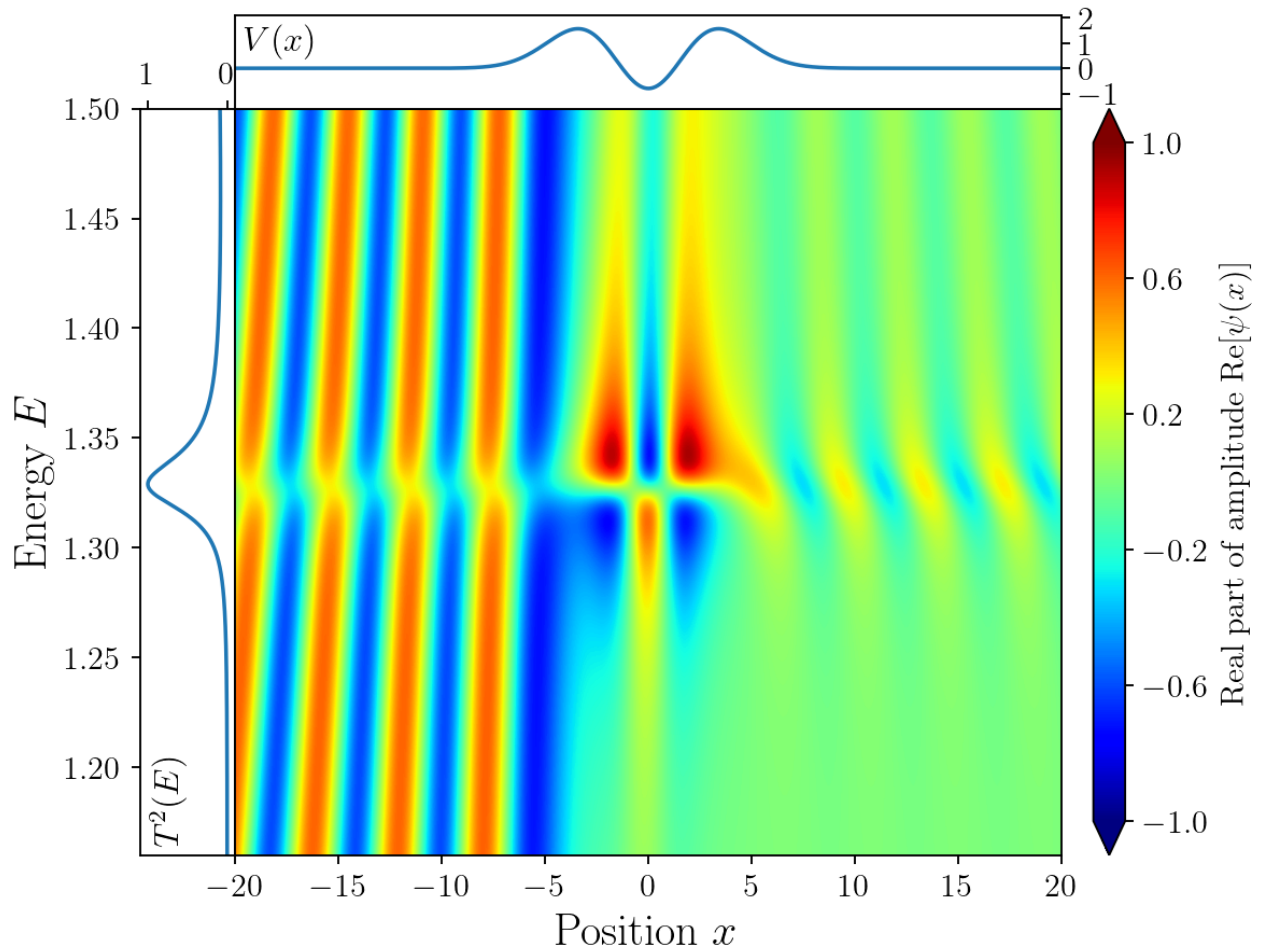


**Figure 28:** Focused area of the **second resonance peak** of the *real part* of the normalized scattered wavefunction. Two additional plots are appended to the upper and left side of the central plot. They depict the local potential  $V(x)$  and the square of transmission coefficient  $|T(E)|^2$  respectively.

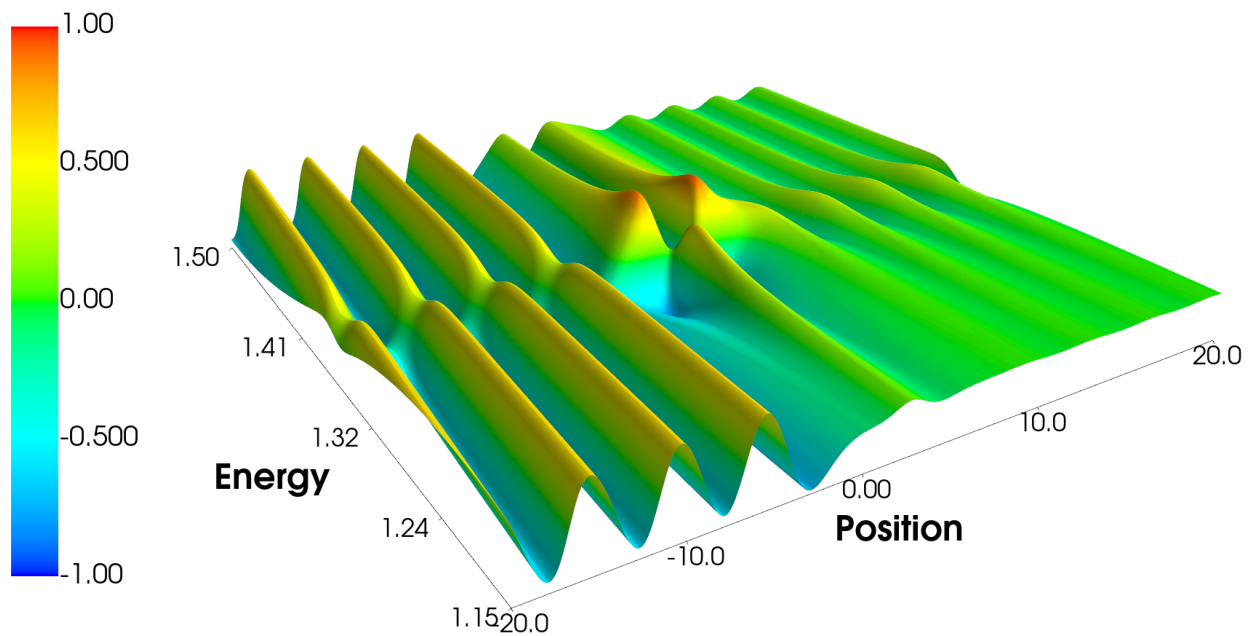


**Figure 29:** Image of a 3D representation of the plot in Figure 28, i.e. a plot of the real part of the wavefunction in the area of the second resonance peak.

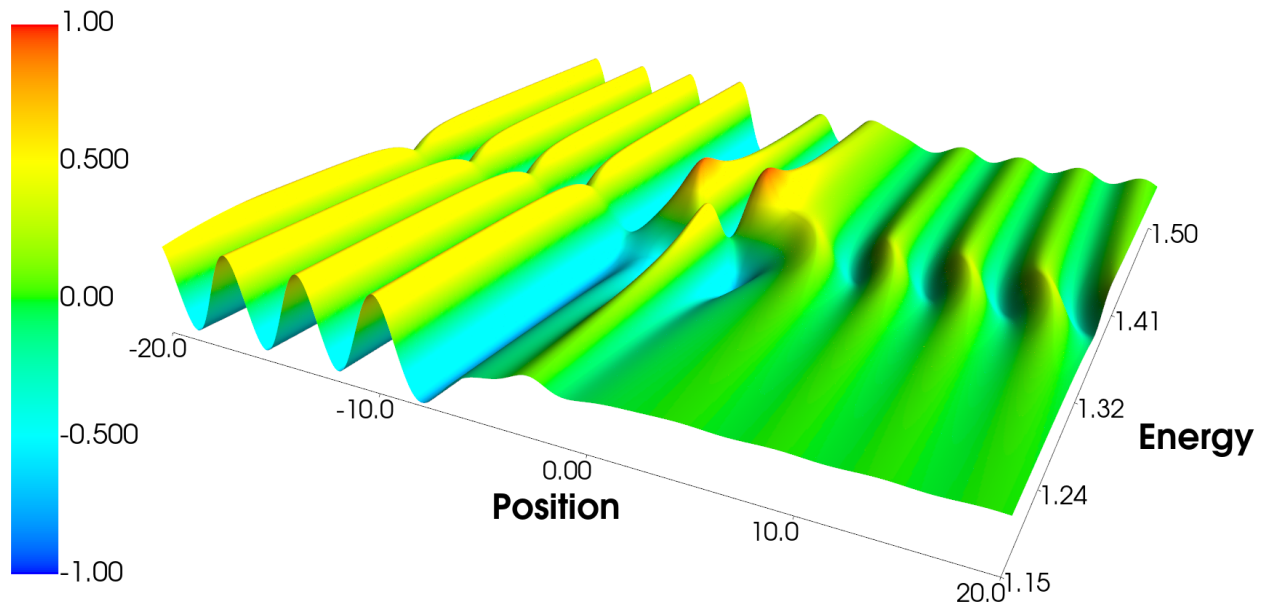


**Figure 30:** Image of a 3D representation of the plot in Figure 28, i.e. a plot of the real part of the wavefunction in the area of the second resonance peak; rotated direction of view.

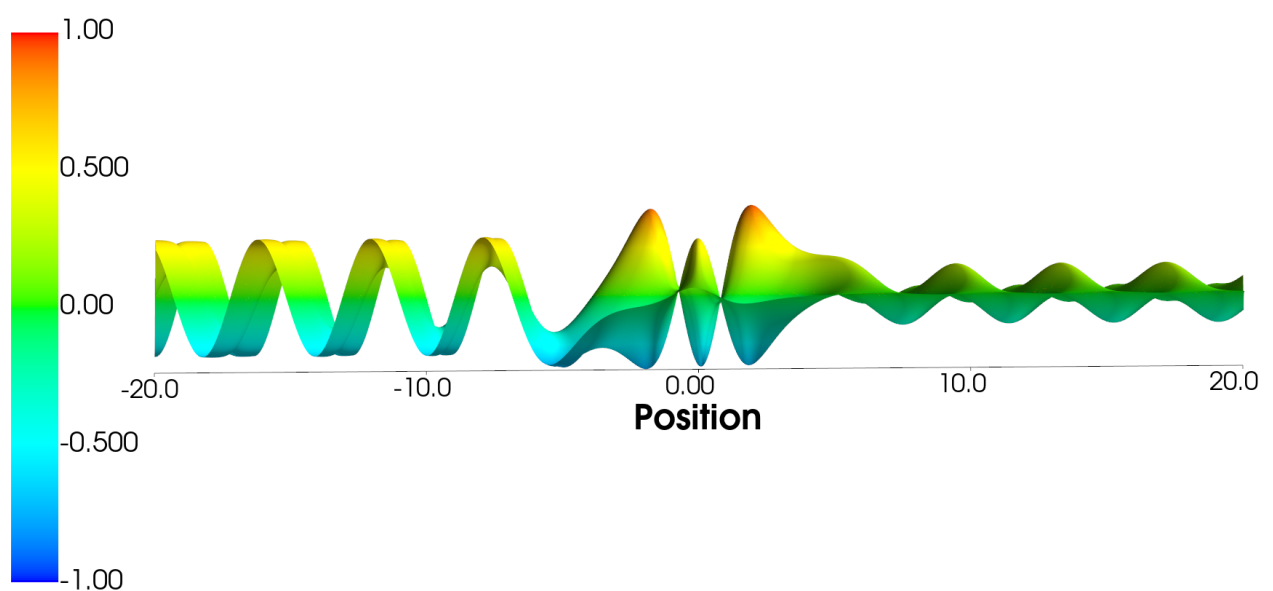


**Figure 31:** Image of a 3D representation of the plot in Figure 28, i.e. a plot of the real part of the wavefunction in the area of the second resonance peak; the view is oriented perpendicular to the axis of position, parallel to the axis of energy.

Resonance no. 2 – imaginary part

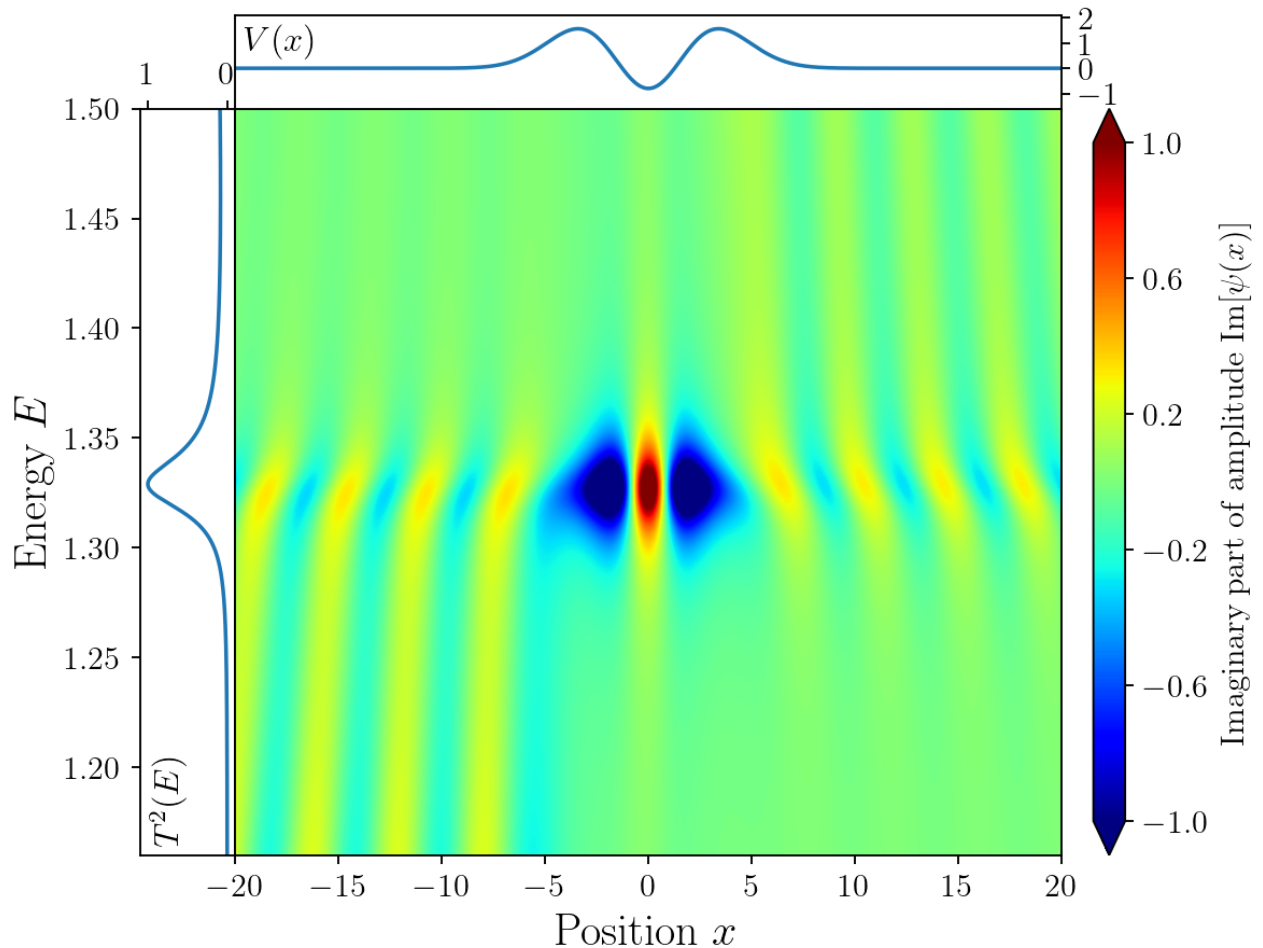


**Figure 32:** Focused area of the **second resonance peak** of the *imaginary part* of the normalized scattered wavefunction. Two additional plots are appended to the upper and left side of the central plot. They depict the local potential  $V(x)$  and the square of transmission coefficient  $|T(E)|^2$  respectively.

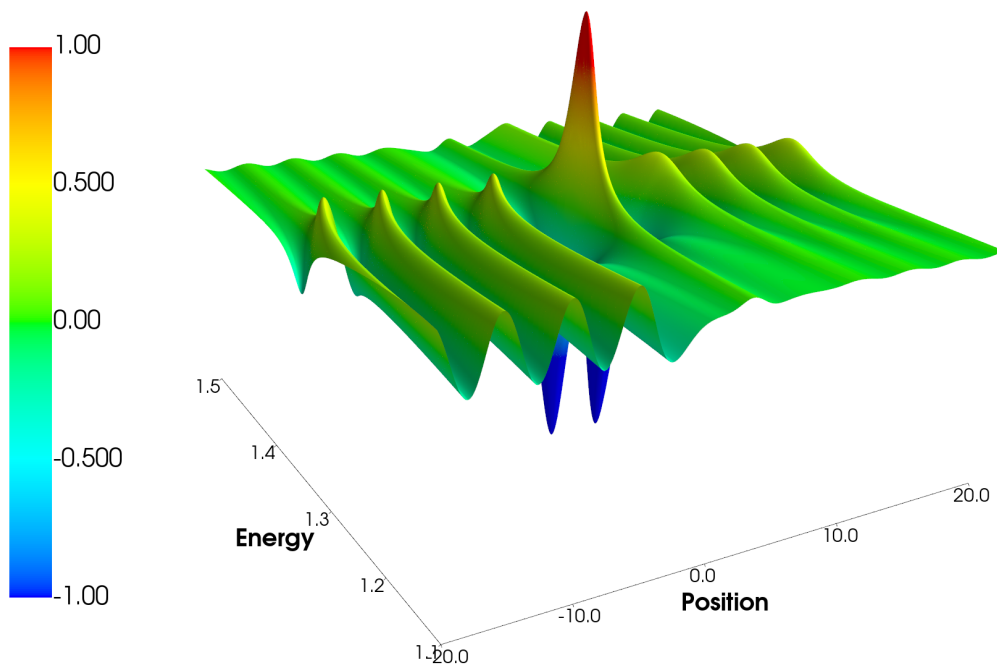


**Figure 33:** Image of a 3D representation of the plot in Figure 32, i.e. a plot of the imaginary part of the wavefunction in the area of the second resonance peak.

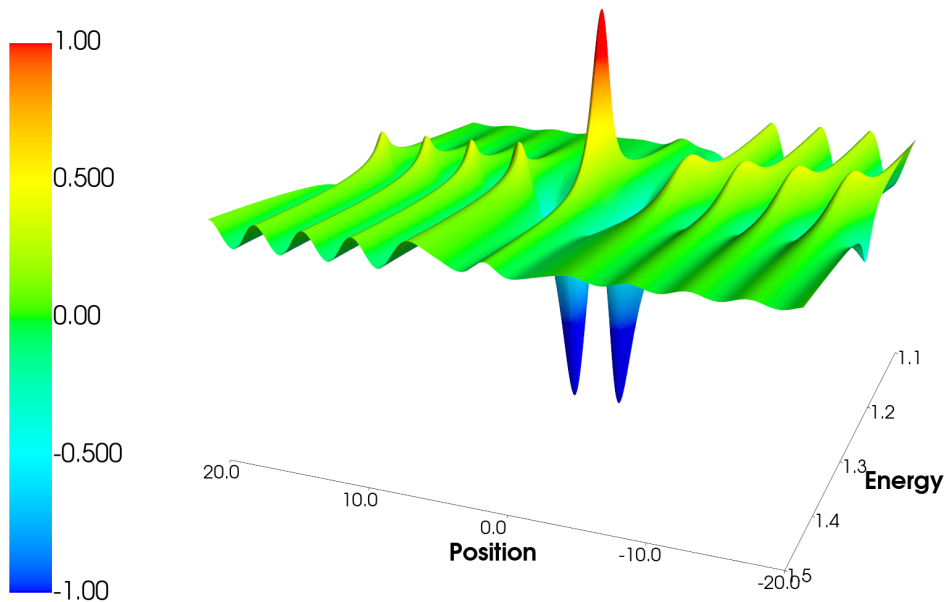


**Figure 34:** Image of a 3D representation of the plot in Figure 32, i.e. a plot of the imaginary part of the wavefunction in the area of the second resonance peak; rotated direction of view.

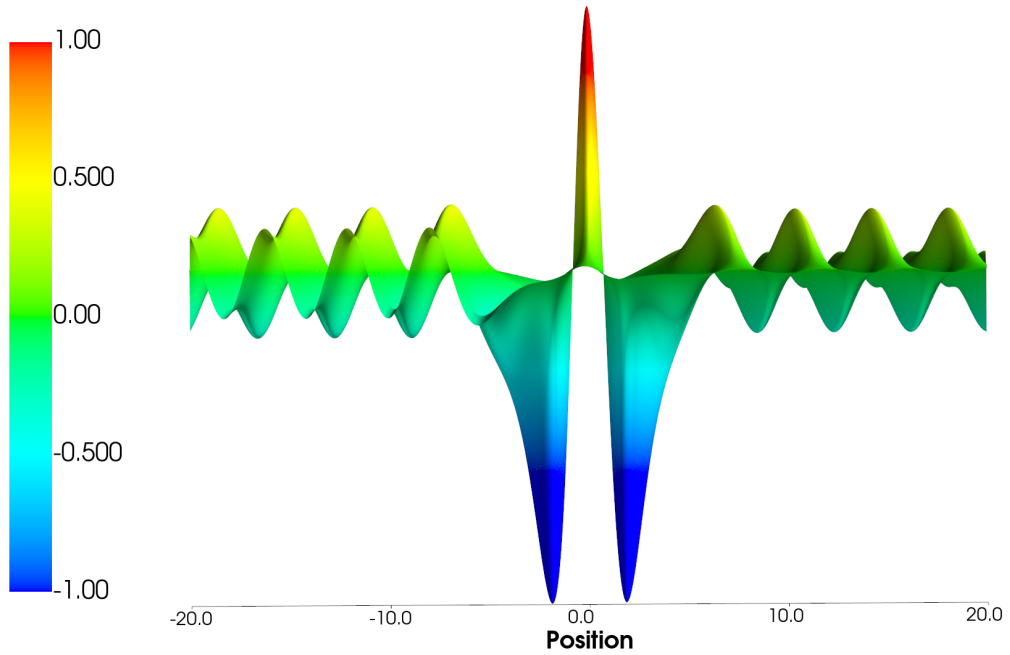


**Figure 35:** Image of a 3D representation of the plot in Figure 32, i.e. a plot of the imaginary part of the wavefunction in the area of the second resonance peak; the view is oriented perpendicular to the axis of position, parallel to the axis of energy.

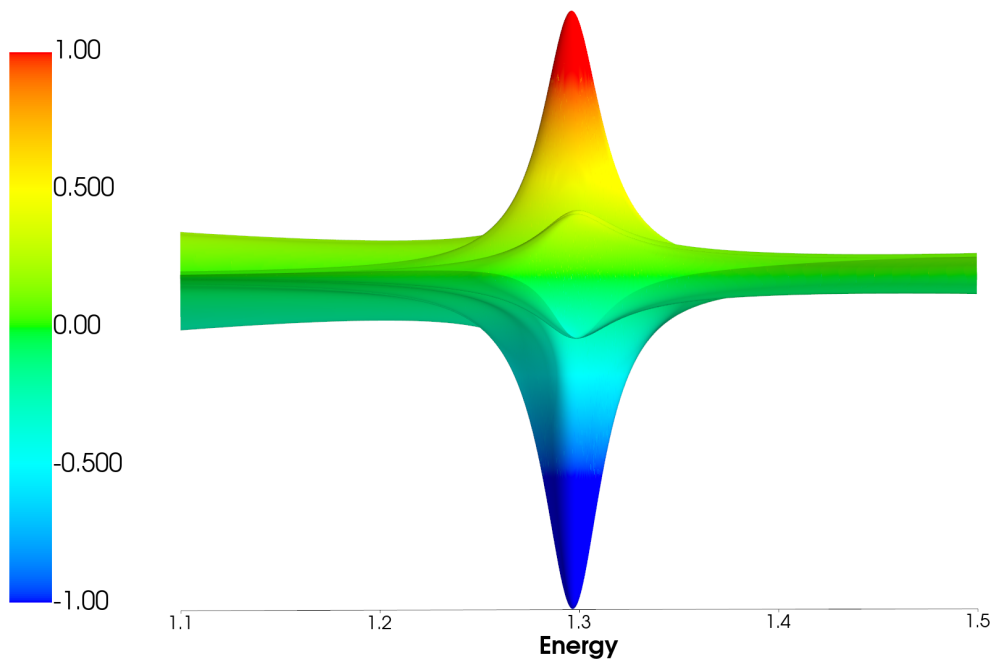


**Figure 36:** Image of a 3D representation of the plot in Figure 32, i.e. a plot of the imaginary part of the wavefunction in the area of the second resonance peak; the view is oriented perpendicular to the axis of energy, parallel to the axis of position.

### 5.1.2 Non-Hermitian Approach

#### Bound State and First Two Resonances

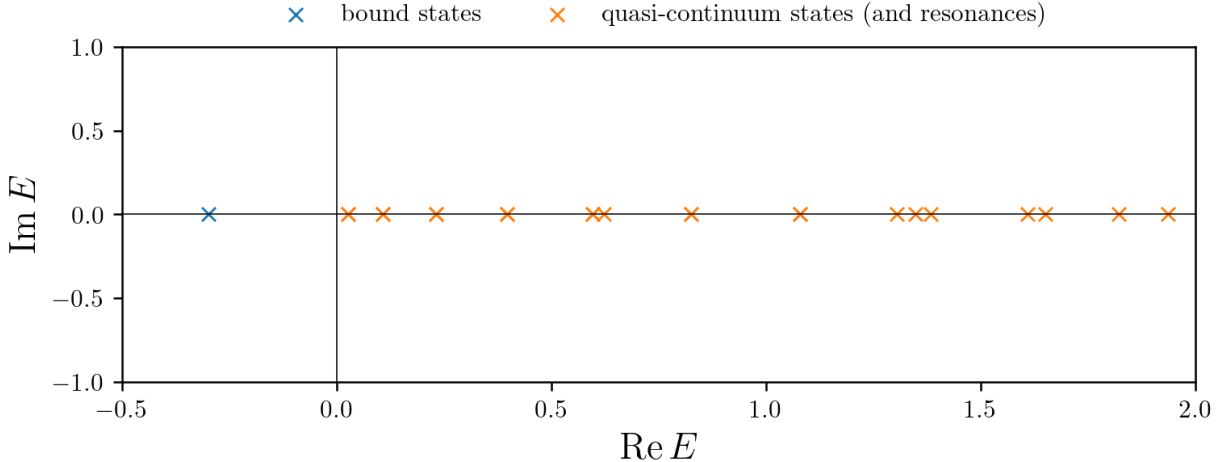


**Figure 37:** Energies of various eigenstates obtained by a basis set expansion using a set of 200 eigenfunctions of an infinite square well potential. Results are plotted in the complex plane. Since complex-scaling has not been adopted here, all values are real.

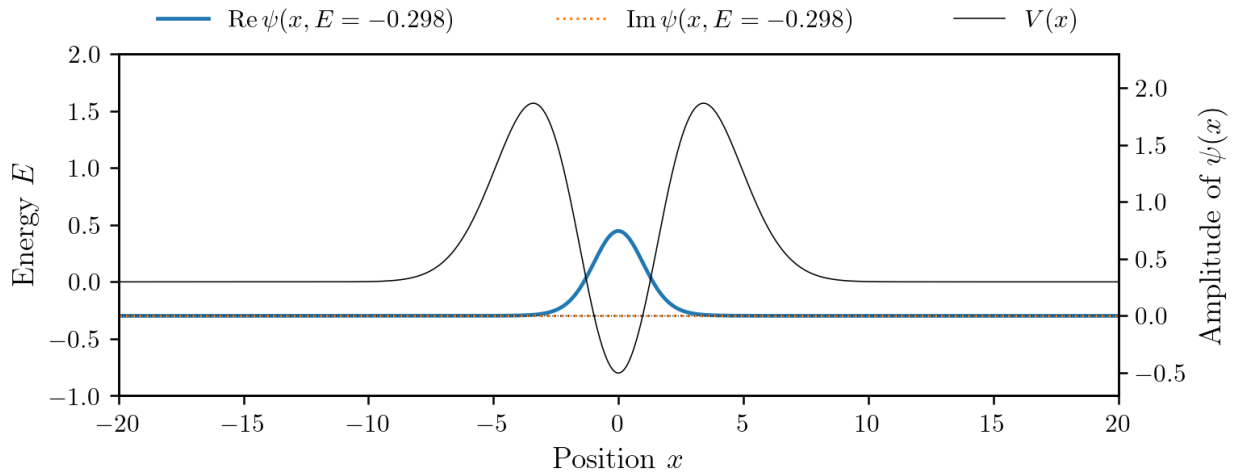


**Figure 38:** Real and imaginary part of the bound state wavefunction obtained by the basis set expansion method using the set of 200 eigenfunctions of the infinite square well potential of size corresponding to the displayed interval of coordinate  $x$ . The graphical representations of the bound state is shifted in the  $y$ -axis direction by the corresponding value of (negative) energy.

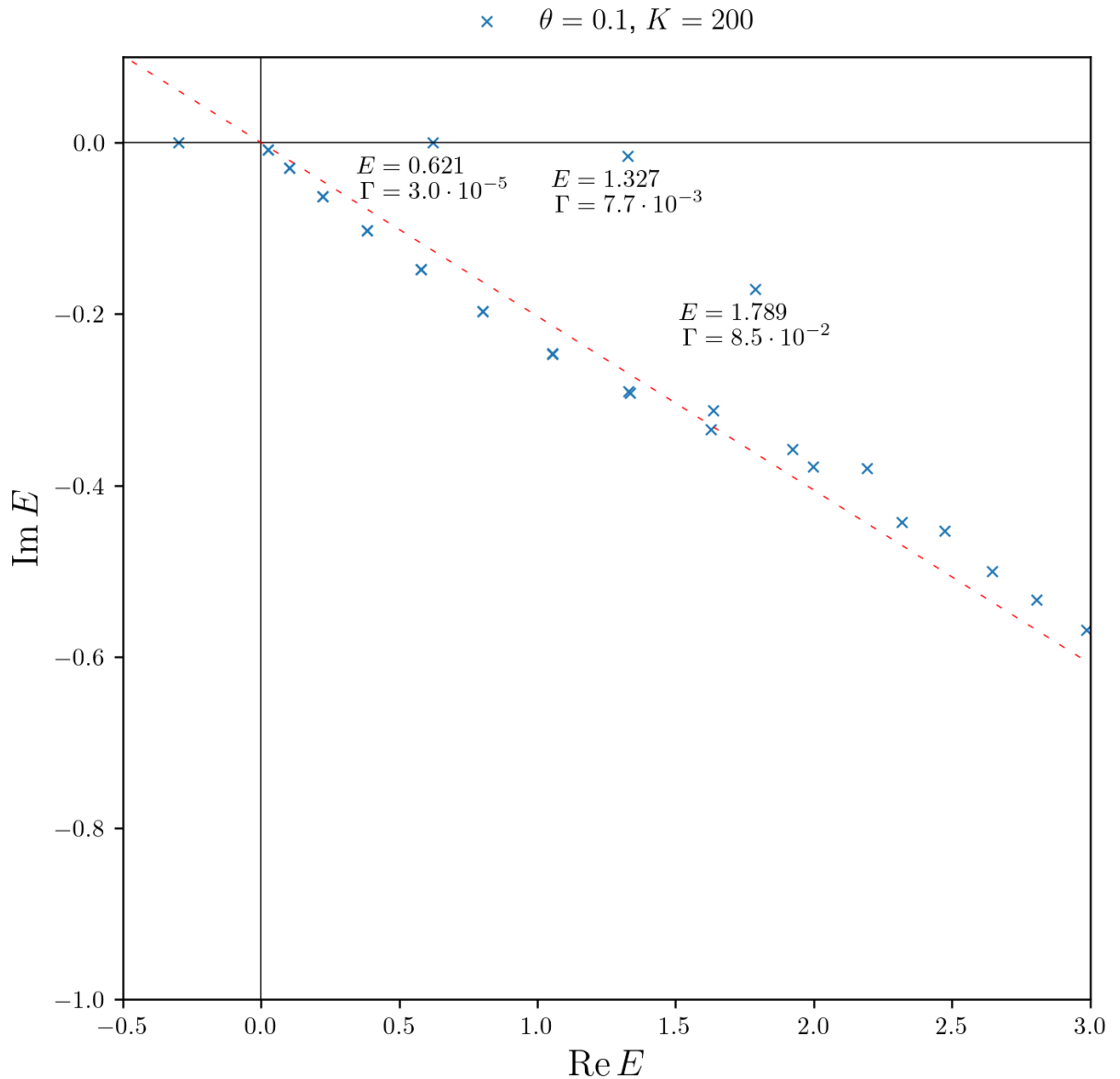


**Figure 39:** Plot of energies calculated by the complex-scaling method combined with basis set expansion. The scaling angle  $\theta$  was set to 0.1, and 200 eigenfunctions ( $K$ ) of the infinite square well were used as the basis set. The straight red line corresponds to the rotation by  $2\theta$ . All recognizable resonances are labeled with their corresponding (real) energy and decay rate constant  $\Gamma$ .

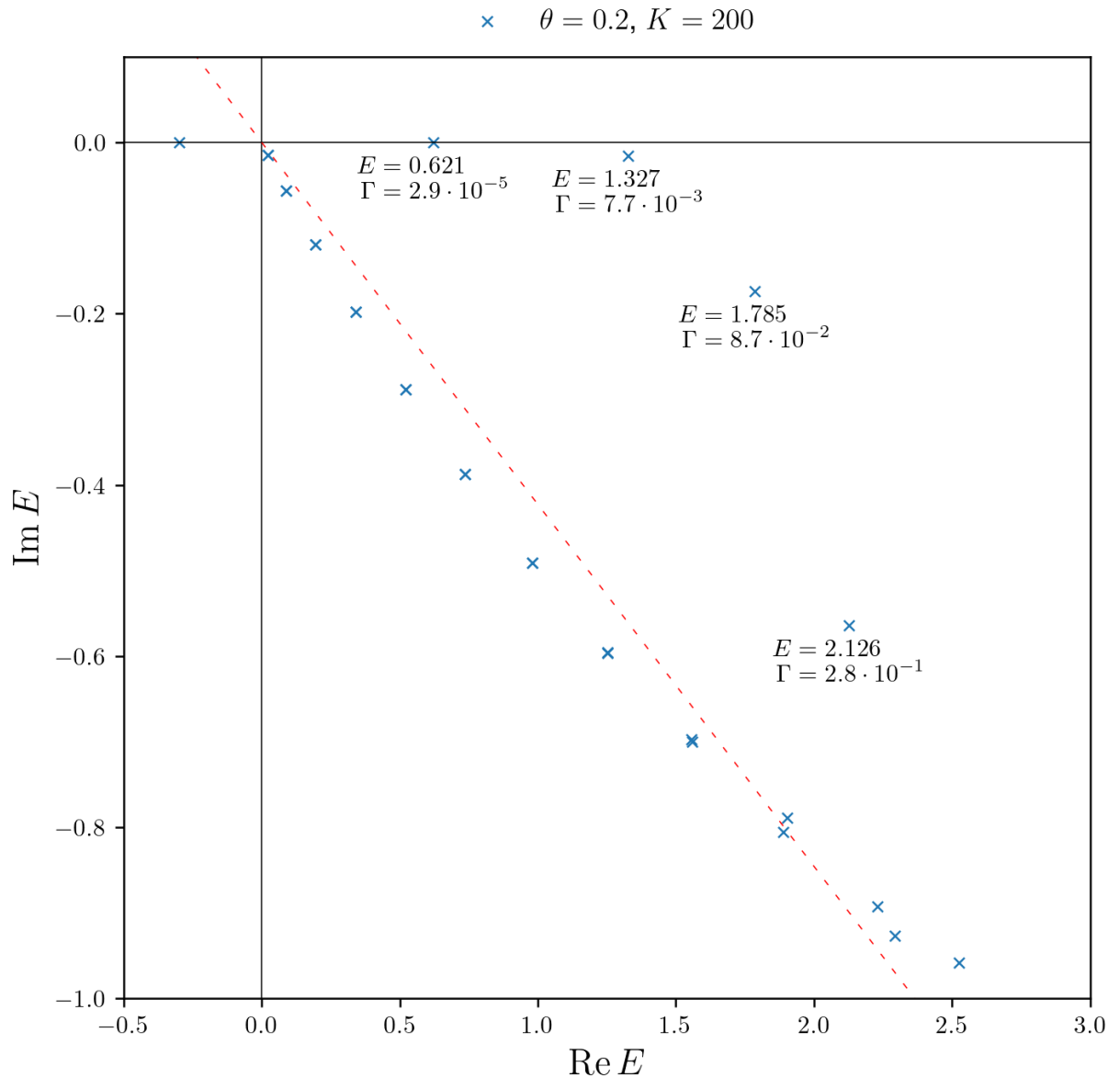


**Figure 40:** Plot of energies calculated by the complex-scaling method combined with basis set expansion. The scaling angle  $\theta$  was set to 0.2, and 200 eigenfunctions ( $K$ ) of the infinite square well were used as the basis set. The straight red line corresponds to the rotation by  $2\theta$ . All recognizable resonances are labeled with their corresponding (real) energy and decay rate constant  $\Gamma$ .

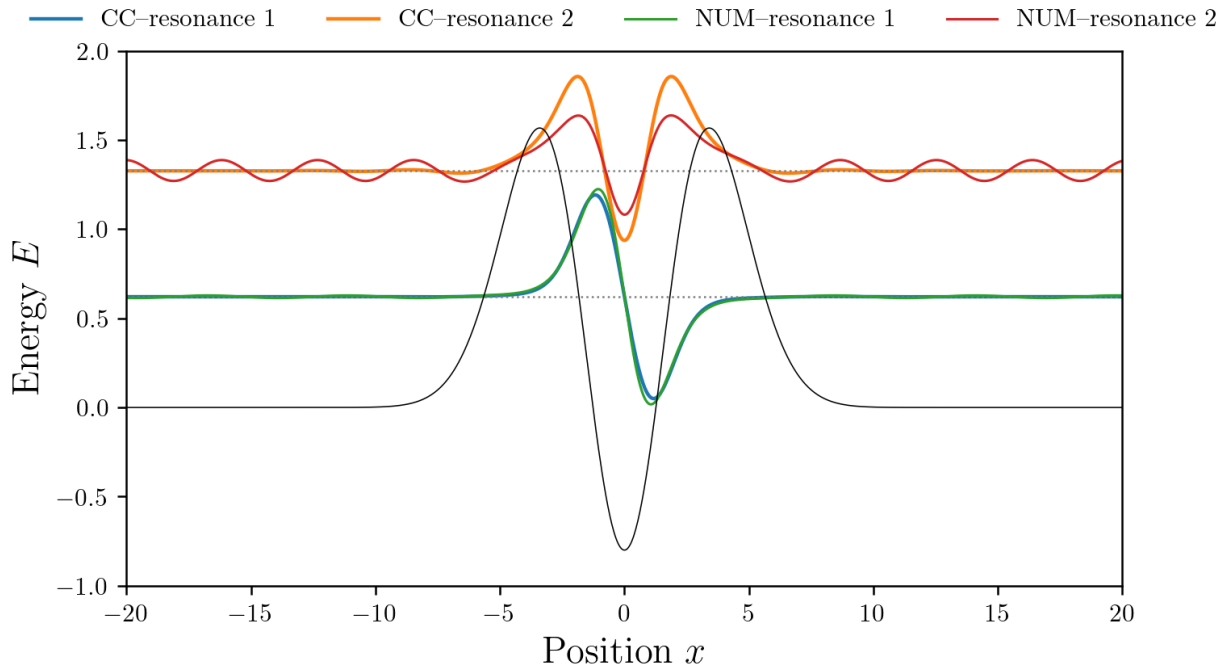


**Figure 41:** Comparison of the wavefunctions obtained by either the numerical approach (NUM, i.e. by propagation on a grid), or by the complex scaling method (CC). The discrepancy might be caused by an error in normalization somewhere in my implementation, or it is the effect of basis set size.

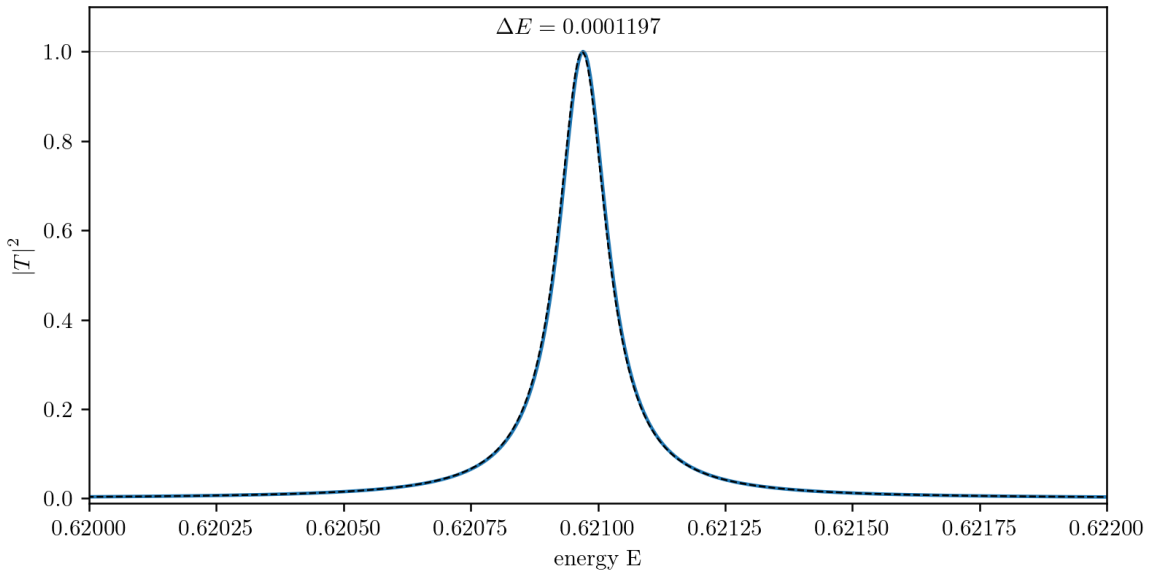


**Figure 42:** Comparison of the first resonance wavefunctions obtained by either numerical propagation on a grid (blue solid line), or by the complex-scaling approach along with the formula for the expected Breit-Wigner lineshape (black dotted line). The offset of both peaks  $\Delta E$  is denoted at the top of quite well-overlaying peaks.

## 5.2 Light Induced Resonances

### 5.2.1 Standard Floquet Theory

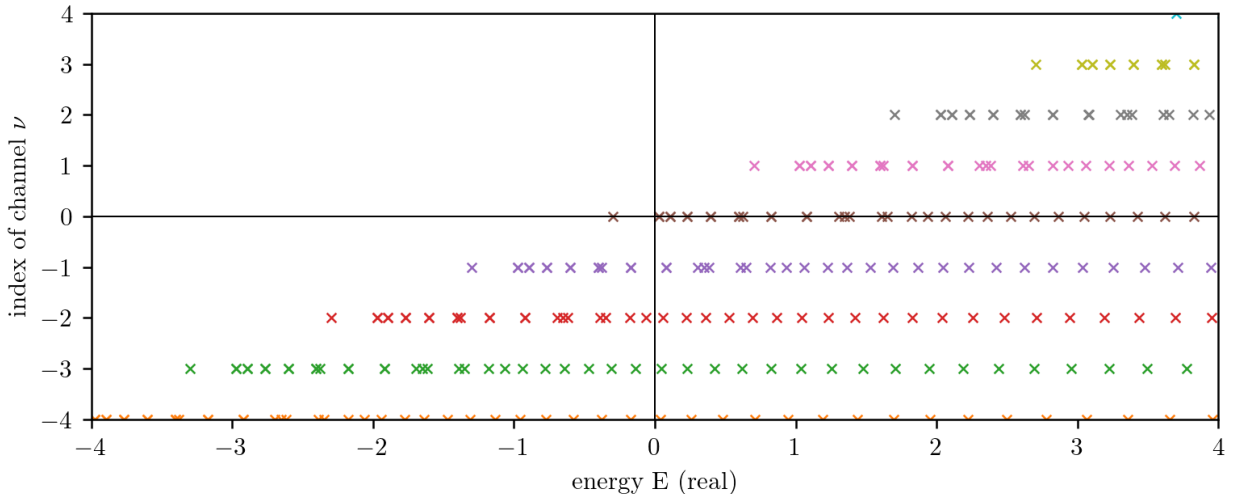


**Figure 43:** Plot of energies calculated by the standard Floquet theory.

### 5.2.2 Non-Hermitian Floquet Theory

#### Significance of Parameters $\alpha_0$ and $\omega$

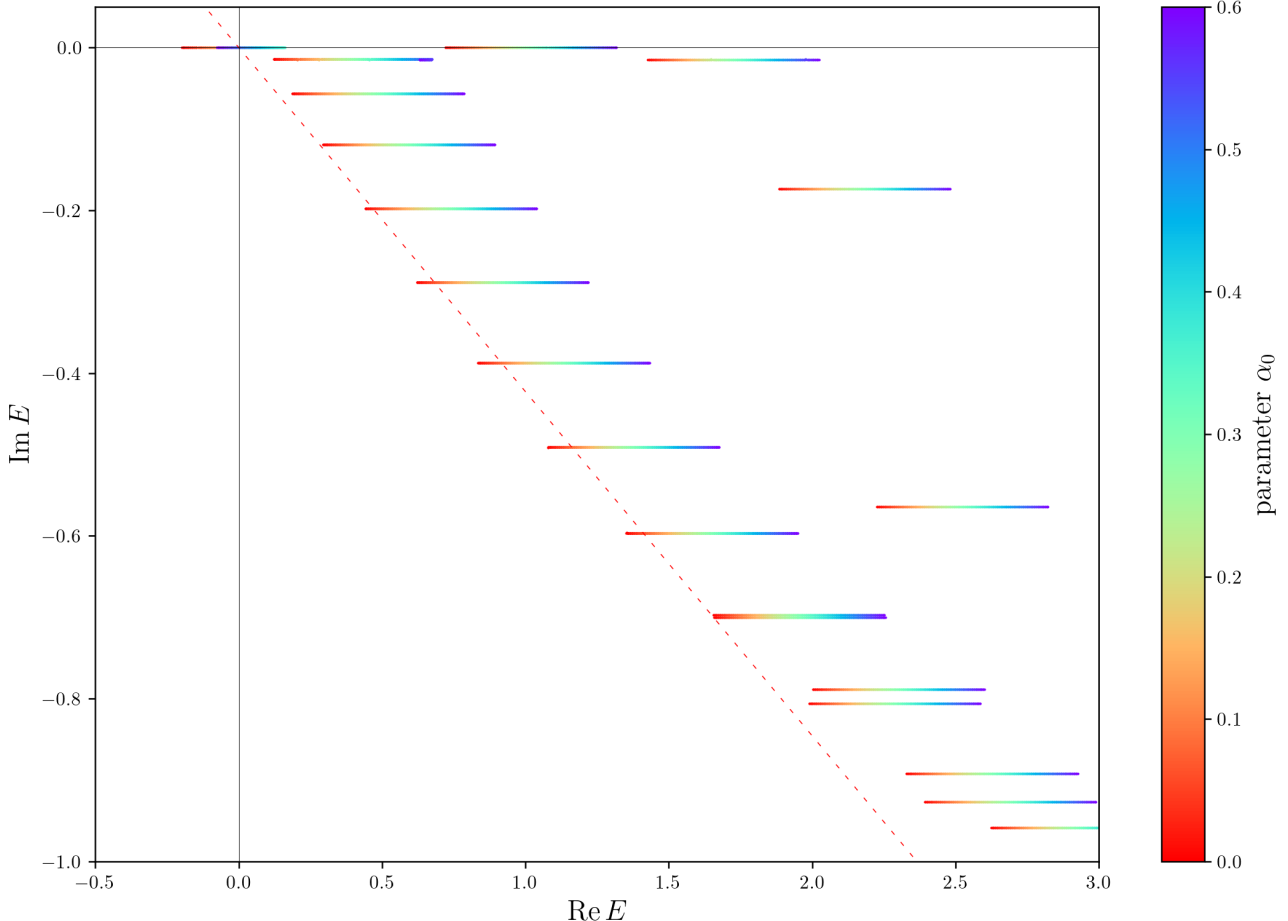


**Figure 44:** Plot of eigenenergy values for a fixed parameter  $\alpha_0 = 0$  and varying parameter  $\omega$  (the colorbar is mislabel, there should be  $\omega$  instead of  $\alpha_0$ ). The values were calculated by the complex-scaling method combined with the Floquet theory and basis set expansion (200 eigenstates of the infinite square well potential were used).

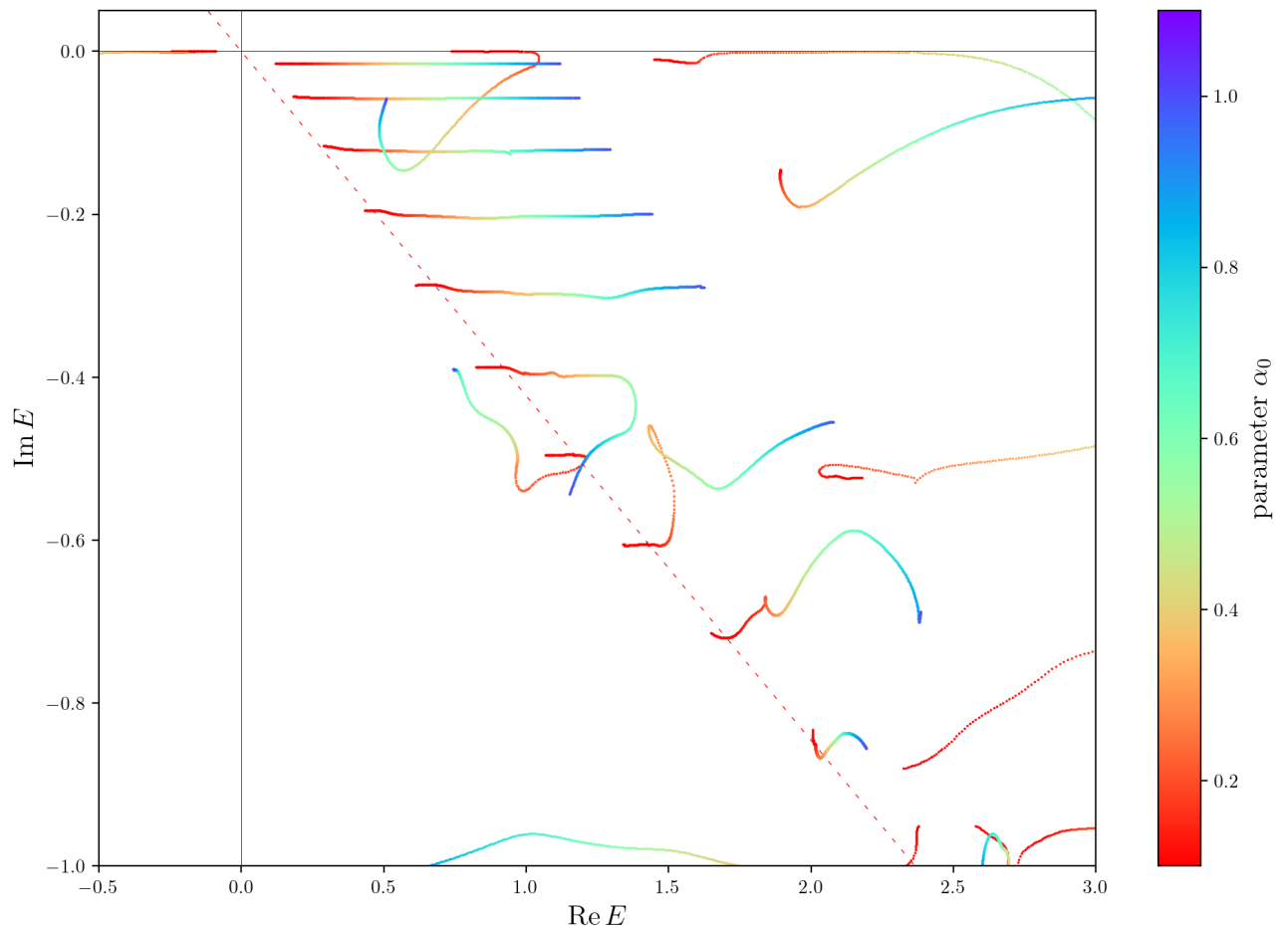


**Figure 45:** Plot of eigenenergy values for a fixed parameter  $\alpha_0 = 1$  and varying parameter  $\omega$  (the colorbar is mislabel, there should be  $\omega$  instead of  $\alpha_0$ ). The values were calculated by the complex-scaling method combined with the Floquet theory and basis set expansion (200 eigenstates of the infinite square well potential were used).

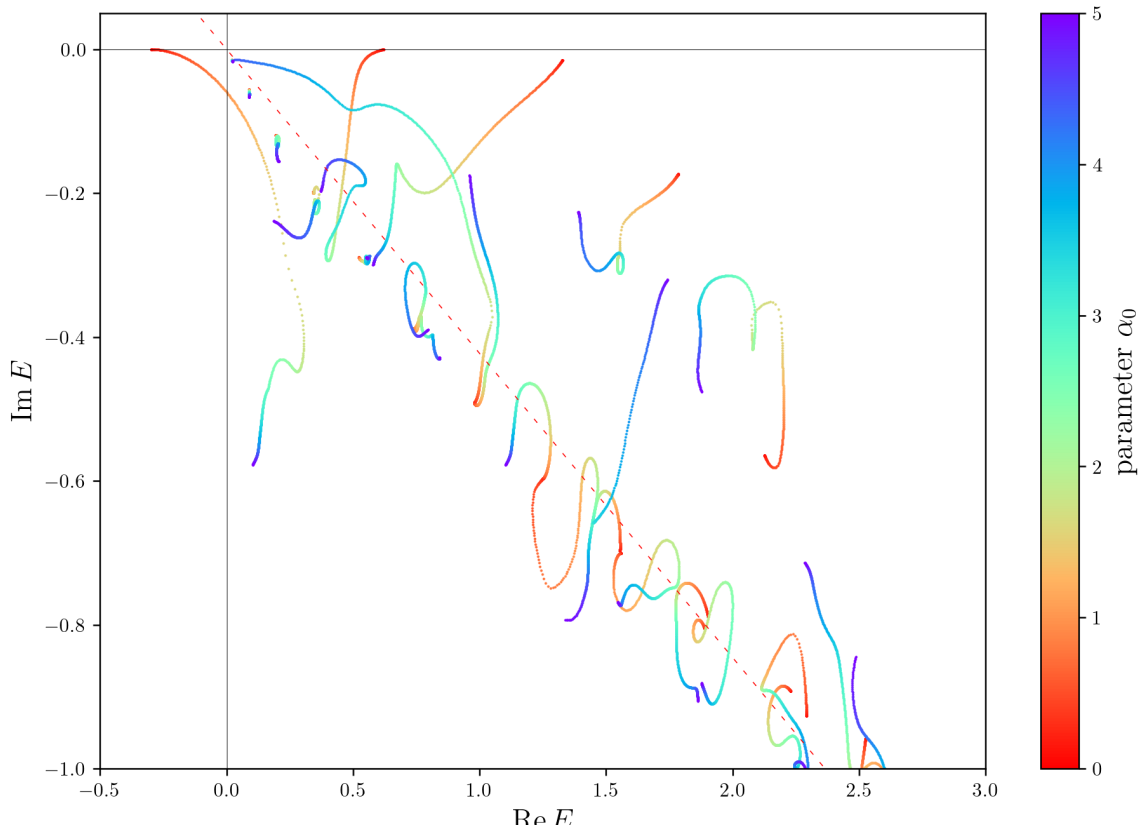
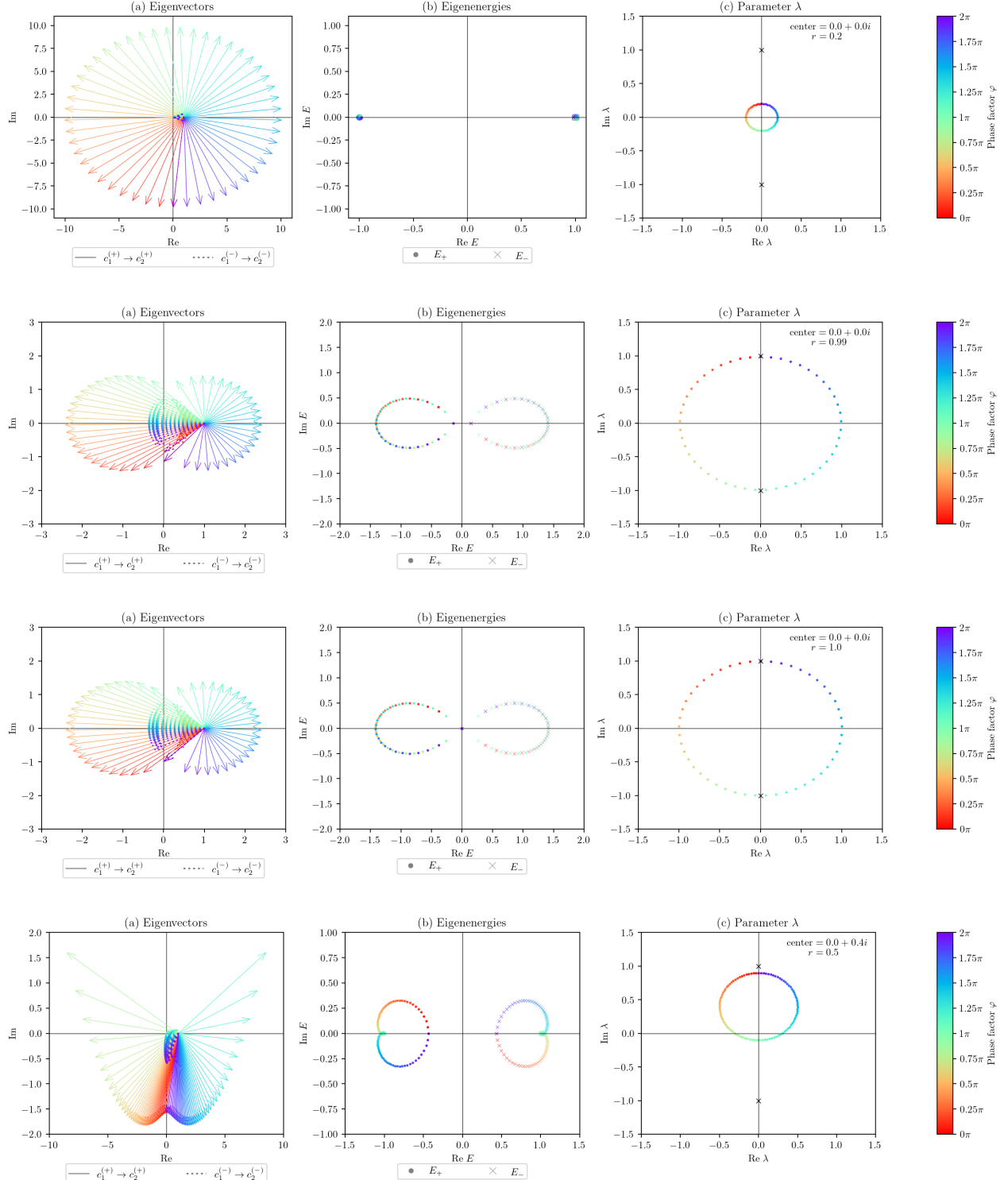


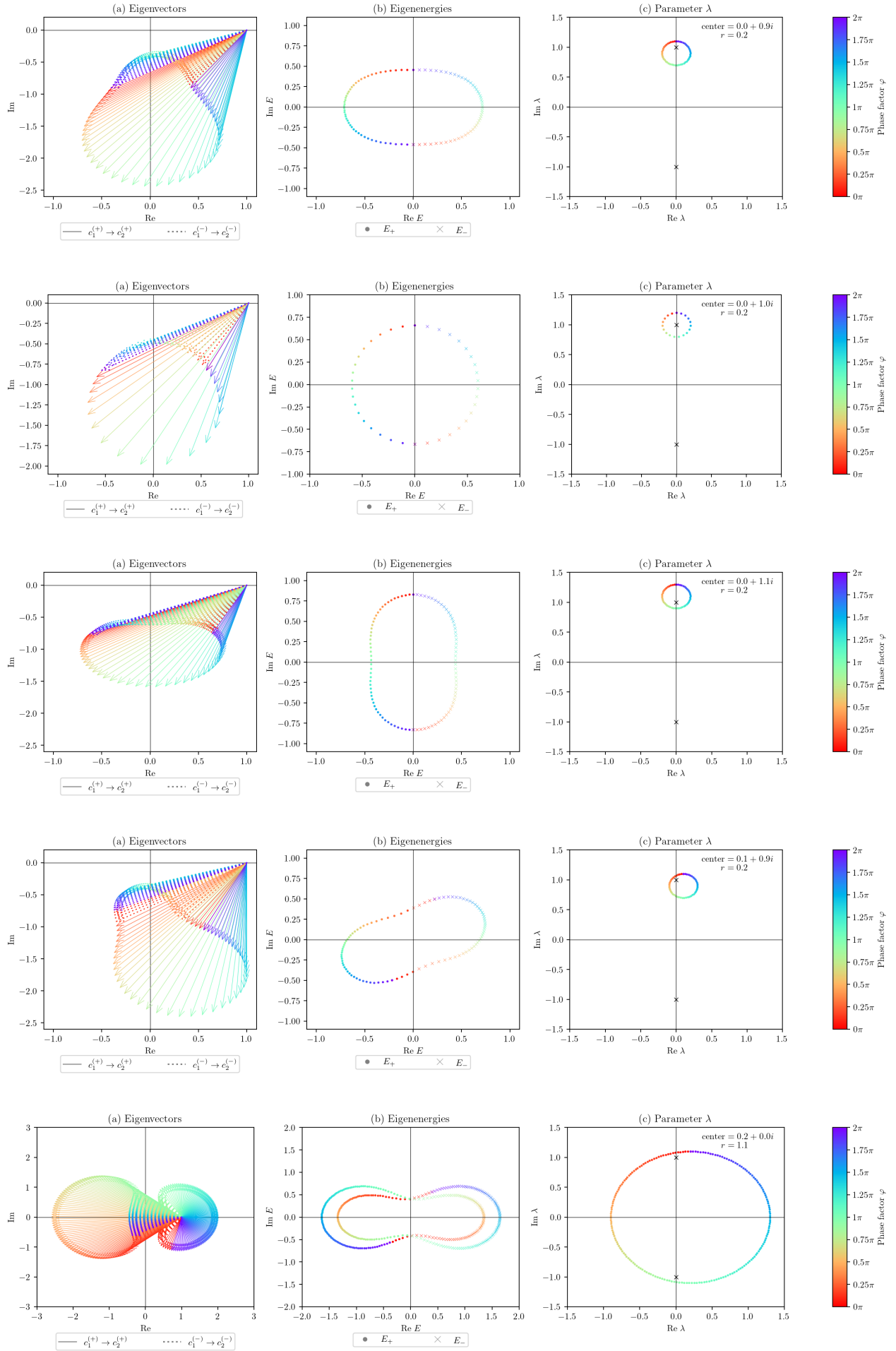
**Figure 46:** Plot of eigenenergy values for a fixed parameter  $\omega = 1$  and varying parameter  $\alpha_0$ . The values were calculated by the complex-scaling method combined with the Floquet theory and basis set expansion (200 eigenstates of the infinite square well potential were used).

### 5.2.3 Exceptional Point

#### Encircling of Exceptional Points

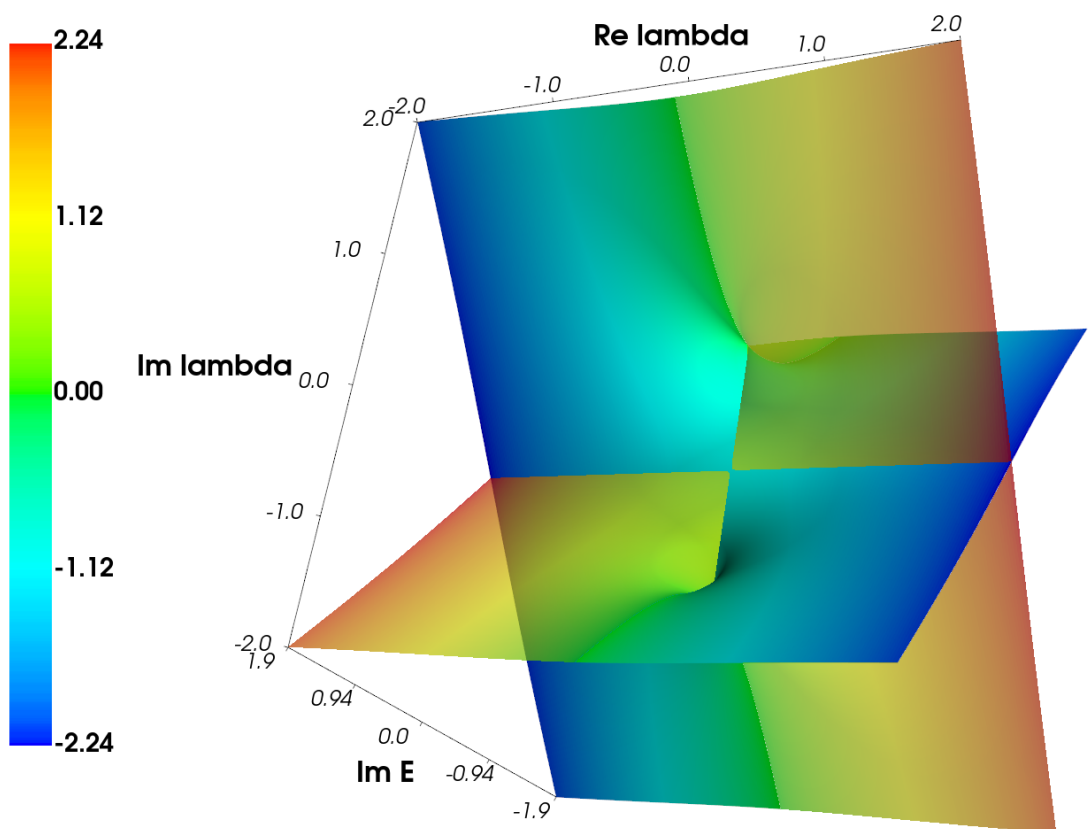
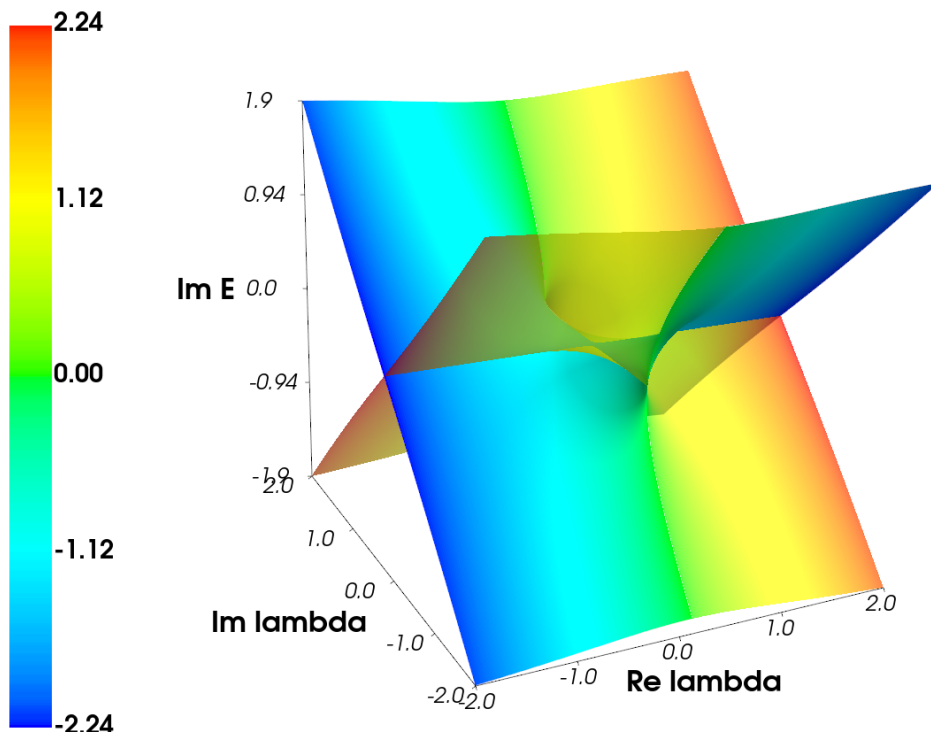
The following plots display the effect of various paths of encircling the exceptional points (plots on the right labeled by  $c$ ). The effect on values of eigenenergies is displayed in the middle (plots labeled by  $b$ ). And finally, an attempt to visualize the eigenvectors was made in the right plots labeled by letter  $a$ .

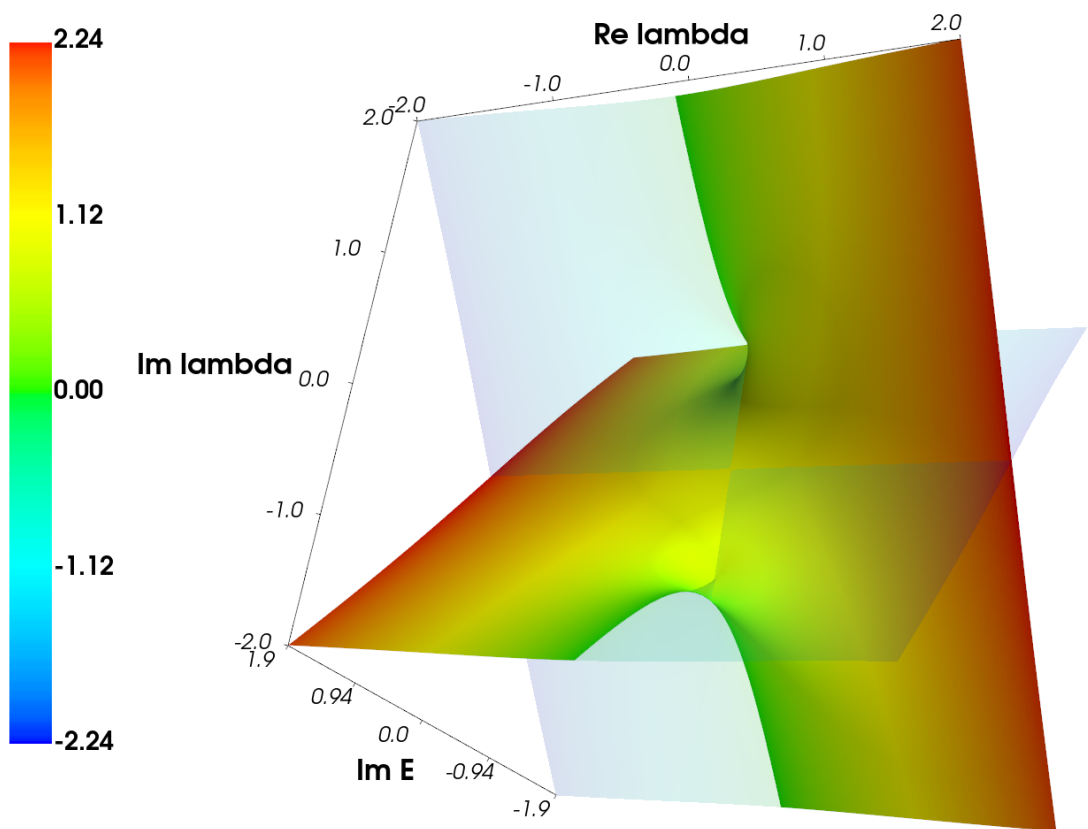
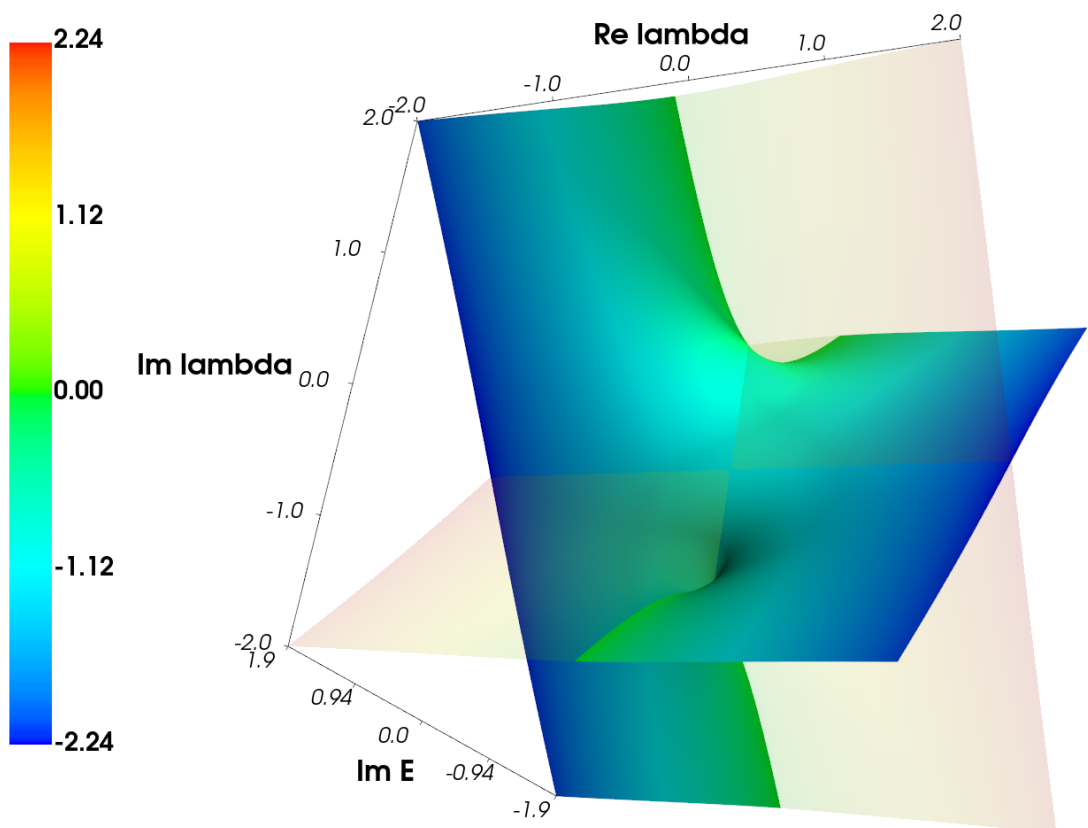


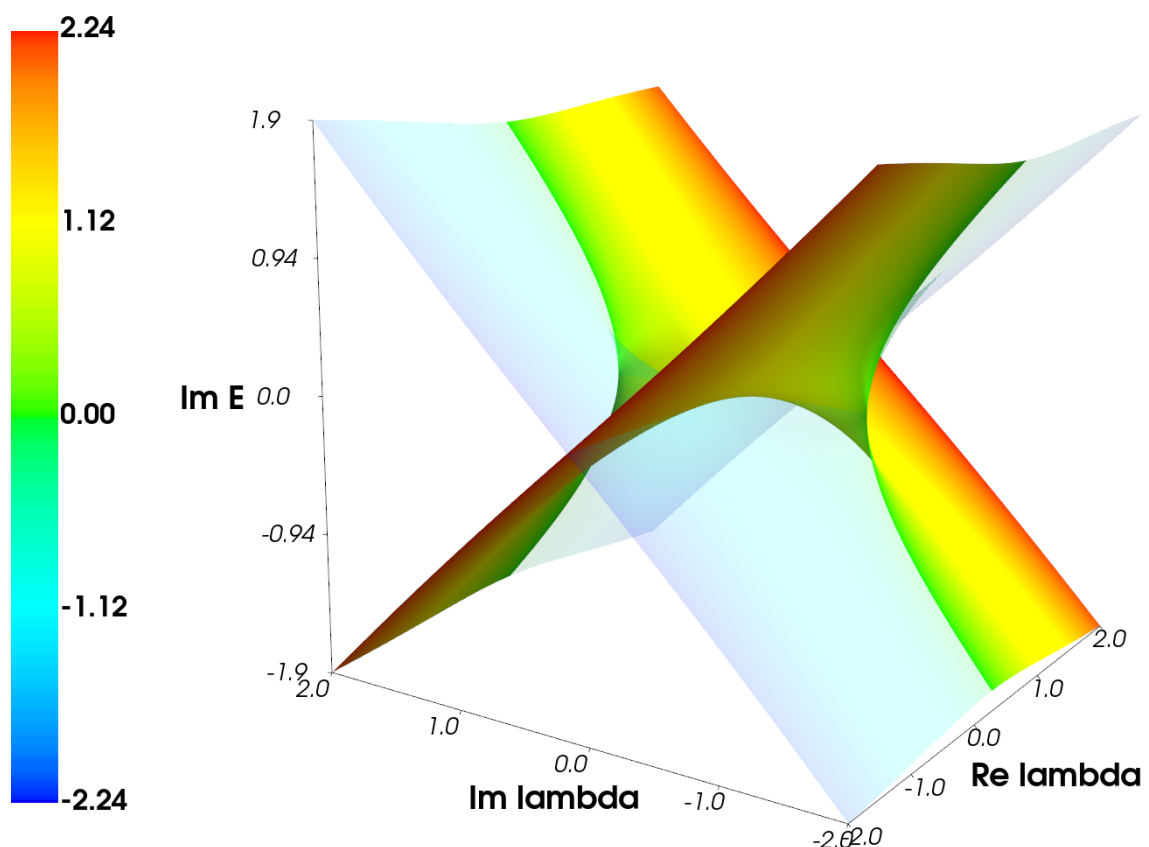
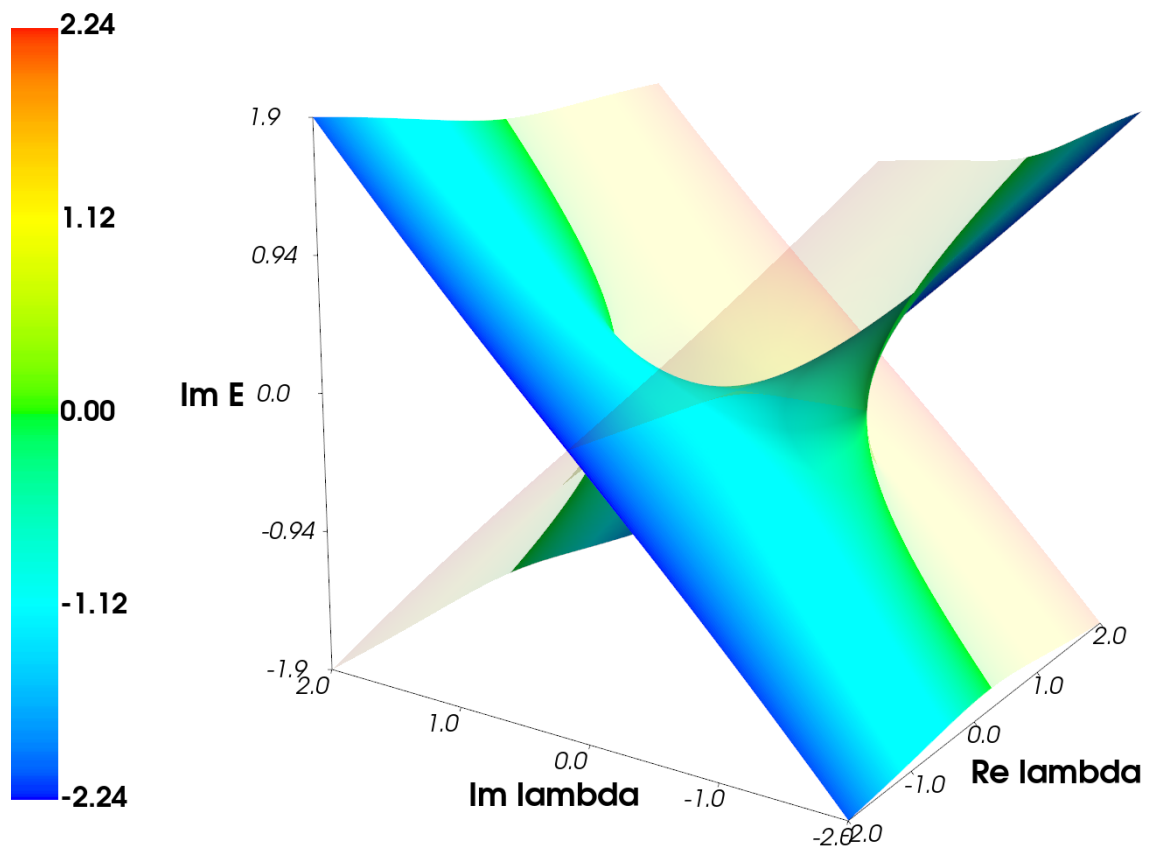


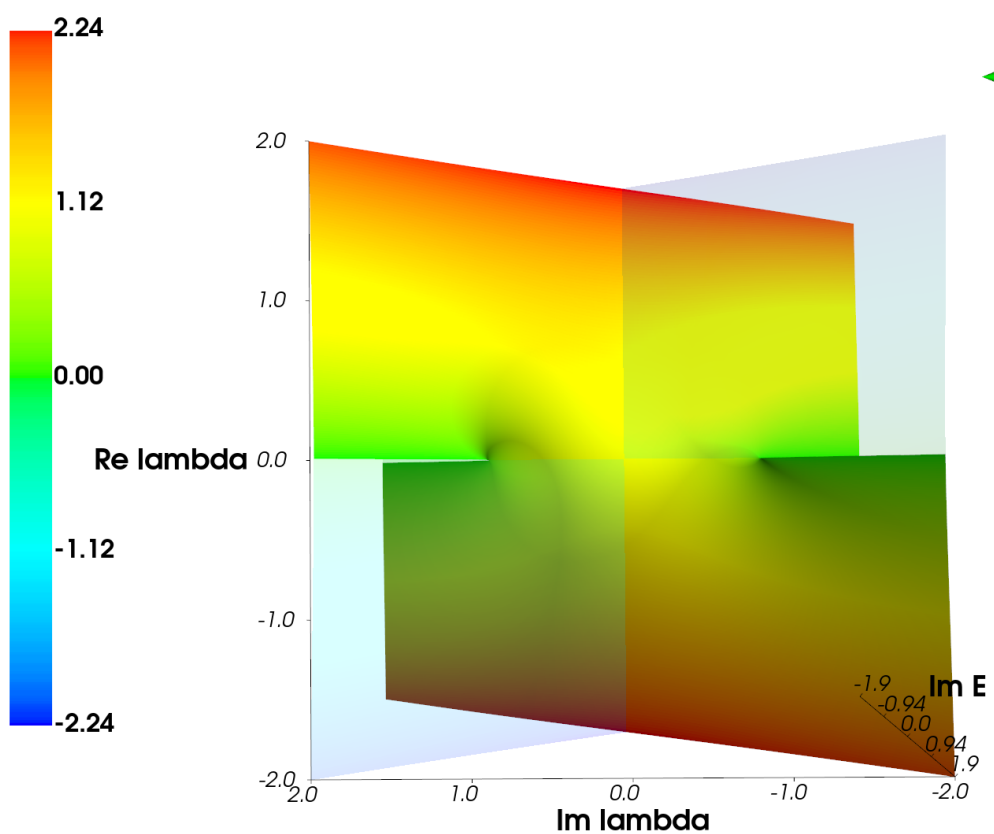
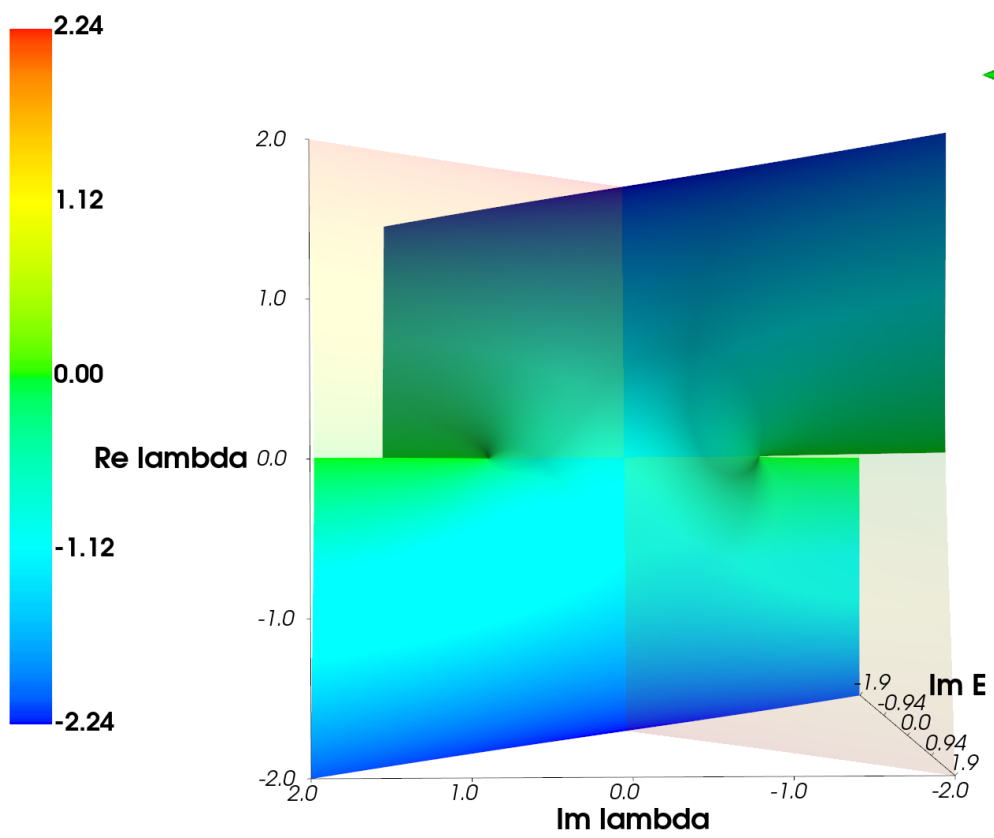
### 3D Depiction of Eigenenergies

The literally complex nature of the dependence of eigenenergies  $E$  on parameter  $\lambda$  was rendered in terms of Riemann-like surface in 3D. The following images shows the rendered model from various sides.  $x$  and  $y$  axis corresponds to the real and imaginary parts of parameter  $\lambda$  respectively. The  $z$  axis represents the imaginary part of eigenenergies  $E$ . The values of eigenenergy real parts are encoded into the rainbow colormap; scale is always displayed by the left size of the images.









## 6 Discussion and Summary

### 6.1 Numerical Approach

Adopting the propagation-on-the-grid algorithm we were able to directly find the numerical values of transmission coefficient  $T$  (see Figure 7), and indirectly the reflective coefficient  $R$  too. Several resonance peaks were observed. The first resonance peak corresponds to the value of energy  $E \approx 0.62109$  and it has thin Lorentzian profile with FWHM  $\approx 1.2 \cdot 10^{-4}$ , see Figure 8. However, the other, higher-in-energy located peaks have much wider profiles since these peaks overlay each other and other effects stemming from their mutual interactions begin to manifest.

The corresponding wave-functions were determined as well, see Figure 11. Both their real and imaginary parts were plotted against the energy and position in a form of 2D and 3D plots as can be seen on many figures in the section of results, subsubsection 5.1.1.

The transmission coefficient phase plot Figure 10 shows that the phase of tends to rise in the areas of resonance peaks and tends to fall elsewhere.

### 6.2 Basis Set Expansion and Complex Scaling

In order to find the energy and the wave-function of the bound state, the basis set expansion method (see brief theoretical description in section 3) was adopted. Two kinds of states are obtained—a single bound-state, and a set of states identified as a quasi-continuum. That is, as the size of the used basis set would rise, the energies would asymptotically form a continuum of states. However, since the basis set size is finite, the continuum is discretized into the so-called quasi-continuum states, see Figure 4.

To get direct access to the resonances, the complex-scaling method was used (see theoretical description in subsection 2.3 for more information). The number of unraveled resonances depends on the scaling parameter (angle)  $\theta$  as can be seen on Figure 39 and Figure 40. The wave-functions of the first two resonances were also plotted and compared with the numerically obtained results (Figure 41). The discrepancy in the wave-function of the second resonance peak might be the result of insufficient basis set size, or some mistake in the algorithm implementation, which I wasn't able to localise and correct. Similarly, the two approaches were compared in terms of the lineshape of the first resonance peak in the transmission coefficient square spectra (Figure 42). The overlap of transmission resonance peak is quite perfect between those two approaches though.

### 6.3 Floquet Theory and Complex Scaling

The next section studied the influence of light interaction on the resonances. To be able to describe the interaction analytically, the Floquet theory was used (see Figure 43). Consequently, it was combined with the complex scaling method again. Two main parameters describing the strength of the light-matter interaction arose—amplitude of light  $\alpha_0$ , and the frequency of light  $\omega$ . In general, the interaction with light renders the original bound state into a new type of resonance state—the so-called Feshbach resonance, in contrast to the so-called shape resonance studied before. The Feshbach resonance are a direct consequence of interaction with light. The influence of both free (experimental) parameters were studied in Figure 44–46.

Since the eigenenergies can travel all around within the complex plane by varying the two free parameters, in theory, two such eigenenergies can become degenerate and give origin to the so-called exception points (see the theory section for more information). The figures in subsubsection 5.2.3 again shows the manifestation of various combinations of parameters on a reduced model (a limit case of weak monochromatic laser). The intriguing properties of exceptional points were again described thoroughly in the theoretical introduction in subsubsection 2.4.4.

## References

Santoro, G. E. (2019). Introduction to Floquet. [https://www.ggi.infn.it/sft/SFT\\_2019/LectureNotes/Santoro.pdf](https://www.ggi.infn.it/sft/SFT_2019/LectureNotes/Santoro.pdf).